Universität Bremen*

*EXZELLENT.

Syntheses, structures and characterizations of novel arsenotungstates

-NLO, conductivity, band-gap and thermal expansion properties-

Dissertation
zur Erlangung des Doktorgrades der Naturwissenschaften
-Dr. rer. nat.-

Vorgelegt dem Promotionsausschuss
des Fachbereichs 02 (Biologie/Chemie)
der Universität Bremen

von
Pei Zhao
Chemische Kristallographie fester Stoffe
Bremen, im Juli 2015

Erstgutachter: Prof. Dr. Thorsten M. Gesing, Universität Bremen

Zweitgutachter: Prof. Evgeny V. Alekseev, RWTH Aachen University

Tag des Kolloquiums

Declaration

I hereby declare that this submission is my own work and that, to the best of my knowledge and belief, it contains no material previously published or written by another person nor material which to a substantial extent has been accepted for the award of any other degree or diploma of the university or other institute of higher learning, except where due acknowledgment has been made in the text.

Signature:____________________________ Date:______________________________

Abstract

The relationship between structures and properties of inorganic compounds is one of the most interesting topics the chemists, the material scientists and relevant communities focus on. Although real materials are much more complex than the monatomic or diatomic systems used for test in theory analysis, people still attempt to get as much information as possible and try to understand the behavior of materials. One of the most investigated families is the metal-tungsten-oxygen system. Tungsten atoms possess flexible coordination geometries which can coordinate with 4, 5 or 6 oxygen atoms leading to tetrahedral, trigonal bipyramidal or octahedral geometry, respectively. Moreover, W^{6+} (d^0 element) is susceptible to second-order Jahn-Teller (SOJT) distortion, leading to spontaneous off-centering distortion of the associated WO_6 octahedra. Off-centering distortion of the polyhedra becomes greater, especially when metal atoms incorporate into the same crystallographic positions in the structure. Associated with their crystal-structures, excellent physical properties were intensively studied and also used widely.

In the chapter 1, three groups of tungsten compounds: tungsten oxides, tungsten bronzes and tungstates (VI) are reviewed mainly including their symmetries, structures and applications. The first and foremost motivation of this study was because of the interesting nonlinear optical property. Chapter 2 is the experimental methods including three parts: synthesis methods of powder and single crystal samples; raw materials with production companies and purities; instruments for a variety of characterization. Based on the first alkali metal arsenotungstate, we synthesized two novel compounds by replacing alkali metals. Of them, the sodium arsenotungstate is isotypic to the potassium compound, but the lithium compound has a completely new framework. The structures will be discussed in detail in the chapter 3 along with diffraction, Raman and infrared spectra, thermal analysis and properties like nonlinear optical. Then in the next chapter, we discussed the temperature-dependent properties of these three products, especially thermal expansion behavior. Combining low-temperature powder neutron and high-temperature powder X-ray diffraction data, the metric parameters can be extracted from the Rietveld refinements and modeled using Grüneisen first-order approximation for the zero-pressure equation of state. The internal energy were calculated by Debye-Einstein-Anharmonicity model. Using Raman spectra data and the autocorrelation method, we can get more information during the temperature changing process. We also measured electrochemical impedance spectroscopy to know conductivity properties. In the following chapter, we get the phase diagram of the system K_2O-As_2O_5-WO_3

by the conventional solid-state reaction. By selecting the special points with different molar ratios of raw materials and analyzing products via powder X-ray diffraction patterns, the most parts of the phase diagram can be drawn. The final chapter is the overall summary and outlook of this thesis.

Key words: alkali metal arsenotungstate, temperature-dependent, nonlinear optical, thermal expansion, Debye-Einstein-Anharmonicity model, autocorrelation, density function theory, phase diagram

Chapter 1 General introduction and motivation

1.1. Introduction

Tungsten (W) is a transition metal in the sixth period and group 6 (VI b) of the periodic table with electron configuration of $[Xe]4f^{14}5d^{4}6s^{2}$. Due to its near half-filled $5d$ shell, the high bonding energy leads to some interesting physical properties [1]. It has the lowest vapor pressure of all metals, the lowest compressibility, an extremely high density, a high modulus of elasticity, low thermal expansion and high thermal conductivity. Particularly, it has the highest melting point of all metallic elements. The structural aspect is interesting as well. Of several oxidation states, the most common formal oxidation state of tungsten is +6. In compounds, its coordination number usually varies from 4 to 6. Greater degree of distortion in the W-centered polyhedra, especially when heteroatoms incorporate into the same crystallographic positions in the structure, gives more possibilites of new properties. Within the scope of this chapter, several types of tungsten compounds: tungsten oxides, tungsten bronzes, and tungstates (VI) are reviwed, leading to motivation of this research work.

1.2. Tungsten oxides

The idealized structure of WO_3 is of ReO_3-type with a three-dimensional network of corner-sharing WO_6 octahedra. However, in reality, the cubic WO_3 modification is only observed in thin condensed films [2]. WO_3 has a very complicated structural distortion and undergoes several transitions upon heating. All of the polymorphs conserve lower symmetry owing to the distortions of the WO_6 octahedra. The detailed determination of phase-transitions was well reviewed and studied from room-temperature to 1273 K by means of high-resolution neutron powder diffraction by Howard et al. [3]. The structure of WO_3 changes with increasing temperature from monoclinic Pc (below ~ 230 K) [4], via triclinic $P\text{-}1$ (~ 230 K – 290 K) [4], monoclinic $P2_1/n$ (~ 290 K – 623 K), orthorhombic $Pbcn$ (~ 623 K – 993 K), monoclinic $P2_1/c$ (~ 993 K – 1073 K), tetragonal $P4/ncc$ (~ 1073 K – 1173 K) to $P4/nmm$ (above ~ 1173 K); the metric parameters of some of them are given in **Table 1.1**.

The motivation for such detailed study of crystallorgraphy is of wide applications [5]. Besides it is an important raw material for producing other tungsten compounds [6-7], the semicondutor WO_3 is well-known for its use in electrochromic [8], photocatalysis [9], gas sensors [10], advanced energy system [11], solar enery conversion and water splittings [12] etc.

Table 1.1: The metric parameters (in units of pm and °) of WO_3 at different temperature with standard deviation of 1 pm and 0.1°, respectively.

Temperature range	Space group	*a*	*b*	*c*	*α*	*β*	*γ*
below ~ 230 K	*Pc*	527	516	767	90	91.92	90
~ 230 K – 290 K	*P*-1	730	752	769	88.83	90.92	90.93
~ 290 K – 623 K	$P2_1/n$	730	754	769	90	90.86	90
~ 623 K – 993 K	*Pbcn*	736	757	776	90	90	90
~ 993 K – 1073 K	$P2_1/c$	528	526	783	90	90.48	90
~ 1073 K – 1173 K	*P*4/*ncc*	528		785	90	90	90
above ~ 1173 K	*P*4/*nmm*	530		393	90	90	90

WO_3 can be reduced by tungsten to intermediates between WO_3 and WO_2. With the decreasing ratio of oxygen to tungsten, the common corner-sharing oxygen atoms progressively changed to edge and face-sharing. Even some new structural features formed like WO_7 pentagonal bipyramids surrounded by five edge-sharing WO_6 octahedra. Several structures of WO_x (x = 2.625 – 2.92) such as $W_{32}O_{84}$ [13], W_3O_8 [14], $W_{18}O_{49}$ [15], $W_{17}O_{47}$ [16], W_5O_{14} [17], $W_{20}O_{58}$ [18], $W_{25}O_{73}$ [19] have been obtained experimentally; their crystal structures are shown in **Figure 1.1**. Due to high degree of disordering, the high-resolution electron microscopy (HREM) lattice imaging became quite popular and useful in studying these structures along with complemenatry X-ray and neutron diffraction techniques. These intermediates WO_x are known as Magnéli phase and display metal-like properties [20]. One of the important oxides WO_2 crystallizes in $P2_1/c$ with lattice parameters a = 557.69(2) pm, b = 489.86(1) pm, c = 566.44(2) pm and β = 120.678(1)° obtained by neutron powder diffraction data [21].

1.3. Tungsten bronzes

Tungsten bronzes [22] are a group of nonstoichiometric compounds with the general formula of M_xWO_3, where x is in the range of $0 < x < 1$ and M represents a metal with a large variety of species. They are intensely colored denpending on the value of x and exibit metallic lustre where the name come from.

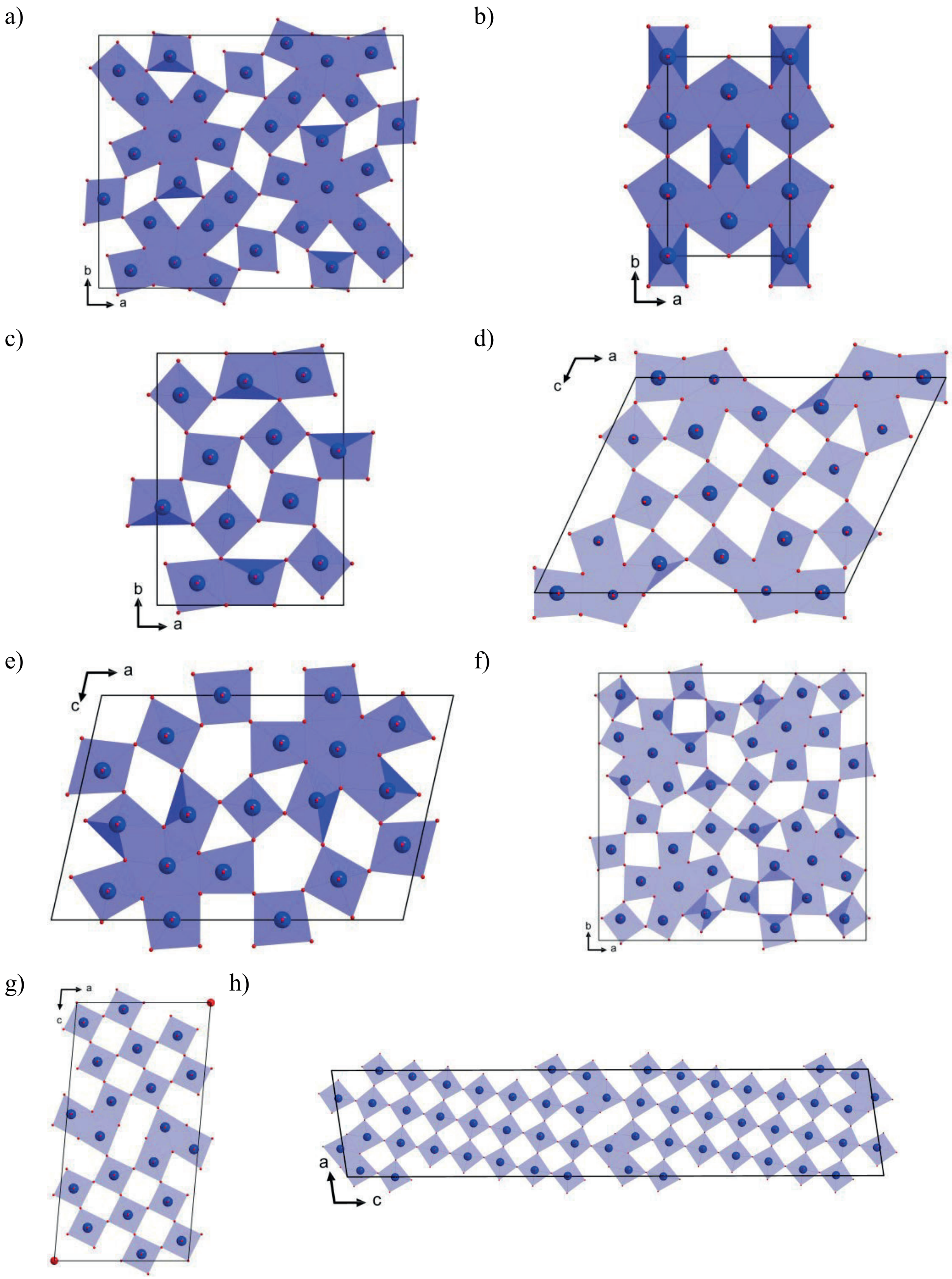

Figure 1.1: The crystal structures of a) $W_{32}O_{84}$, b) W_3O_8 (*C*222), c) W_3O_8 (*Pbam*), d) $W_{18}O_{49}$, e) $W_{17}O_{47}$, f) W_5O_{14}, g) $W_{20}O_{58}$ and h) $W_{25}O_{73}$. The tungsten and oxygen atoms are displayed in blue and red color respectively.

The mobility of cations in WO_3 framework can modify the electronic properties of materials. Especially, the superconductivity property is intensively investigated [23]. Most commenly, M is an alkali metal cation, and the formula can be written as $A_xW^{5+}{}_xW^{6+}{}_{1-x}O_3$. As the value of x decreases, so does the structure symmetry. The most universal preparation method is the solid-state reaction [24]. The alkali metal compounds are finely grounded with WO_3 and WO_2 or W and heated up to a certain temperature. There are also other ways like the vapour-phase reaction [25] and the electrolytic reaction [26].

The crystal structures are based on the corner-sharing linkage of WO_6 octahedra with the metal cations located in the formed channels. The particular adopted structure depends on x value and the ionic radius of M. Further more, changing synthesis methods could also effect the construction of the framework and cause the shift of x value ranges for the same structure type [24,26]. In the **Table 1.2** shown below, all the data at room-temperature condition are collected based on the solid-state reaction method. The structures can be classified into four types which are perovskite tungsten bronzes (PTB), tetragonal tungsten bronzes (TTB), hexagonal tungsten bronzes (HTB) and intergrowth tungsten bronzes (ITB). PTB can be further divided into four crystal systems: monoclinic (PTB_m), orthorhombic (PTB_o), tetragonal (PTB_t), cubic (PTB_c).

Table 1.2. Collected x value ranges for variable structure types in tungsten bronzes.

$A_xW^{5+}{}_xW^{6+}{}_{1-x}O_3$	M = Li	M = Na	M = K	M = Rb	M = Cs
Ref.	[24]	[24]	[24,27-30]		
PTB_m	0 – 0.008	0 – 0.01	–	–	–
PTB_o	0.028 – 0.032	0.01 – 0.045	–	–	–
PTB_t	0.095 – 0.11	0.045 – 0.085	–	–	–
PTB_c	0.26 – 0.5	0.37 – 0.95	–	–	–
TTB	–	0.26 – 0.35	0.4 – 0.59	–	–
HTB	–	–	0.22 – 0.31	0.16 – 0.33	0.16 – 0.33
ITB	–	–	0.06 – 0.1	0.06 – 0.1	0.06 – 0.1

The primary building units and connection ways in four types are same. The main differences are the formed channels (**Figure 1.2**). PTB have four-membered ring (4-MR) channels. The further symmetric division due to the tilting of WO_6 octahedral units. TTB have 3-MR, 4-MR and 5-MR channels in the framework. The alkali metal ions are located in the larger 4-MR or 5-MR or both channels. HTB form 3-MR and 6-MR channels and cations prefer to reside in the larger channels. ITB can be described as an ordered intergrowth of

HTB with WO_3 slabs. The widths of these two slabs can vary and the numbers of slabs can be used as the name of the structure. (1, 5) and (1, 6) types are the most frequently observed. However, as low as (1, 4) and as high as (1, 14) have also been observed in the ITB compounds.

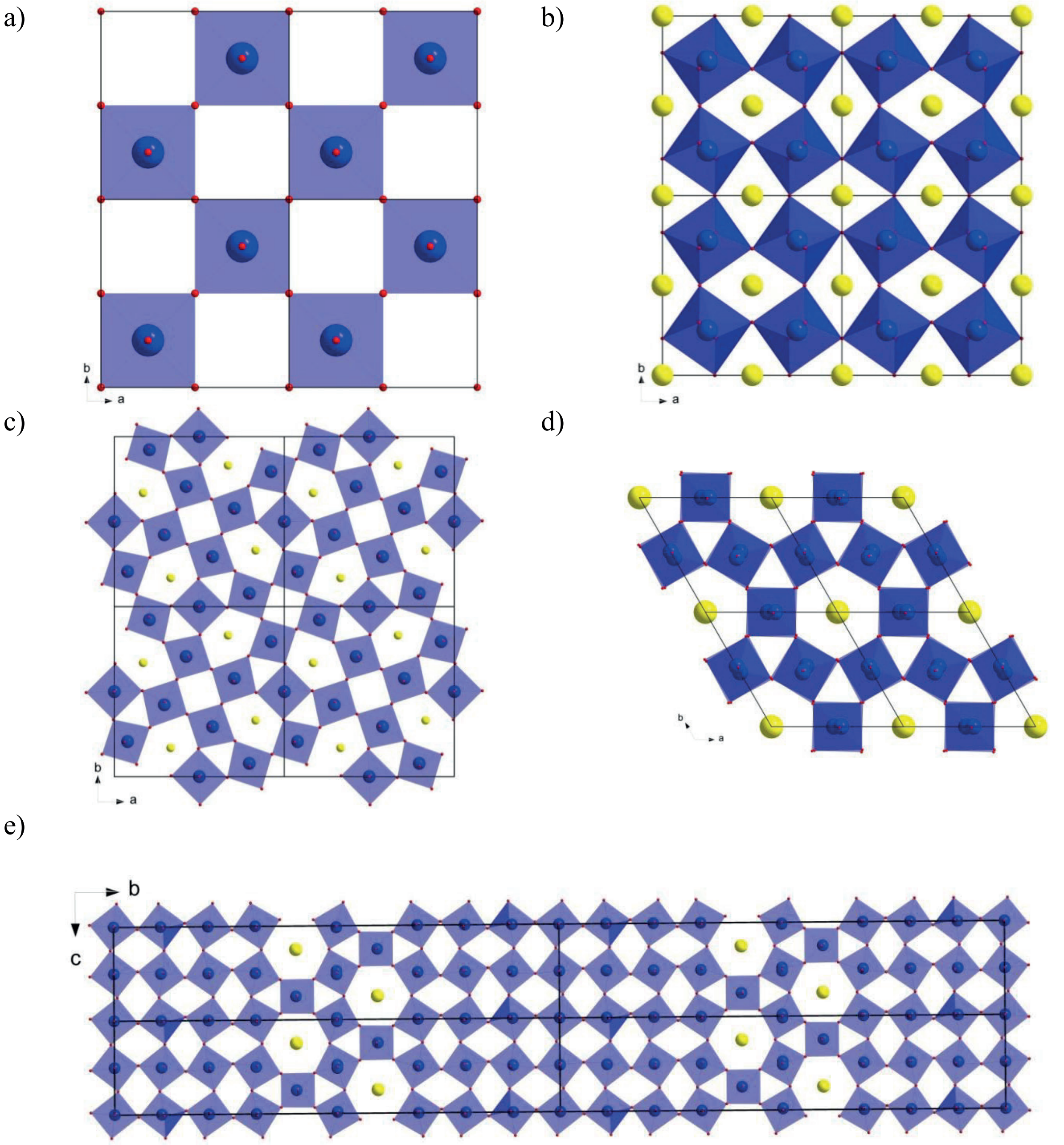

Figure 1.2: The crystal structures of a) perovskite tungsten bronze (PTBt) $Li_{0.095}WO_3$, b) perovskite tungsten bronze (PTBc) $Li_{0.36}WO_3$, c) tetragonal tungsten bronze (TTB) $Na_{0.28}WO_3$, d) hexagonal tungsten bronze (HTB) $K_{0.26}WO_3$ and e) intergrowth tungsten bronze (ITB) $Cs_{0.07}WO_3$. In all above figures, tungsten, oxygen and alkali metal atoms are displayed in blue, red and yellow color respectively.

When vanadium, niobium or tantalum fully substitutes tungsten with the valence of +5, one special bronze-type products are produced and known as bronzoids [31-32], means fully oxidized phases. From the compositional and structural points of view, they are bronze-like, but they are insulating phases contrary to the bronze due to d^0 configuration [33].

1.4. Tungstates (VI)

Tungstates possess various functional properties depending on the structures [34]. According to the metal with different oxidation states, tungstates (VI) can be separated into several groups.

1.4.1. Monometallic tungstates with +1 cations

In the monovalent metal tungstate A_2O-WO_3 system, there are many compounds with different molar ratios. For example, the K_2O-WO_3 system [35-37] have reported compounds K_4WO_5 (2 : 1), K_2WO_4 (1 : 1), $K_2W_2O_7$ (1 : 2), $K_2W_3O_{10}$ (1 : 3), $K_2W_4O_{13}$ (1 : 4) and $K_2W_6O_{19}$ (1 : 6). Of these, the sample with molar ratio of 1 : 1 which is A_2WO_4 has been studied the most.

Lithium tungstate Li_2WO_4 [38] has the phenacite-structure type with space group $R\overline{3}$. Sodium tungstate Na_2WO_4 [39] has three different solid phases at atmospheric pressure. Among them, the room-temperature phase cystallizes in the cubic spinel-type space group $Fd\overline{3}m$ and is stable till 860 K. K_2WO_4 and Rb_2WO_4 [40] are isomorphous and monoclinic, Cs_2WO_4 [40] is isomorphous with orthorhombic β-K_2SO_4. The building unit for them are all individual WO_4 tetrahedra. Cu_2WO_4 [41] single crystals were obtained by the high-temperature reaction of $CuWO_4$ and copper. It crystallizes in $P1$ space group. Four edge-shareing WO_6 form W4 clusters (**Figure 1.3**). Ag_2WO_4 [42] has three different crystallorgraphic forms α, β and γ which is in orthorhombic, hexagonal and cubic crystal system, respectively. Hg_2WO_4 [43] is isotypic with the low-temperature modification of Hg_2MoO_4. It crystallizes in $C2/c$ and the crystal structure is octahedra linked via common edges to form zigzag chains (**Figure 1.4**). Three phase-transformations and the crystal data of four phases (α, β, γ and δ) for Tl_2WO_4 were reported [44-45]. The room-temperature γ phase is considered to be the first example of the glaserite-structure type and in trigonal $P\overline{3}m1$.

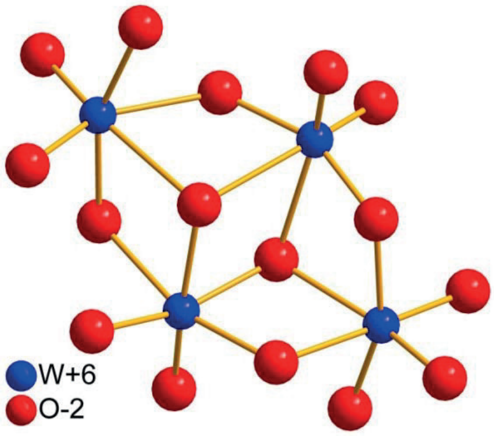

Figure 1.3: W4 cluster in the crystal structure of Cu_2WO_4.

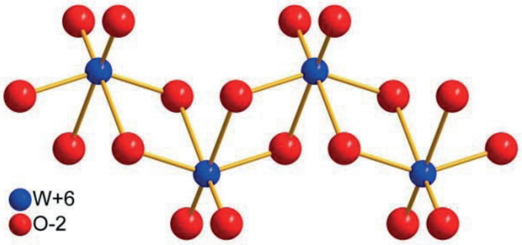

Figure 1.4. Zigzag chain in the crystal structure of Hg_2WO_4.

1.4.2. Monometallic tungstates with +2 cations

RWO_4 and R_3WO_6 where R is an alkaline earth or other divalent element are the most common forms in bivalent metal tungstates. RWO_4 are the most well established chemical compounds because they are the main composition of natural tungsten ores. They are formed by the mineral scheelite and wolframite [1].

Calcium tungstate $CaWO_4$ has very interesting luminescence [46] and structural properties [47] with the mineral name scheelite. The scheelite structures (**Figure 1.5**) with tungsten in tetrahedral coordination are formed with the large bivalent cations (≥ 0.1 nm). It crystallizes tetragonal with space group $I4_1/a$. $SrWO_4$, $BaWO_4$ and $PbWO_4$ have the same structure type [48-50].

Alternatively, with small cations (< 0.1 nm) such as Mg, Mn, Fe, Co, Ni, Cu, Zn and Cd, the wolframite structures [47,51-52] are formed with tungsten in octahedral coordination as shown in **Figure 1.6**. They have been studied for their wide applications such as multiferroic materials [53], scintillation detectors [54], catalysts [55], electrochromic materials [56] and the dye-sensitized solar cells [57]. They crystallize with monoclinic $P2/c$ structure but $CuWO_4$ with lower symmetry triclinic P-1 because of the Jahn-Teller distortion of Cu^{2+} ion [58]. In the wolframite structure, both R^{2+} and W^{6+} are coordinated by six oxygen atoms in a highly distorted octahedral geometry. The tungsten-centered octahedra share edge to form zigzag chains and so do R-centered octahedra. These two types of chains connected each other via corner sharing. $HgWO_4$ [59] does not belong to wolframite or scheelite structure. The data were obtained from neutron powder diffraction and the structure crystallizes in monoclinic $C2/c$ space group. The structure consists of the zigzag chains formed by edge-sharing WO_6 which is the same as the connection of wolframite. However, the coordination of mercury and the distortion of WO_6 make it different. $SnWO_4$ [60-61] has two modifications with phase-transition at 940 K. The low-temperature α-form is orthorhombic with space group *Pnna*. Rapid quenching from above 940 K yields the β-form which is cubic with $P2_13$.

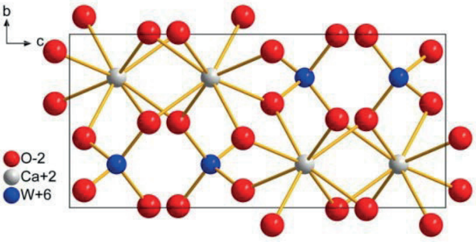

Figure 1.5: The scheelite structure.

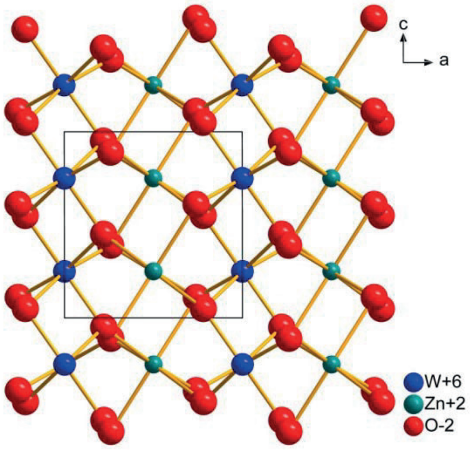

Figure 1.6: The wolframite structure.

A new class containing higher concentration of divalent metals is R_3WO_6 (R = Ca, Sr, Ba) [62]. The crystal structure of Ca_3WO_6 (**Figure 1.7**) was assigned to space group $P2_1$ [63]. Sr_3WO_6 has four polymorphs α, β, γ and δ on going from low to high temperature [64]. Ba_3WO_6 has a structure approaching cubic symmetry. They all can be considered as double perovskites ($A_2BB'O_6$). Cu_3WO_6 [65] has the symmetry of cubic with space group $Pa\bar{3}$. The structure (**Figure 1.8**) is composed of distorted WO_6 octahedra and CuO_5 triangular bipyramids sharing coners and edges in a rather complicated way.

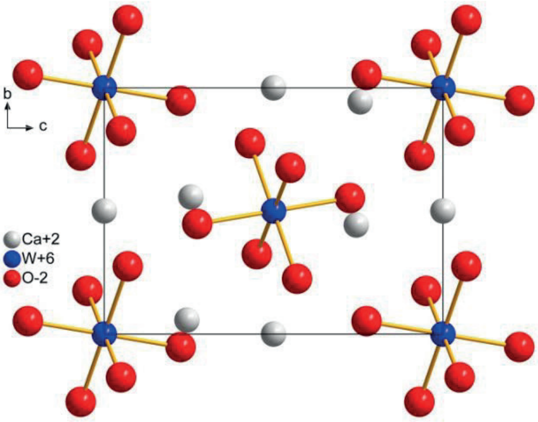

Figure 1.7: The crystal structure of Ca_3WO_6.

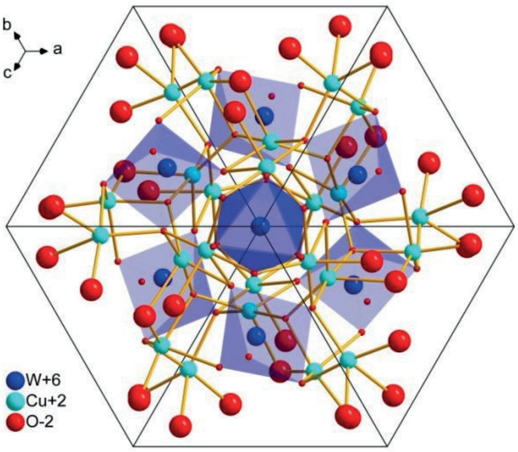

Figure 1.8: The crystal structure of Cu_3WO_6.

1.4.3. Monometallic tungstates with +3 cations

There are a series of trivalent metal tungstates. For example, the system Ln_2O_3-WO_3 has compounds with the molar ratio of 3 : 1, 5 : 2, 3 : 2, 1 : 1, 2 : 3, 1 : 2, 1 : 3 or 1 : 4 [66]. $M_2(WO_4)_3$ (1 : 3), M_2WO_6 (1 : 1) and M_6WO_{12} (3 : 1) where M is a rare earth metal or other trivalent element are more common.

Nassau et al. [67-69] reported a series of trivalent tungstates $L_2(WO_4)_3$ where L is Ln, Y, Sc, In, Fe, Cr, Al. According to ionic radius and temperature, they can be divided into A with *C*2/*c* and C with *Pnca* family structures. The orthorhombic tungstates have the framework with corner-sharing MO_6 and WO_4 polyhedra. As ionic radius increases, the coordination number of M changes from 6 to 8. The structure also becomes edge-sharing with monoclinic symmetry [70]. This class of tungstates attracts considerable interest mainly because of their negative thermal expansion properties [70-74]. Dilanthanide tungstates Ln_2WO_6 were reviewed by Blasse [75]. They can be separated into two group M_2WO_6 (M = Pr – Dy) with (4) La_2MoO_6-type and M_2WO_6 (M = Ho – Lu, Y) (6) with Bi_2NbO_5F-type and the number in front indicates tungsten coordination.

V_2WO_6 [76] and Cr_2WO_6 [77-78] have the trirutile structure and appear in *P*4$_2$/*mnm*. Fe_2WO_6 crystallizes in *Pbcn* and the structure contains zigzag chains formed by corner-sharing MO_6 (M = Fe, W). Sb_2WO_6 [79] crystallizes in triclinic *P*1 and the structure is built up by the $[WO_4]_n$ layers of WO_6 octahedra sharing corner sandwiched by two $[Sb_2O_2]_n$ layers. Bi_2WO_6 [80] is the composition of the mineral russellite. It is orthorhombic *Pca*2$_1$ and consists of WO_6 corner-shared layer sandwiched between the layers of bismuth and oxygen (**Figure 1.9**). It has been studied because of the interesting properties such as photocatalytic activity, ferroeletricity, piezoelectricity, and nonlinear dielectric susceptibility [80].

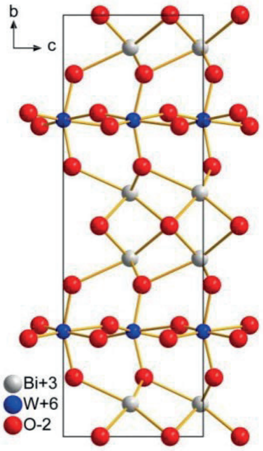

Figure 1.9: The crystal structure of Bi_2WO_6.

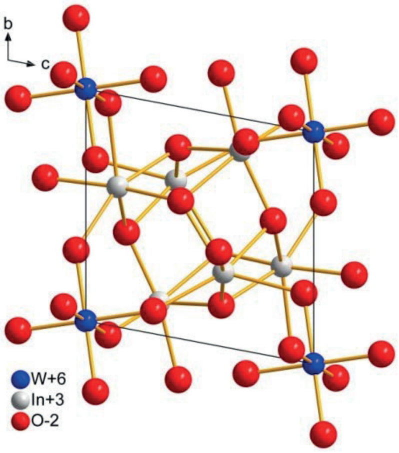

Figure 1.10: The structure of In_6WO_{12}.

The M_6WO_{12} (M = Ln, Y) [81] were all related to the fluorite structure and their symmetries depend on the size of cation. When M = La – Pr, the structure is cubic or pseudo-cubic; when M = Nd – Gd, it is pseudo-tetragonal and when M = Tb – Lu, Y, it is rhombohedral. The specific character of In_6WO_{12} (**Figure 1.10**) lies in the isolated WO_6 octahedral units at the corner of the cell which is in space group $R\overline{3}$.

1.4.4. Monometallic tungstates with +4 cations

Isostructural ZrW_2O_8 and HfW_2O_8 [82] have been intensively studied because of the strong negative thermal expansion from 0.3 K to 1050 K. Below 428 K, ZrW_2O_8 adopts $P2_13$ containing corner-sharing ZrO_6 and WO_4. Above the phase-transition, it becomes $Pa\overline{3}$ with one oxygen site half occupied.

1.4.5. Monometallic tungstates with +5 cations

Nb_2WO_8 [83] and Ta_2WO_8 [84] are isostructural and crystallize in space group *Pbcm*. In the structures, 5/6 metal cations are octahedrally coordinated and remaining cations are coordinated with seven oxygen atoms in a pentagonal-bipyramids configuration.

1.4.6. Bimetallic tungstates

There are plenty of bimetallic tungstates well investigated. They have anions WO_6^{6-} [85-86], WO_9^{12-} [87-88], $W_2O_8^{4-}$ [88], $W_2O_9^{6-}$ [89-90], $W_3O_{12}^{6-}$ [91] and $W_3O_{16}^{14-}$ [92] etc. According to the valence of anion group, several possibilities of cation combination can be found. For example, the compounds containing WO_6^{6-} group has two types: A(I)M(V)WO_6 (A = Li, Na, K, Rb, Cs, Tl and M = V, Nb, Ta, Sb) [85,93-96] and $R(II)_2R'(II)WO_6$ (R = Ca, Sr, Ba, Pb and R′ = Mg, Ca, Sr, Cr, Mn, Fe, Co, Ni, Cu, Zn, Pd, Cd) [97-112]. The first type compounds composing of an anion group with –6 oxidation state, a +1 cation and a +5 cation also can be considered as bronzoids. The second type is known as double perovskite structure. $R'O_6$ and WO_6 octahedral tilting modifies the coordination environment of R-site cation and lowers the symmetry of the crystal structure [113].

1.5. Motivation

The tungsten compounds reviewed above are under continued interest because of their crystal chemical and physical properties. However, in contrast to the rapidly growing interest on other metals with +5 oxidation state like Nb and Ta tungstates, arsenic as a heteroatom in tungstates is quite limited. In a phenomenological model it was shown that for oxides a correlation exists between the absence of an inversion center in the crystal structure and the shortest M–O bond length [114-115]. Therefore, formation of a NCS crystal could be possible within the range of respective M–O values. The model includes a wide range of known NCS binary and ternary oxides along with tungstates and arsenates. Considering the known M–O distances for WO_x and AsO_y coordinations the model helped guide to synthesize the new NCS crystal $K[AsW_2O_9]$ crystallizing in space group $P2_12_12_1$ [116]. In this case, the observed mean W–O and As–O bond distances lie within the range of the M–O maps designed for the formation of NCS tungstates and arsenates [114]. To further tune the NLO susceptibility this research study was motivated to (i) expand the member of the $K[AsW_2O_9]$ family replacing K^+ by other alkali metal cations such as Na^+ and Li^+, assuming a possible elongation/contraction of the M–O bond distances, (ii) study on the crystal chemical properties of this novel family, and (iii) change the molar ratio of raw material to expand the system in the phase diagram K_2O-As_2O_5-WO_3 and attempt to find new materials in this family.

Chapter 2 Experimental methods

2.1. Synthesis

There are a rising variety of methods to prepare new materials along with their growing interesting properties. The solid-state reaction or so-called the ceramic method [117] is the simplest and most widely used method of preparing polycrystalline samples. It is a reaction of stoichiometric mixture of reagents at high temperature. This method has many advantages like low costs, availability of precursors and easy to carry out the synthetic procedure both industrially and in the laboratory. However, to get pure powder samples, it becomes fairly complex considering the factors like temperature, heating and cooling rate, crucibles and purification etc. It is necessary to grind the reactants thoroughly to achieve a homogeneous mixture. Containers should stand at high temperatures and not react with the reagents.

Single crystals can be prepared by flux growth which is one of solution methods. The powders with the same components of desired single crystals are dissolved in a proper flux at high temperature, and then the saturated solution slowly cool down till single crystals form.

2.2. Raw materials

KNO_3	EMD Millipore, ≥ 99 %
$NaNO_3$	Carl Roth, ≥ 99 %
$LiNO_3$	Alfa-Aesar, 99 %
$As_2O_5 \cdot H_2O$	Sigma-Aldrich, 98 %
WO_3	Sigma-Aldrich, ≥ 99 %
$NH_4H_2AsO_4$	ABCR, 98 %

2.3. Instruments and equipment

2.3.1. Single crystal X-ray diffractometer

The single crystal X-ray diffraction (SCXRD) data were collected using D8 Venture diffractometer (Bruker AXS GmbH, Karlsruhe) equipped with a KAPPA four-circle goniometer, the PHOTON 100 detector (based on CMOS technology provided an active area of 100 cm^2), and the curved graphite crystal TRIUMPH monochromator giving Mo $K_{\alpha1,2}$ ($\lambda_{\alpha1}$ = 70.9300(3) pm, $\lambda_{\alpha2}$ = 71.3574(2) pm) radiation.

2.3.2. Powder X-ray diffractometer

X-pert:

The room-temperature powder X-ray diffraction (PXRD) data were collected using a MPD diffractometer (Panalytical, Almelo) with Bragg-Brentano geometry, a X'Celerator multi strip detector, and a secondary Ni filter giving Cu $K_{\alpha1,2}$ ($\lambda_{\alpha1}$ = 154.05929(5) pm, $\lambda_{\alpha1}$ = 154.4414(2) pm) radiation. The temperature-dependent experiments were performed with the same instrument adapting an Anton Paar-HTK1200N heating chamber in the diffractometer.

PW1800:

A small part of PXRD data for phase diagram were collected using the Philips PW1800 diffractometer with Bragg-Brentano geometry, a PW1711 proportional detector, and a graphite monochromator giving Cu $K_{\alpha1,2}$ radiation.

2.3.3. Time-of-flight powder neutron diffractometer

Time-of-flight (TOF) powder neutron diffraction (PND) data were collected on the Powgen high-resolution powder diffractometer at the Spallation Neutron Source (SNS), Oak Ridge National Laboratory (ORNL), USA. For the low-temperature measurements, the Powgen Automatic Changer (PAC) has a carousel that holds a maximum of 24 sample-filled vanadium cans of 8 mm diameter and collects data in the temperature range between 10 and 300 K. The ILL furnace built with vanadium heating elements is available for high-temperature measurements from room-temperature till 900 K.

2.3.4. Scanning electron microscope

Energy dispersive X-ray spectroscopy (EDX) data were collected in a JSM-6510 Scanning electron microscope (SEM) instrument equipped with XFlash Detector 410-M.

2.3.5. The Fourier transform infrared spectrometer

The Fourier transform infrared spectra (FTIR) were carried out on a Bruker VERTEX80v spectrometer.

2.3.6. Raman spectrometer

The Raman spectra were recorded on a Horiba LabRam Aramis spectrometer equipped with lasers worked at the wavelength of 532 nm (Nd-YAG-laser), 633nm (He-Ne-laser) and 785nm (Dioden-laser). A T95-HT system controller, a Linkam TS1500 heating stage and an ECP water circulator pump were used for high-temperature and A T95-PE system controller, a THMS350V cooling stage and an LNP95 liquid nitrogen pump system were used for low-temperature measurements respectively.

2.3.7. Ultraviolet-visible spectrophotometer

Ultraviolet-visible (UV-vis) diffuse reflectance measurements were obtained on a Shimadzu UV-vis spectrophotometer UV-2600 equipped with an ISR-2600 plus two-detector integrating sphere.

2.3.8. Electrochemical Impedance spectrometer

Electrochemical impedance spectroscopy (EIS) measurements were carried out using Novocontrol Alpha-A spectrometer in two-wire mode. The sample pellets were located in a high-temperature sample holder NorECs ProboStat and relatively lower temperature glass tube sample holder in ESPEC SH-221 chamber.

2.3.9. Thermal analyzer

Simultaneous thermal analyses (TG-DSC) were carried out under dry synthetic air atmosphere (80 vol% N_2 and 20 vol% O_2) with the heating rate of 10 K/min up to 1473 K on a Netzsch STA 449 F3 Juptier thermal analyzer.

2.3.10. Second harmonic generation apparatus

Second harmonic generation (SHG) in the sample was excited by 0.6 ns pulsed radiation of a Nd:YAG laser (STA-01-7, Standa) working at $\lambda = 1064$ nm with 100 mW mean power. The SHG signal at $\lambda = 532$ nm was selected by a collimator and a monochromator and recorded by a photomultiplier.

Chapter 3 Novel alkali-metal arsenotungstates*

3.1. Introduction

According to the transmittance wavelength range, nonlinear optical (NLO) crystals can be divided into groups optimal for applications over ultraviolet, visible and near and far infrared regions. For the former two types, well investigated and widely used compounds like β-BaB_2O_4 [118-119], LiB_3O_5 [120] and $KTiOPO_4$ [121] were reported. However, for the far infrared region the known compounds still have many limitations for practical applications, thus exploring suitable mid- and far-infrared nonlinear optical materials is a challenge. Oxide NLO crystals are preferably used in modern high-power laser systems because of their higher optical damage threshold. In oxide containing crystals, the appropriate cation selection may result in a noticeable shift of the infrared cut edge to suitable wavelengths for particular usages. As an example, in the $KTiOPO_4$ compound, substitution of the P^{5+} by As^{5+} results in $KTiOAsO_4$ with an optical transmission range up to ~ 5 μm which is ~ 1 μm higher than that in $KTiOPO_4$ [122-123].

Non-linear optical properties are correlated with local or global non-centrosymmetric (NCS) crystal structures. Due to second-order Jahn-Teller effects, octahedrally coordinated d^0 transition metal W^{6+} cations can cause distortions leading to NCS symmetry. Introducing additional foreign cations with different radii into the tungstate framework may increase the degree of octahedral distortion leading to structural modification as well as change the NLO properties. Notably, in the past decade many NCS tungstates such as $BaTeW_2O_9$ [124], $Na_2TeW_2O_9$ [89], $(NH_4)_2Te_2W_2O_8$ [125], $KNbW_2O_9$ and $RbNbW_2O_9$ [32] have been of considerable interest because of their second-harmonic generation (SHG), piezoelectric, pyroelectric and ferroelectric properties. Besides, many complex tungstates are proposed as effective rare-earth-doped host materials applicable in femtosecond and integrated laser systems [126-129]. It seems to be a promising way to search for new As-containing NCS tungstates to create new laser crystals with improved optical properties. To further tune the NLO susceptibility we tried to replace K by Na and Li in the $K[AsW_2O_9]$ system. The isotypic $Na[AsW_2O_9]$ and a novel structure of composition $Li_3AsW_7O_{25}$ instead of the proposed $Li[AsW_2O_9]$ were obtained. In this chapter, the syntheses, structures and characterizations of these two new compounds are described.

---

*The two novel arsenotungstates are both published and most of the tables and figures in this chapter are reprinted from reference [130-131].

3.2. Synthesis, structure and characterizations of Na[AsW_2O_9]

3.2.1. Synthesis

Single crystals of Na[AsW_2O_9] were synthesized using $NaNO_3$, WO_3 and $As_2O_5\cdot H_2O$ in the molar ratio 1 : 2 : 6. The mixture was intensively ground in a mortar and heated in a platinum crucible at 1023 K for 24 h followed by cooling (~ 50 K/h) down to room-temperature. Pale greenish needle-like single crystals were produced as shown in **Figure 3.1**. Pure dark greenish powder samples were synthesized using stoichiometric mixtures with respect to the metal cations of $NH_4H_2AsO_4$, $NaNO_3$ and WO_3 at similar condition.

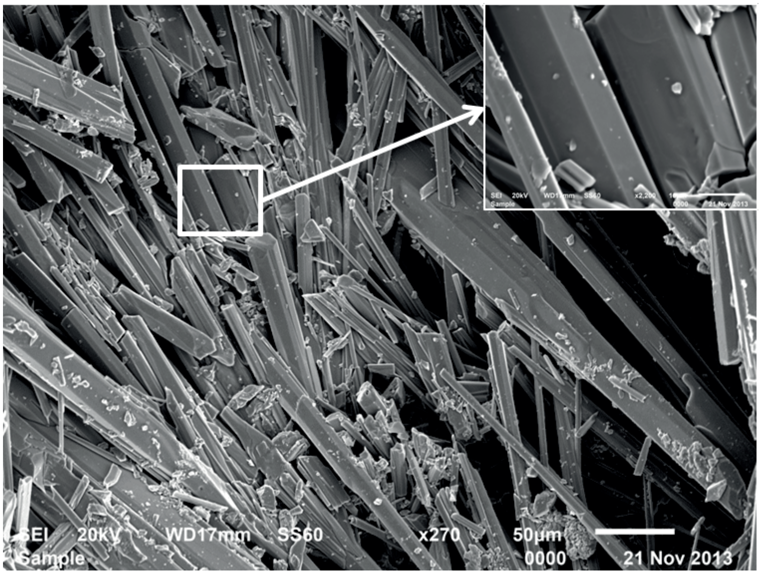

Figure 3.1: Scanning electron microscope image of Na[AsW_2O_9] single crystals.

Because of the isotypic structures of K[AsW_2O_9] and Na[AsW_2O_9] and the channels of the open framework are large enough to locate larger alkali metal ions K^+; there is a possibility that both are located in the same framework. The mixture synthesis was also tried to see the replacement of two alkali metals. Using KNO_3, $NaNO_3$, $NH_4H_2AsO_4$ mixed with WO_3 in the ratio of 1 : 1 : 2 : 4, fine grounded and put into the furnace 500 K/h heated up to 1023 K for 24 hours and then cooling down to room-temperature in the speed of 50 K/h.

3.2.2. Structure

Single crystal X-ray diffraction data were collected and a semi-empirical approach was applied for absorption correction of equivalent reflections. The structure was solved by direct methods and refined on F^2 by full-matrix least-squares calculations using the SHELX97 program package [132]. Details of the structural features are given in **Table 3.1**.

Table 3.1: Crystal data obtained from the single crystal X-ray diffraction of $Na[AsW_2O_9]$.

Empirical formula	$Na[AsW_2O_9]$
Formula weight	609.61
Temperature	304(2) K
Crystal system	Orthorhombic
Space group	$P2_12_12_1$
Unit cell dimensions	a = 491.13(2) pm b = 872.38(4) pm c = 1645.85(6) pm
Volume	$705.17(5)\times10^6$ pm^3
Z	4
Density (calculated)	5.742 g/cm^3
Absorption coefficient	37.341 mm^{-1}
F(000)	1056
θ for data collection	2.475- 38.678°
Indices ranges	$-8 \le h \le 5$, $-15 \le k \le 13$, $-22 \le l \le 28$
Reflections collected/unique	7681/3745
Refinement method	Full-matrix least-squares on F^2
GOF on F^2	1.029
Final R indices $[I > 2\sigma(I)]$	$R1 = 0.0371$ $wR2 = 0.0568$
R indices (all data)	$R1 = 0.0516$ $wR2 = 0.0606^a$
Largest diff. peak and hole	2.151 and -2.450 e A^{-3}

CSD No. 428393.

[a] $R1 = \sum(|F_o| - |F_c|)/\sum|F_o|$; $wR2 = \{\sum[w(|F_o|^2 - |F_c|^2)^2]/\sum[w(|F_o|^2)^2]\}^{1/2}$.

The X-ray powder diffraction was carried out at ambient condition from 3° and 140° 2θ with a step size of 0.0167° and a data collection time 110 s/step. The fundamental parameter approach, where the fundamental parameters were fitted against a LaB_6 standard material, was applied for the Rietveld refinement using “DiffracPlus Topas 4.2” software (Bruker AXS GmbH, Karlsruhe). For this purpose, the starting atomic coordinates were taken from the results of the single crystal diffraction data refinements. The atomic coordinates, equivalent isotropic and anisotropic displacement parameters obtained from single crystal and powder X-ray diffraction data are given in **Table 3.2** and **Table 3.3**, respectively.

Table 3.2: Atomic coordinates, equivalent isotropic and anisotropic displacement parameters of Na[AsW_2O_9] obtained from single crystal and powder X-ray diffraction data.

Single crystal X-ray diffraction

Atom	Occupancy	Wyckoff	*x*	*y*	*z*	U_{eq} /10^4×pm^2
W1	1	4a	0.34997(5)	0.12012(3)	0.044834(15)	0.00631(6)
W2	1	4a	0.12064(5)	0.39034(3)	0.345988(15)	0.00563(6)
As1	1	4a	0.36274(16)	0.72944(7)	0.27103(4)	0.00515(12)
Na1	1	4a	0.6999(10)	0.0144(5)	0.3894(3)	0.0332(11)
O1	1	4a	0.0360(11)	0.7478(7)	0.0990(4)	0.0124(11)
O2	1	4a	0.2204(12)	0.0028(7)	0.9726(3)	0.0130(11)
O3	1	4a	0.4843(10)	0.7698(6)	0.3626(3)	0.0082(10)
O4	1	4a	0.2785(10)	0.5458(5)	0.2572(3)	0.0079(9)
O5	1	4a	0.0957(10)	0.8463(6)	0.2558(3)	0.0113(10)
O6	1	4a	0.5951(12)	0.7531(6)	0.1958(3)	0.0115(10)
O7	1	4a	0.1372(12)	0.0505(5)	0.1321(3)	0.0107(9)
O8	1	4a	0.1458(11)	0.2960(5)	0.0237(3)	0.0081(9)
O9	1	4a	0.6421(12)	0.9749(5)	0.0800(3)	0.0099(9)

Anisotropic displacement parameters (/10^4×pm^2) of single crystal X-ray diffraction data

Atom	U_{11}	U_{22}	U_{33}	U_{23}	U_{13}	U_{12}
W1	0.00596(10)	0.00666(10)	0.00632(11)	0.00007(10)	-0.00144(9)	-0.00053(10)
W2	0.00595(10)	0.00527(9)	0.00568(10)	0.00077(10)	0.00047(9)	0.00125(10)
As1	0.0056(3)	0.0047(2)	0.0051(3)	0.0004(2)	-0.0008(3)	-0.0001(3)
Na1	0.050(3)	0.0257(19)	0.024(2)	0.0068(18)	-0.0115(19)	-0.021(2)
O1	0.011(2)	0.013(2)	0.014(3)	0.003(2)	0.006(2)	0.0043(19)
O2	0.016(3)	0.013(2)	0.010(2)	-0.003(2)	0.002(2)	-0.001(2)
O3	0.009(2)	0.010(2)	0.005(2)	0.0027(19)	-0.0042(17)	-0.0003(18)
O4	0.010(2)	0.0053(19)	0.009(2)	0.0014(19)	0.0010(19)	-0.0036(17)
O5	0.007(2)	0.014(2)	0.013(2)	0.002(2)	-0.0031(19)	0.0062(19)
O6	0.016(3)	0.011(2)	0.007(2)	0.0011(19)	0.005(2)	0.002(2)
O7	0.016(3)	0.0042(18)	0.012(2)	0.0010(17)	0.001(2)	-0.002(2)
O8	0.009(2)	0.0074(18)	0.008(2)	0.0026(17)	-0.0043(19)	0.002(2)
O9	0.011(2)	0.0090(19)	0.010(2)	0.0040(18)	0.000(2)	0.003(2)

Table 3.3: Cell parameters, atomic coordinates and displacement parameters of Na[AsW_2O_9] obtained from powder X-ray diffraction data Rietveld refinement.

a = 491.280(7) pm, b = 872.18(1) pm, c = 1648.10(2) pm, V = 706.18(2)×10^6 pm^3

Atom	Occupancy	Wyckoff	x	y	z	B_{eq} /10^4×pm^2
W1	1	4a	0.35141(60)	0.11902(25)	0.04465(10)	0.388(22)^a
W2	1	4a	0.88494(53)	0.88928(23)	0.15426(10)	0.388^a
As1	1	4a	0.3557(15)	0.72727(43)	0.27047(23)	0.388^a
Na1	1	4a	0.6884(47)	0.0084(15)	0.38363(74)	0.84(34)
O1	1	4a	0.0078(65)	0.7569(26)	0.0982(12)	2.63(54)^b
O2	1	4a	0.1132(99)	0.2979(24)	0.0211(12)	2.63^b
O3	1	4a	0.6183(71)	0.7791(22)	0.1950(11)	0.25(22)^c
O4	1	4a	0.2488(56)	0.5507(22)	0.2483(12)	0.25^c
O5	1	4a	0.1031(64)	0.8336(22)	0.2781(11)	0.25^c
O6	1	4a	0.6788(80)	0.9522(21)	0.1213(12)	0.25^c
O7	1	4a	0.1233(83)	0.0515(21)	0.1323(11)	0.25^c
O8	1	4a	0.7240(64)	0.5078(19)	0.0313(11)	0.25^c
O9	1	4a	0.9763(52)	0.0937(26)	0.0416(13)	0.25^c

[a, b, c] Values with the same letters were constrained to each other during the refinements.

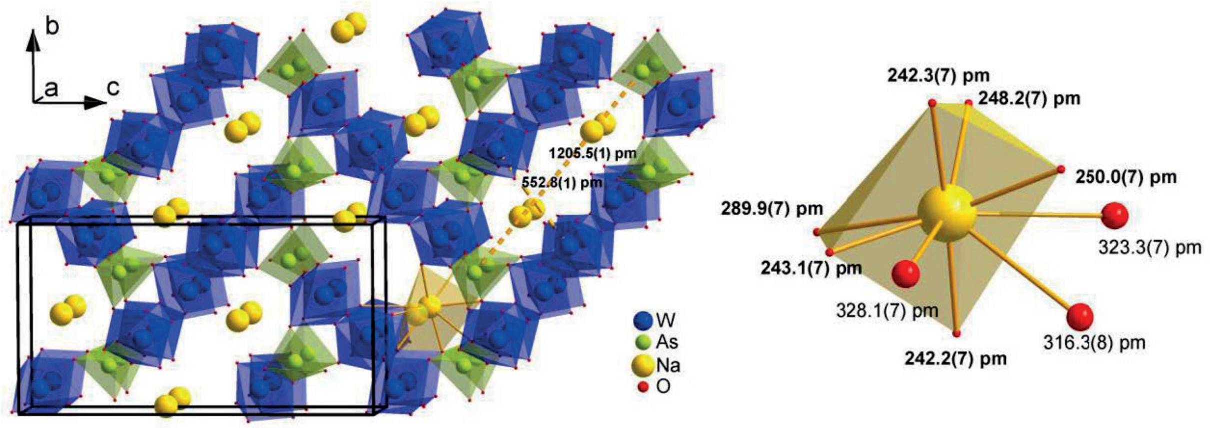

Figure 3.2: Crystal structure of Na[AsW_2O_9] along the **a**-direction and the coordination environment of Na^+ cation.

The crystal structure of Na[AsW_2O_9] is isotypic with K[AsW_2O_9] [116]. That is, in the orthorhombic system ($P2_12_12_1$) the corner-sharing WO_6 octahedra and AsO_4 tetrahedra form the three-dimensional framework as shown in **Figure 3.2**. The powder data Rietveld refinement results, shown in **Figure 3.3**, agree well with those obtained from the single crystal data analysis, however, the c-cell parameter slightly differs from each other as well as the cell volume (V) within standard deviation. Comparing with K[AsW_2O_9] [116], the metric parameters decrease by 1.27(1) %, 4.95(1) %, 1.34(1) % and 7.42(1) % for *a*, *b*, *c* and *V*, respectively.

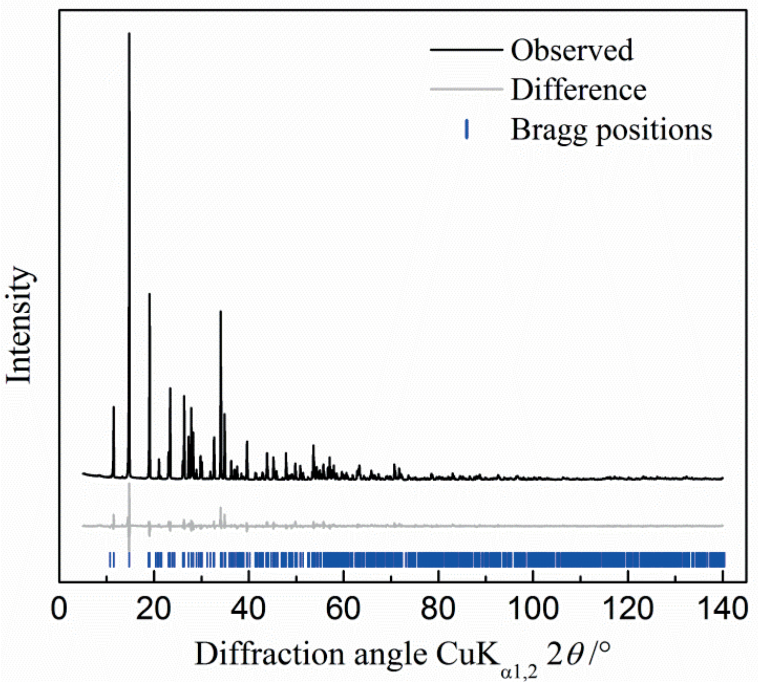

Figure 3.3: Rietveld plot of X-ray powder diffraction of Na[AsW_2O_9].

The W−O bond lengths are in the range between 169.3(6) pm and 216.6(5) pm, the As−O bond lengths between 165.8(5) pm and 169.7(5) pm. Na^+ cations are coordinated by six oxygen atoms within a Na–O cut-off distance of 300 pm (**Figure 3.2**). These six oxygen atoms contribute to the bond valence sum (BVS) [133] with 0.92(1) valence units (v.u.). Taking the next farther three oxygen atoms 316.3(8) pm, 323.3(7) pm and 328.1(7) pm) into account the BVS increases to 0.98(1) v.u. showing the expected charge of the sodium cation. Thus, these farther oxygen atoms must be regarded close to the first coordination shell, which slightly contribute to Na–O bonding. The sodium atoms are therefore 9-fold (6 + 3) coordinated, and resides in the channel that runs along the **a**-direction (**Figure 3.2**). The cross-section of the channel is elongated with a dimension of about 290 pm × 600 pm. The shortest Na–O bond distance has been reduced to about 7.7(1) % compared with the corresponding K–O distance in K[AsW_2O_9] [116]. As a consequence, the one-dimensional channel elongated along the direction with a perpendicular shrinkage. For example, the distance between two As-atoms changes from 1185.3(3) pm to 1205.5(1) pm, and the distance between two W-atoms changes from 635.1(2) pm to 552.83(4) pm while replacing

K^+ by Na^+ cation (see arrow, **Figure 3.2**). These changes cause an overall contraction of the metric parameters, in particular, the significant reduction of *b*-cell parameter.

To describe the polyhedral distortions [134] the mean quadratic elongation (λ_Q) is a convenient measure. We calculated λ_Q for both WO_6 octahedra and AsO_4 tetrahedra in the $Na[AsW_2O_9]$ and $K[AsW_2O_9]$ compounds, and the results are given in **Table 3.4**. λ_Q for the $W1O_6$ octahedra remained unchanged between $Na[AsW_2O_9]$ and $K[AsW_2O_9]$. However, both $W2O_6$ octahedra and AsO_4 tetrahedra in $Na[AsW_2O_9]$ comprise with slightly a higher distortion than that in the corresponding polyhedra in $K[AsW_2O_9]$. Clearly, both AsO_4 and WO_6 polyhedra conform to their rigid-unit like behaviors in the framework even with a sizable shrinkage of the channel dimension due to smaller Na incorporation. Thus, using a smaller alkali metal cation causes a slightly distorted NCS structure of this compound family, which seems to be an important factor to explain the associated NLO property.

Table 3.4: Mean quadratic elongation (λ_Q) of polyhedra in $Na[AsW_2O_9]$ and $K[AsW_2O_9]$.

Compound	$W1O_6$	$W2O_6$	AsO_4
$Na[AsW_2O_9]$	1.019(1)	1.019(2)	1.007(1)
$K[AsW_2O_9]$[a]	1.019(2)	1.015(1)	1.004(1)

[a] Crystal data of $K[AsW_2O_9]$ are taken from ref. [116].

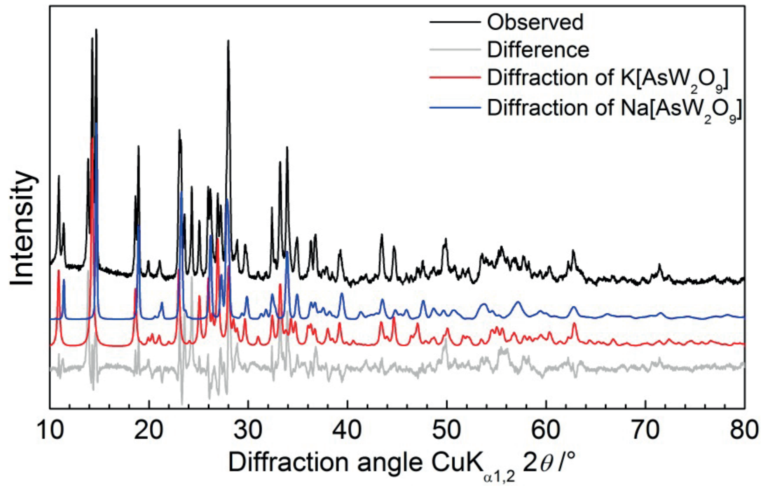

Figure 3.4: The X-ray powder diffraction pattern and Rietveld plot of mixture products.

The X-ray powder diffraction for the mixture products was carried out at ambient condition from 3° to 80° 2*θ* with a step size of 0.0167° and a data collection time 30 s/step. **Figure 3.4** depicts the X-ray Rietveld plot, showing identification of two phases, namely,

$K[AsW_2O_9]$ and $Na[AsW_2O_9]$ Therefore, attempts to produce a solid solution of $Na_{0.5}K_{0.5}[AsW_2O_9]$ with the structure coexisting K^+ and Na^+ in the channels using conventional solid-state reaction did not work.

3.2.3. Spectroscopy

The Fourier transform infrared (FTIR) absorption spectra were measured both for the far-infrared (FIR, 30–950 cm^{-1}) and the mid-infrared (MIR, 370–4000 cm^{-1}) region. The MIR spectrum was collected using the standard KBr method (1 mg sample in 200 mg KBr), obtained from 32 scans with a spectral resolution of approx. 2 cm^{-1}. For the FIR spectrum recording, a polyethylene pellet (2 mg sample in 50 mg PE) was used, obtained from 16 scans. To get a continuous whole range spectrum, the FIR spectrum was adjusted to the MIR.

Raman spectra were collected using a pressed powder pellet of 5 mm diameter. The spectrum was recorded using a laser of 532 nm wavelength. Data were collected between 80 cm^{-1} and 1000 cm^{-1} with a spectral resolution of approx. 3.2 cm^{-1} using a grating of 1800 grooves/mm. Both the FTIR and Raman spectra were baseline corrected for peak fitting performed using the LabSpec Version 5 software package. Component analysis was carried out using pseudo-Voigt functions.

The infrared and the Raman spectra along with the fitted components are presented in **Figure 3.5**; the band maxima are given in **Table 3.5**. Factor group analysis leads to 156 Raman active ($39A + 39B_1 + 39B_2 + 39B_3$) and 114 IR active ($39B_1 + 39B_2 + 39B_3$ – acoustic ($B_1 + B_2 + B_3$)) modes. Fitting the observed IR spectrum, however, requires only 44 bands and the Raman spectrum requires 30 bands. Selected bands are assigned (**Table 3.5**) based on the comparative frequency values (uncertainty of ± 1 cm^{-1}) observed for the respective coordination. For example, for the AsO_4^{3-} unit with site symmetry *C*1 nine bands are assigned which are both IR and Raman active: A (ν_1 symmetrical stretching mode), 2A (ν_2 symmetrical bending modes), 3A (ν_3 asymmetrical stretching mode), 3A (ν_4 asymmetrical bending modes). In the infrared spectrum, well resolved band maxima were observed at 370 cm^{-1}, 406 cm^{-1}, 433 cm^{-1} and 456 cm^{-1} and assigned to bending vibration of AsO_4 group. The line observed at 788 cm^{-1} refers to symmetric stretching vibration of AsO_4 group, and those at 833 cm^{-1}, 877 cm^{-1}, and 893 cm^{-1} are associated with the asymmetric stretching vibration of AsO_4 group [135]. The bands at 541 cm^{-1} and 983 cm^{-1} are assigned to the vibration of terminal W=O bond. Raman band at 972 cm^{-1} can be attributed to the stretching mode of the terminal bond W=O, which lies close to the frequency observed in the IR spectrum.

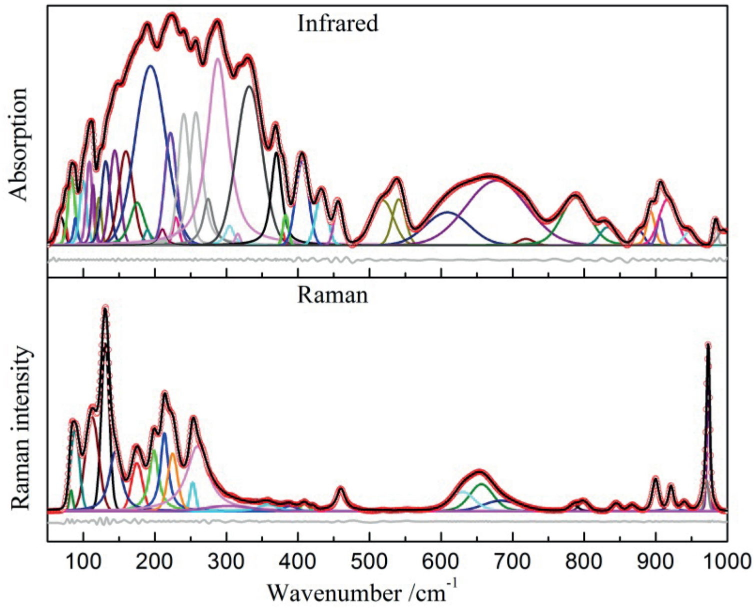

Figure 3.5: Observed and fitted Infrared and Raman powder spectra of Na[AsW_2O_9] showing respective band components. The difference curve below the respective spectrum justifies the quality of the fit.

Table 3.5: Fitted infrared and Raman band maxima /cm^{-1}.

Infrared	Raman	Assignment
68.64(3)	--	
75.16(3)	--	
83.50(2)	82.86(2)	
88.95(1)	88.30(3)	
99.73(2)	--	
108.49(3)	--	
113.60(1)	112.20(3)	
121.89(2)	--	
131.35(2)	130.71(3)	
143.95(2)	144.75(1)	
159.52(4)	--	
175.34(1)	174.99(1)	
189.46(3)	--	
194.02(4)	198.62(2)	
210.54(1)	213.32(4)	
221.90(2)	224.80(3)	
229.51(2)	--	
240.53(1)	--	
--	253.00(3)	

257.40(2)	259.50(2)	
274.41(3)	--	
287.99(1)	--	
304.43(3)	302.88(3)	
315.86(2)	--	
331.91(1)	--	
369.89(1)	358.48(2)	bending v_2 of AsO_4
378.56(2)	--	
382.75(1)	388.85(3)	
405.74(1)	409.31(3)	bending v_2 of AsO_4
432.97(2)	421.61(4)	bending v_4 of AsO_4
456.38(4)	460.07(3)	bending v_4 of AsO_4
518.42(3)	--	
540.92(3)	--	vibration of W=O
608.92(1)	--	
--	630.45(1)	
--	656.47(3)	
677.55(4)	--	
--	684.07(3)	
718.55(2)	--	
788.00(4)	785.25(3)	symm. stretch. v_1 of AsO_4
--	799.47(3)	
832.81(4)	844.90(1)	asymm. stretch. v_3 of AsO_4
877.46(1)	866.81(1)	asymm. stretch. v_3 of AsO_4
893.02(2)	899.70(1)	asymm. stretch. v_3 of AsO_4
905.79(1)	--	
916.85(4)	921.31(1)	
946.96(1)	940.04(2)	
--	971.00(2)	
--	972.00(2)	
--	973.59(2)	
983.29(4)	--	vibration of W=O
994.94(4)	--	

The scanning electron microscope (SEM) image and energy dispersive X-ray spectroscopy (EDX) data were collected. The atom ratio of As : W was found to be 1 : 1.8(2) for $Na[AsW_2O_9]$ which is corresponding to the initial chemical composition and in agreement with the refined structure.

3.2.4. Thermal analysis

Simultaneous thermal analyses (TG-DSC) were carried out using 26.7(1) mg sample which was measured relative to an empty corundum crucible as the reference. A drift correction to the data was applied using an empty corundum crucible measurement.

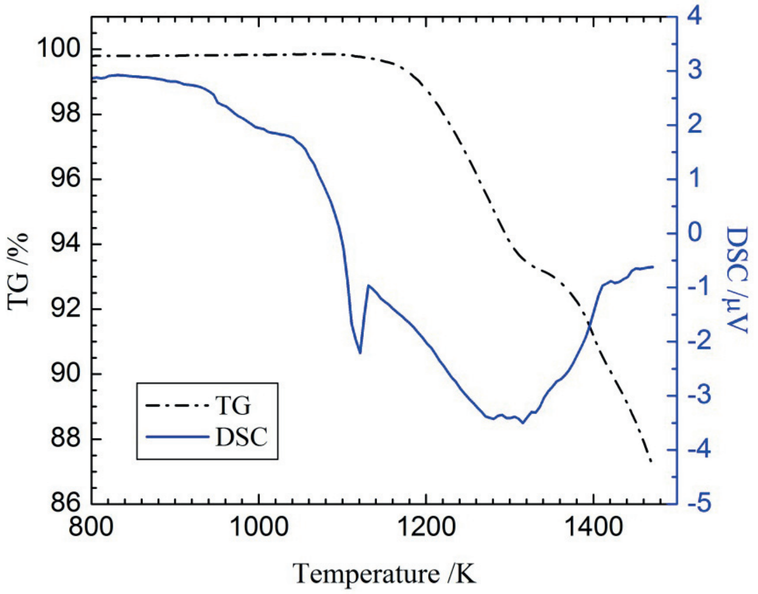

Figure 3.6: Thermogravimetry (TG) analysis and the differential scanning calorimetry (DSC) curve of Na[AsW_2O_9].

Investigating the thermal behavior of the sodium compound the observed TG curve (**Figure 3.6**) displays a two-step weight loss. In the first step, which starts directly after an endothermic signal at 1093(5) K (onset temperature) observed from the DSC data, 6.5(3) wt% were determined. This mass loss corresponds to approx. two oxygen atoms. Second, a continuous mass loss starting at around 1338(5) K is observed. Correlating the first sharp endothermic DSC peak at 1093(5) K with the decomposition of (two formula units) Na[AsW_2O_9] into possible binary oxides of Na_2O, As_2O_5 and 4WO_3. At this temperature As_2O_5 is not stable and might decompose to As_2O_3 and O_2. This oxygen molecule corresponds to the observed mass loss. Taking a boiling point for As_2O_3 of 738 K into account the continuous further mass loss till the end of the experiment corresponds to the evaporation of As_2O_3. We did not investigate the decomposition products. But the remains after TG/DSC experiment were found to be light green. This is in agreement with the color of WO_3. All other possible compounds including sodium-tungstates are white. This further supports the decomposition of the sodium-arsenotungstate to arsenic-oxide and tungsten (VI)-oxide.

3.2.5. Second harmonic generation

The SHG response was analyzed in a back-scattering geometry by means of the modified Kurtz-Perry method [136]. The sample was placed into a platinum container without additional grinding. The experimental signal was corrected for thermal noise background recorded as a signal without the laser pump. The luminescence contributions were controlled by measurements at wavelengths above and below λ = 532 nm. The SHG signal was averaged over the 5×10^5 pump pulses. Quartz powder (α-SiO_2) with well-known nonlinear optical properties was used as a reference material.

The second harmonic intensity at λ = 527 nm generated in Na[AsW_2O_9] has about 45 % intensity of that in α-SiO_2 indicating comparatively low NLO properties. The estimated NLO susceptibility $\chi^{(2)} \sim 0.2$ pm/V is an order of magnitude lower than that in K[AsW_2O_9]. Thus, substitution of K by Na in the K[AsW_2O_9] structure results in significant diminution of the observed NLO signal although the W−O and As−O bond lengths still stay in the potential range of high-rank NLO properties. Since Na[AsW_2O_9] is colored (greenish) compared with its white counterpart K[AsW_2O_9] we explain the lower valued NLO susceptibility of Na[AsW_2O_9] with the associated optical absorption.

3.3. Synthesis, structure and properties of $Li_3AsW_7O_{25}$

3.3.1. Synthesis

$LiNO_3$ (Alfa-Aesar, 99 %), WO_3 (Sigma-Aldrich, ≥ 99 %) and $As_2O_5{\cdot}H_2O$ (Sigma-Aldrich, 98 %) with the molar ratio of 6 : 14 : 1 were mixed in an agate mortar and heated in a platinum crucible for 6 hours at 973 K. Following grinding and heating at 1008 K for another 6 hours yielded in a pale yellow powder. Using flux method, an excess of $As_2O_5{\cdot}H_2O$ was added to pure $Li_3AsW_7O_{25}$ powder in a platinum crucible with the molar ratio of 10 : 1, and heated at 1053 K for 12 h. Cylindrical single crystals were obtained by slowly cooling (50 K/h) down to room-temperature.

3.3.2. Structure

Single crystal X-ray diffraction data were collected and a semi-empirical approach was applied for absorption correction of equivalent reflections. The structure was solved by direct methods and refined on F^2 by full-matrix least-squares calculations using the SHELX97 program package [132]. Details of the structural features are given in **Table 3.6**.

Table 3.6: Single crystal data and structure refinements for $Li_3AsW_7O_{25}$.

Empirical formula	$Li_3AsW_7O_{25}$
Formula weight	1782.69
Temperature	293(2) K
Crystal system	Orthorhombic
Space group	*Pbca*
Unit cell dimensions	a = 724.38(3) pm b = 1008.15(4) pm c = 4906.16(17) pm
Volume	$3582.9(2) \times 10^6$ pm^3
Z	8
Density (calculated)	6.610 Mg/m^3
Absorption coefficient	46.720 mm^{-1}
F(000)	6080
θ for data collection	2.49- 32.13°
Indices ranges	$-10 \leq h \leq 10$, $-15 \leq k \leq 15$, $-73 \leq l \leq 73$
Reflections collected/unique	186487/ 6277
Refinement method	Full-matrix least-squares on F^2
GOF on F^2	1.141
R_{int}, R_{sigma}	0.1196, 0.0378
R-values [$I > 2\sigma(I)$]	$R1$ = 0.0552, $wR2$= 0.1330
R-values (all data)	$R1$ = 0.0825, $wR2$= 0.1433
Largest diff. peak and hole	5.692 and -5.297 e/A^3
CSD number	429249[a]

$R1 = \sum(|F_o| - |F_c|)/\sum|F_o|$; $wR2 = \{\sum[w(|F_o|^2 - |F_c|^2)^2]/\sum[w(|F_o|^2)^2]\}^{1/2}$

[a]Further details can be obtained from Fachinformationszentrum Karlsruhe (Germany) referring to the respective CSD number

X-ray powder diffraction measurements were carried out at ambient condition in the range between 3° and 110° 2θ with a step size of 0.0167° and a data collection time 30 s/step. The fundamental parameter approach, where the fundamental parameters were fitted against a LaB_6 standard material, was applied for the Rietveld refinement using "Diffrac^{Plus} Topas 4.2" software (Bruker AXS GmbH, Karlsruhe, Germany). For this purpose, the starting atomic coordinates were taken from the results of the single crystal structure refinement.

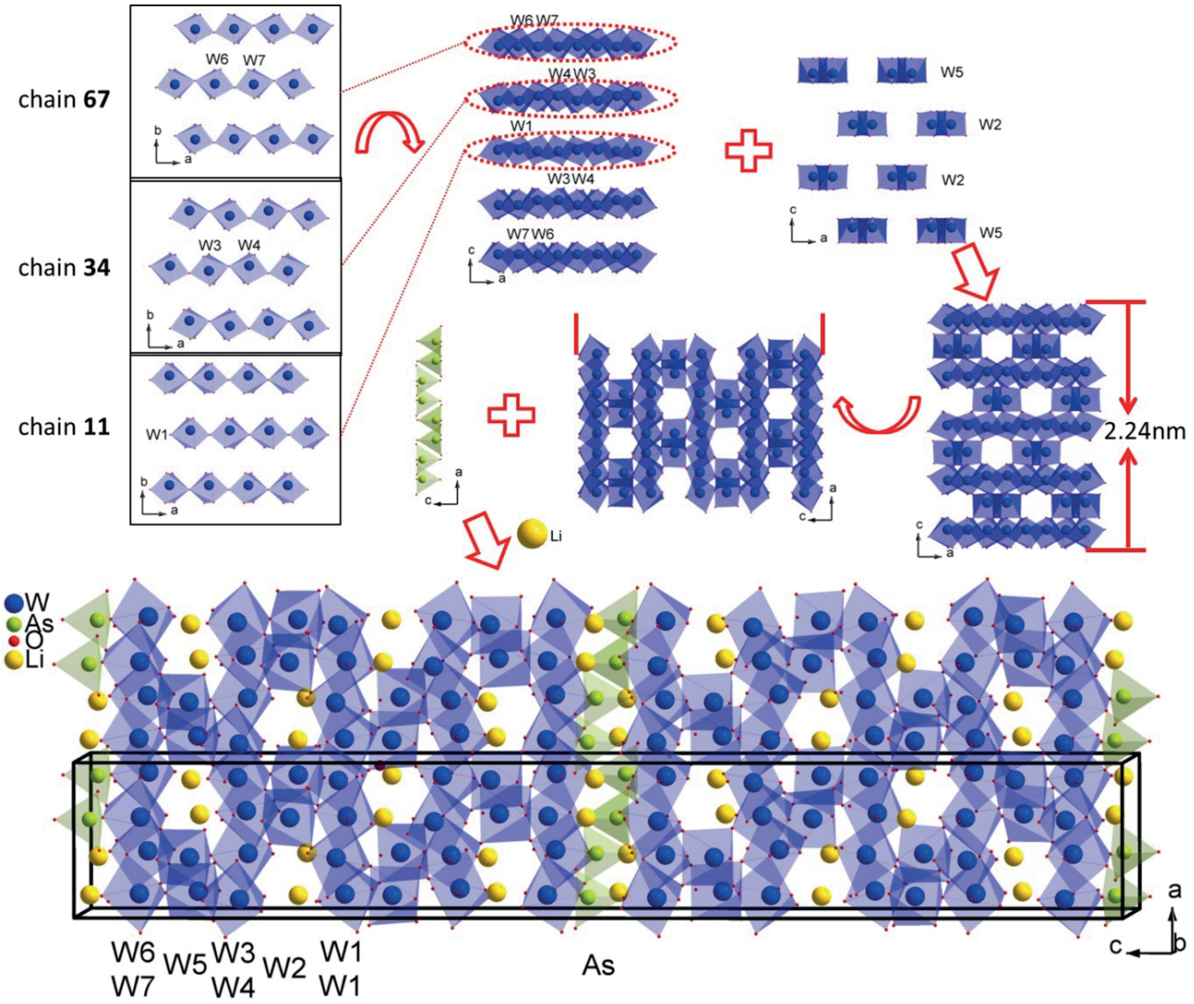

Figure 3.7: Crystal structure of $Li_3AsW_7O_{25}$ showing different schematic components

Time-of-flight (TOF) neutron powder diffraction was performed on approx. 6.5 g of a sample loaded in a vanadium container of 8 mm diameter. The measurements were conducted at room-temperature and flight-times between 9.0 and 103.7 ms corresponding to d-spacing from 0.040 to 0.460 nm and flight-times from 38.4 to 281.9 ms corresponding to d = 0.170-1.247 nm using center wavelengths of 0.1066 nm and of 0.3731 nm for 2 and 1 h, respectively. Rietveld refinements against both powder data sets were performed using the GSAS [137] platform with EXPGUI interface [138]. During these Rietveld refinements the scale factor, absorption coefficient and two profile shape parameters were varied for each pattern. Lattice parameters, fractional coordinates of the atoms and their displacement parameters were optimized against both data sets simultaneously.

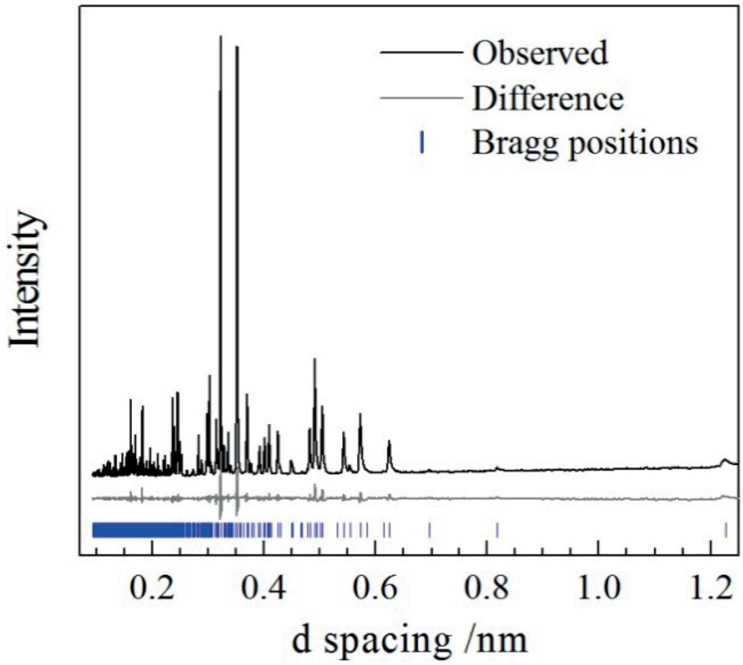

Figure 3.8: X-ray powder data Rietveld plot of $Li_3AsW_7O_{25}$.

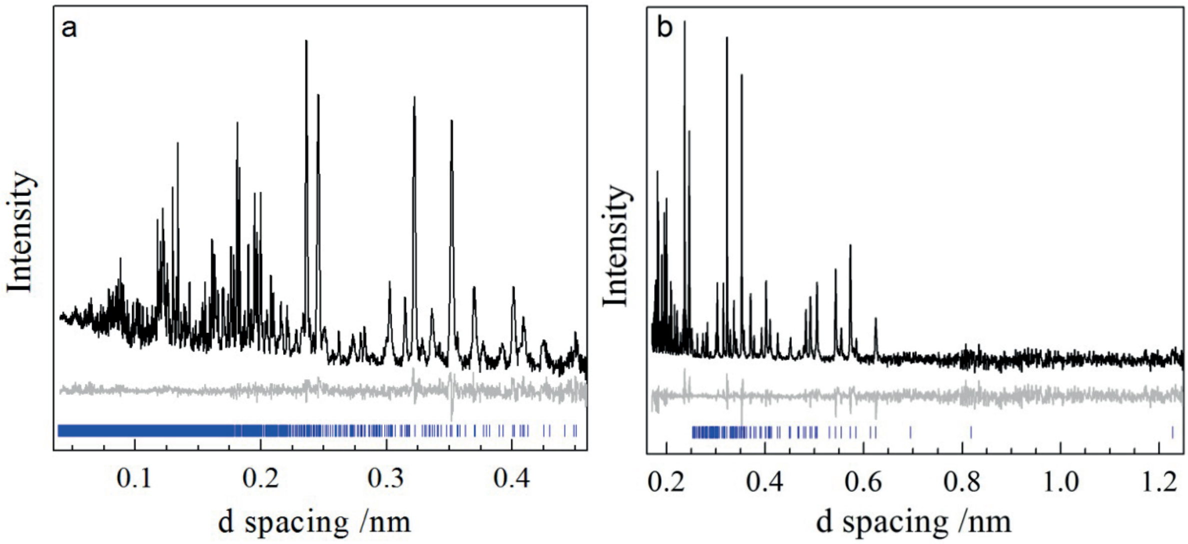

Figure 3.9: Neutron powder time-of-flight data Rietveld plots of $Li_3AsW_7O_{25}$ for the center wavelengths of 0.1066 nm (a) and 0.3731 nm (b).

The crystal structure of $Li_3AsW_7O_{25}$ is shown in **Figure 3.7** together with some schematic components. The compound crystallizes in the centrosymmetric orthorhombic space group *Pbca*. The details of the single crystal structural features are given in **Table 3.6**. The Rietveld refinement results obtained from X-ray and neutron powder diffraction data agree well with those obtained from the single crystal data analysis; **Figure 3.8** and **Figure 3.9** depict the corresponding Rietveld plots, respectively, and **Table 3.7** summarizes the refined lattice parameters.

Table 3.7: X-ray and neutron powder diffraction data Rietveld refinement results for $Li_3AsW_7O_{25}$.

	X-ray	Neutron
Crystal system	Orthorhombic	Orthorhombic
Space group	*Pbca*	*Pbca*
Unit cell dimensions	a = 724.70(1) pm	a = 724.69(1) pm
	b = 1008.82(1) pm	b = 1009.10(1) pm
	c = 4909.42(3) pm	c = 4910.33(4) pm
Volume	3589.27(4) × 10^6 pm^3	3590.82(3) × 10^6 pm^3
CSD number[a]	429248[a]	429250[a]

[a] Further details can be obtained from Fachinformationszentrum Karlsruhe (Germany) referring to the respective CSD number

The asymmetric unit contains 36 crystallographically independent atoms. All tungsten atoms are 6-coordinated and arsenic atoms are 4-coordinated forming WO_6 octahedra and AsO_4 tetrahedra, respectively. The W–O bond lengths are in the range between 170(1) pm and 222(1) pm. The As–O bond lengths vary from 166(1) pm to 170(1) pm. The W1 octahedra share two opposite corners to each other forming a 1-D zigzag chain along the **a**-direction (**Figure 3.7**, chain-**11**) with W1–W1–W1 angles of 176.3(1)° in the ac-plane. These chains are arranged in the –ABAB– stacking sequence along the **b**-direction. Alike, chain-**34** (formed by W3 and W4) and chain-**67** (formed by W6 and W7) are in the same construction way (i.e., –ABAB– stacking sequence along the b-direction) and located on both sides of the chain-**11**. The angles W3–W4–W3 and W6–W7–W6 are 159.51(3)° and 177.7(1)°, respectively. Chain-**11**, chain-**34** and chain-**67** are further connected by isolated W2 and W5 octahedra forming approximately a 2.24 nm-sized oxo-tungsten block along the **c**-direction (**Figure 3.7**). These blocks are connected through chain-**67** to the isolated AsO_4 tetrahedra to form the 3-D framework. The linkage of the chains and polyhedra can be clearly seen from the resulting channels. **Figure 3.10** shows three different types of channels in the framework along the **a**-direction.

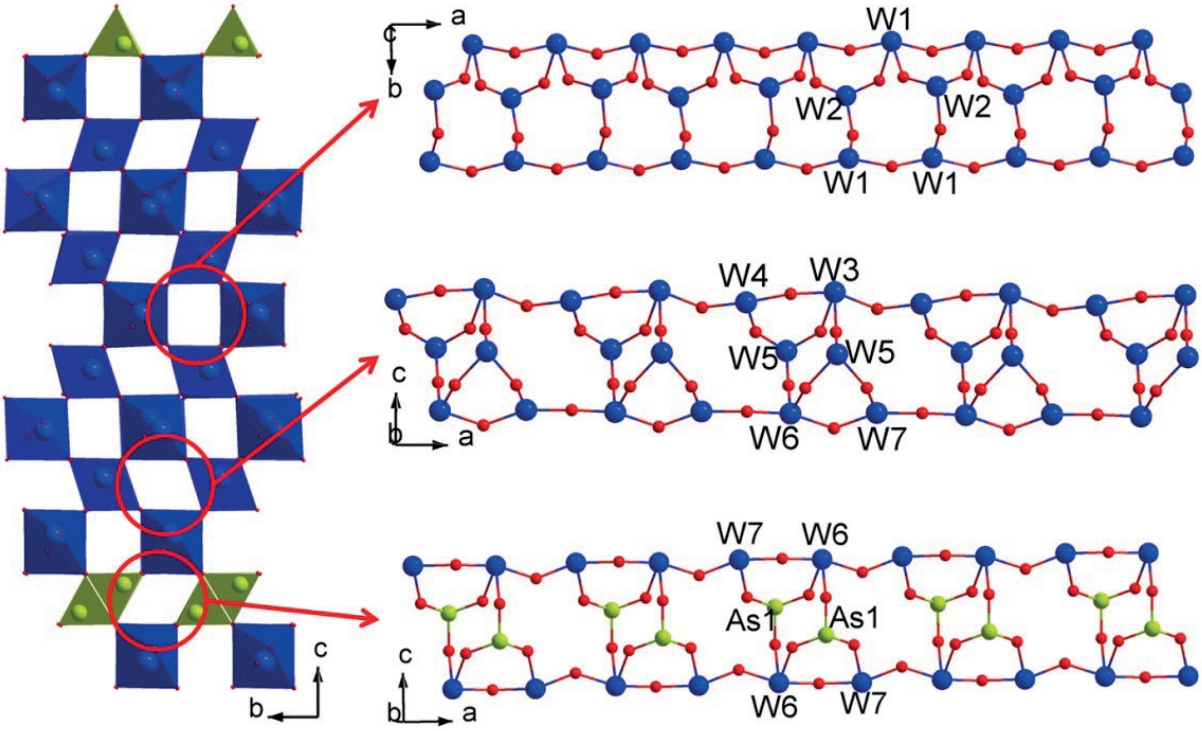

Figure 3.10: Three types of channels in the framework of $Li_3AsW_7O_{25}$.

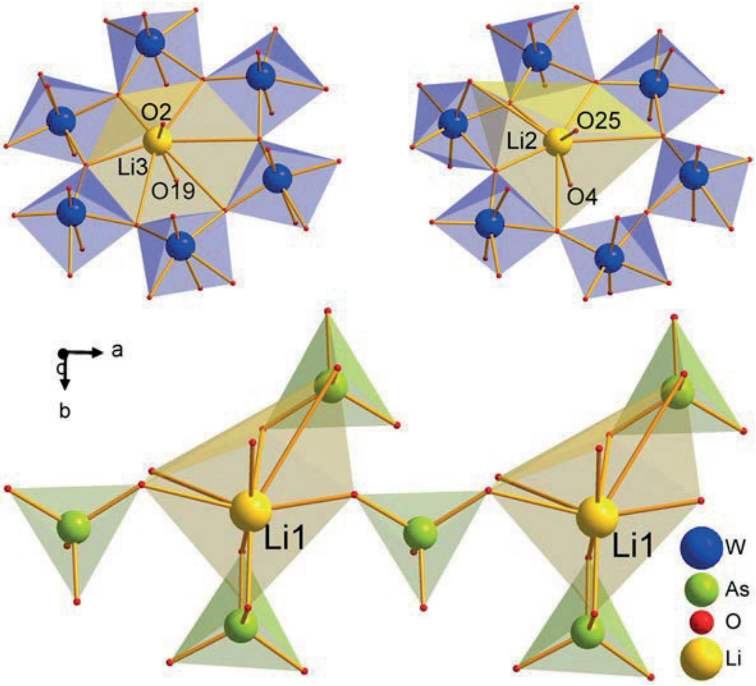

Figure 3.11: Coordination environments of the Li1, Li2 and Li3 in $Li_3AsW_7O_{25}$.

Li3 locates at the centroid of the hexagonal plane of a hexagonal bipyramid with distances of about 203(3) pm and 188(3) pm for Li3–O2 and Li3–O19, respectively. Due to these short Li–O distances the associated O2 and O19 may not show the characteristic features of W=O terminal bonds forming short distances of 170(1) pm (W4–O2) and 171(1) pm (W7–O19), respectively. Alike, Li2 also locates at the centroid of a hexagonal bipyramid with two short distances of 186(4) pm (Li2–O4) and 210(3) pm (Li2–O25). Li1 and As1 atoms arrange in an alternate order along the **a**-direction with an As–Li–As angle of 167(1)°. The coordination of these lithium atoms are shown in **Figure 3.11** with the Li–O distances in the range between 186(4) pm and 349(4) pm.

Distortion indices and bond valence sums (BVS's) of the polyhedra framework are shown in **Table 3.8**. Due to the SOJT susceptibility of W^{6+} cation, WO_6 octahedra can hold a certain degree of distortions leading to frequent occurrences of corner-, edge- or face-sharing clusters, chains, layers or 3-D frameworks.

Table 3.8: Distortion indices and bond valence sum (BVS) of the polyhedra in $Li_3AsW_7O_{25}$.

Polyhedra	^{a}BAV /deg.^{2}	^{b}MQE	BVS /v.u.
$W1O_6$	76.4(1)	1.03(1)	6.37(10)
$W2O_6$	72.6(1)	1.03(1)	6.23(8)
$W3O_6$	78.3(1)	1.03(3)	6.34(8)
$W4O_6$	77.6(1)	1.03(1)	6.36(9)
$W5O_6$	64.6(2)	1.03(4)	6.31(8)
$W6O_6$	49.3(1)	1.02(1)	6.35(8)
$W7O_6$	74.0(1)	1.03(1)	6.39(9)
$As1O_4$	33.7(1)	1.01(1)	5.03(6)
$Li1O_8$	-	-	1.03(5)
$Li2O_8$	-	-	0.96(4)
$Li3O_8$	-	-	0.95(4)

[a] Bond angle variance (BAV)

[b] Mean quadratic elongation (MQE) of the WO_6 octahedra and AsO_4 tetrahedra

There are also oxo-tungstate structures with one long cell parameter as in $Cs_{0.06}WO_3$ [139] with orthorhombic cell parameters of $a = 3485(5)$ pm, $b = 733(1)$ pm and $c = 387.9(9)$ pm, which is an (1,7) ITB-type. In this structure, all octahedra are corner-shared with each other. Octahedra connected via oxygen atoms to form layers in the *bc*-plane can be named as part-1, seven of such layers corner share along the a-direction to form part-7. These two parts are connected by chains along the c-direction. Comparing the construction of $Li_3AsW_7O_{25}$ with that of ITB-type bronze, the 2 nm bocks can be considered as part-7, and the arsenic tetrahedra as part-1. Octahedra corner-sharing via oxygen atoms to form chains or layers and arranging perpendicular to each other in the *–ABAB–* stacking sequence is a common building methods, which is also the construction way for part of $Cs_{0.06}WO_3$. A similar part of structural building unit as of $Li_3AsW_7O_{25}$ can be found in the structure of $ANb_4WO_9(PO_4)_3$ (A = K, Rb, Cs) [140], where the octahedra corner shared to double layers with PO_4 located in the channel and individual octahedra connect them via sharing the oxygen atoms. However, in the $Li_3AsW_7O_{25}$ structure, all the chains are connected by individual octahedra forming a one dimensional limited range block and then via AsO_4 tetrahedra building unit further connected together, which is a completely novel construction way in the tungsten compounds.

3.3.3. Spectroscopy

The Fourier transform infrared (FTIR) absorption spectra were measured both for the far-infrared (FIR, 30 – 950 cm^{-1}) and the mid-infrared (MIR, 370 – 4000 cm^{-1}) region. The MIR spectrum was collected using the standard KBr method (1 mg sample in 200 mg KBr), obtained from 32 scans with a spectral resolution of approx. 2 cm^{-1}. For the FIR spectrum recording, a polyethylene pellet (2 mg sample in 50 mg PE) was used, obtained from 16 scans. To get a continuous whole range spectrum, the FIR spectrum was adjusted to the MIR.

Raman spectra were collected using a pressed powder pellet of 5 mm diameter. The spectrum was collected between 50 cm^{-1} and 1200 cm^{-1} with a spectral resolution of approx. 3.2 cm^{-1} using a grating of 1800 grooves/mm. Both the FTIR and Raman spectra were baseline corrected for peak fitting using the LabSpec Version 5 software package. Component analysis was carried out using pseudo-Voigt functions.

There are 432 Raman active ($108A_g + 108B_{1g} + 108B_{2g} + 108B_{3g}$) and 321 IR active ($108B_{1u} + 108B_{2u} + 108B_{3u}$ – acoustic ($B_{1u} + B_{2u} + B_{3u}$)) modes calculated by factor group analysis.

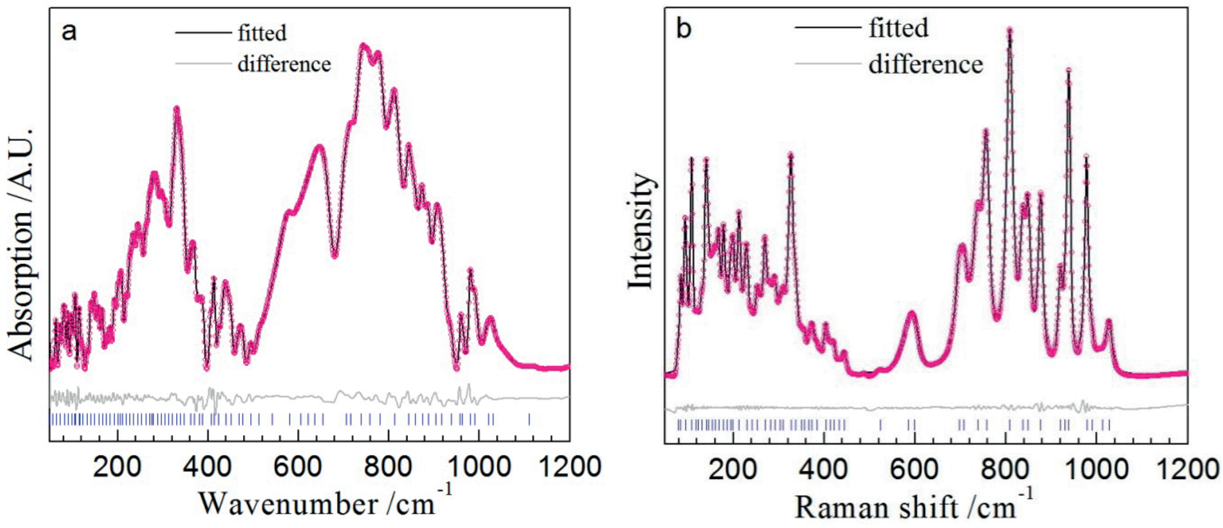

Figure 3.12: Infrared (a) and Raman (b) spectra of $Li_3AsW_7O_{25}$ together with the positions (band maxima) of the fitted modes (vertical ticks) and the difference between the observed and the calculated intensities

Table 3.9: Fitted infrared and Raman mode maxima /cm^{-1}. Standard deviations are estimated as (+0.2) cm^{-1} both for IR and Raman modes.

Infrared	Raman	Assignment	Infrared	Raman	Assignment
49.1			380.7		
56.7				383.3	
63.9			388.0		
73.0				403.7	
	79.1		406.0		
81.8			413.2	412.9	
	84.7			421.0	
90.5				432.5	
	94.6		438.8		W–O–W bending vibrations
98.4				444.7	
104.9			450.3		
107.4	108.9		469.1		υ_4 bending of AsO_4
114.6			476.1		
117.5	118.4		494.0		
122.6	123.0		513.3		
132.8	131.1			523.3	
140.9	140.6		541.6		
	146.0		580.3		
148.8				584.8	
	153.1			598.2	vibration of W=O
157.8			604.3		
	160.2		621.2		W–O–W bending vibrations
166.2	167.6		636.0		
175.4			654.3		
	178.8			696.4	

183.4			704.8		
	185.9			708.1	
193.0	193.7		716.4		
200.8	199.8		737.7	737.5	W–O–W bending vibrations
205.9			758.1	757.2	
209.9			780.0		υ_1 stretching of AsO_4
	212.8			808.7	
218.3			813.0		
226.6				837.1	
	229.2			808.7	
234.8			813.0		
	240.9			837.1	
244.6			844.1		υ_3 stretching of AsO_4
252.9	253.2			849.1	
261.8			858.2		
269.9	270.0		873.9		υ_3 stretching of AsO_4
275.6				876.6	vibration of AsO_4
279.4			886.6		
	281.4		902.5		
288.1			916.5		
	291.3			920.2	
297.0				930.2	
	302.6		936.7		
305.1				938.4	
	309.7		958.2		
312.2			962.3		
320.7				977.7	vibration of WO_6
	326.7		979.6		
330.4			989.0		vibration of W=O
338.9	337.8			990.1	
345.9		υ_2 bending of AsO_4		1012.8	
	349.4		1023.4		
	356.2			1027.6	
361.0			1030.4		
	366.0		1113.7		
370.3			1030.4		
	373.4		1113.7		

However, the observed Raman and IR spectra require only 55 and 81 bands, respectively, between 50 cm^{-1} and 1200 cm^{-1}. The infrared and Raman spectra along with the fitted components are presented in **Figure 3.12**, and the band maxima are given in **Table 3.9**. The bands in the IR spectrum at 844 cm^{-1}–874 cm^{-1}, 780 cm^{-1}, 469 cm^{-1} and 346 cm^{-1} can be attributed to the stretching and bending vibrations of the AsO_4 group. The band at 989 cm^{-1} can be assigned to the short W−O stretching, and those at 439 cm^{-1}, 621 cm^{-1} and 738 cm^{-1} can be associated with the W–O–W bending vibrations. The intense and sharp peak at 978

cm^{-1} can be attributed to the asymmetric W–O vibrations of WO_6 groups, and at around 877 cm^{-1} to the asymmetric As–O vibrations of AsO_4 groups.

Energy dispersive X-ray spectroscopy (EDX) data show the atom ratio of As : W was found to be 1 : 6.6(6) which corresponds within the error to the initial chemical composition and is in agreement with the refined structure. **Figure 3.13** depicts a representative scanning electron microscope image of the investigated sample, which was taken using the secondary electron detector.

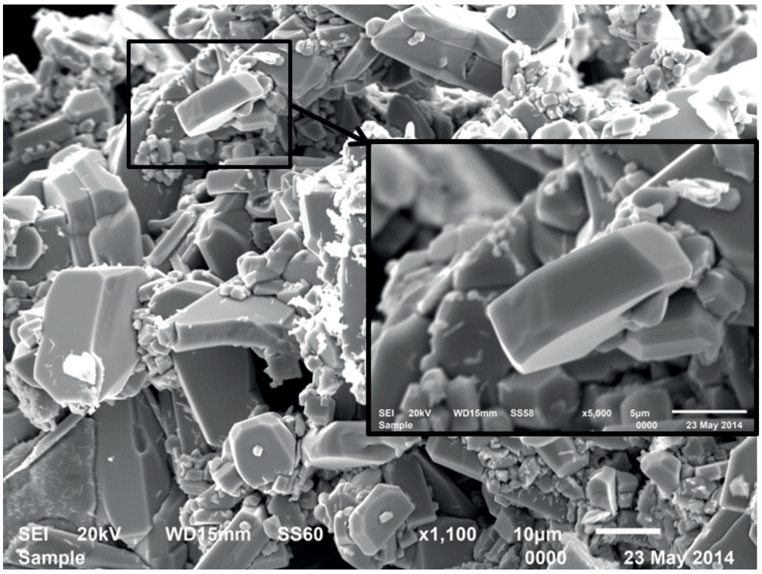

Figure 3.13: Scanning electron microscope image of $Li_3AsW_7O_{25}$.

Ultraviolet-visible (UV-vis) diffuse reflection spectrum was measured over the wavelength range of 200−1400 nm in 2 nm steps. The sample holder was filled with barium sulfate as the background.

The absorption spectrum of the $Li_3AsW_7O_{25}$ sample is shown in **Figure 3.14**a. The extrapolation of the linear part of the absorption curve results in an estimated band-gap energy value of $E_g = 2.8$ eV, determined without considering a direct or indirect electron transition of the electrons [141]. A more detailed analysis of the band-gap energy is realized using the well-known Kubelka-Munk relation [142-143]: $F(R_\infty) = (1 - R_\infty)^2/2R_\infty$, where R_∞ is the reflectance as $R_\infty = R_{sample}/R_{standard}$. In the parabolic band structure, E_g and the extinction coefficient of the material (α) are related through the equation: $\alpha(h\nu) \approx B(h\nu - E_g)^n$, where $h\nu$ is the photon energy, B is an absorption constant and n depends on the electron transition within the semiconductor, with n = 2 for indirect and n = 1/2 for direct transition [141]. If the material scatters in a perfectly diffuse manner [142], the indirect band-gap energy can be obtained by plotting $[F(R_\infty)h\nu]^{1/2}$ against $h\nu$ and the direct band-gap by plotting $[F(R_\infty)h\nu]^2$ against $h\nu$ [141].

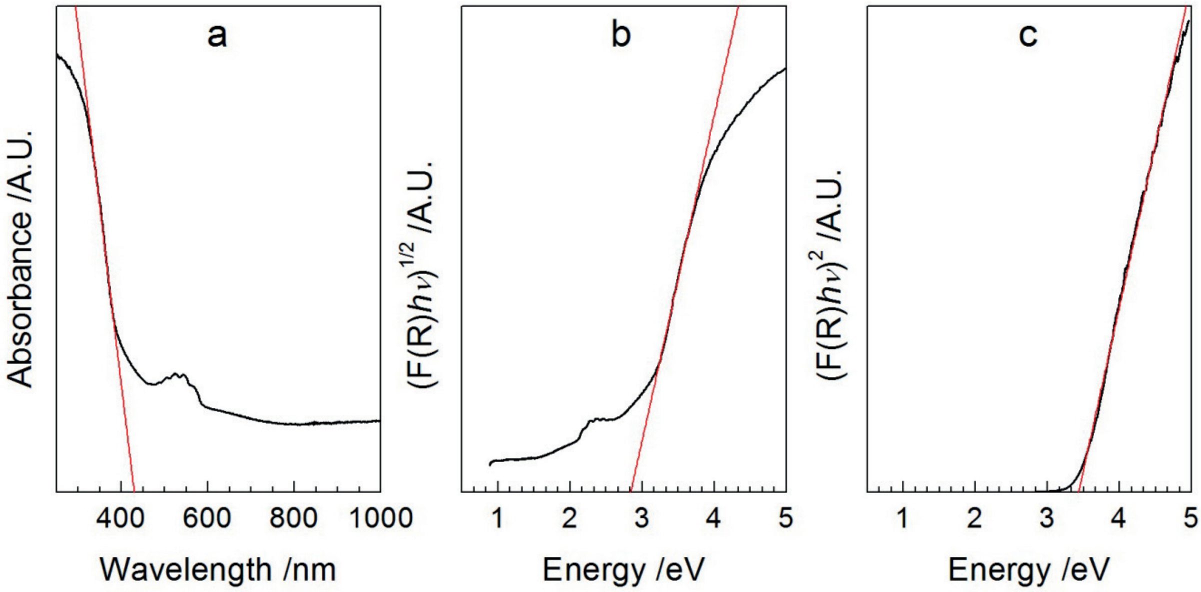

Figure 3.14: The absorption spectrum of $Li_3AsW_7O_{25}$ (a) together with the Kubelka-Munk transformed reflectance for indirect (b) and direct (c) transition.

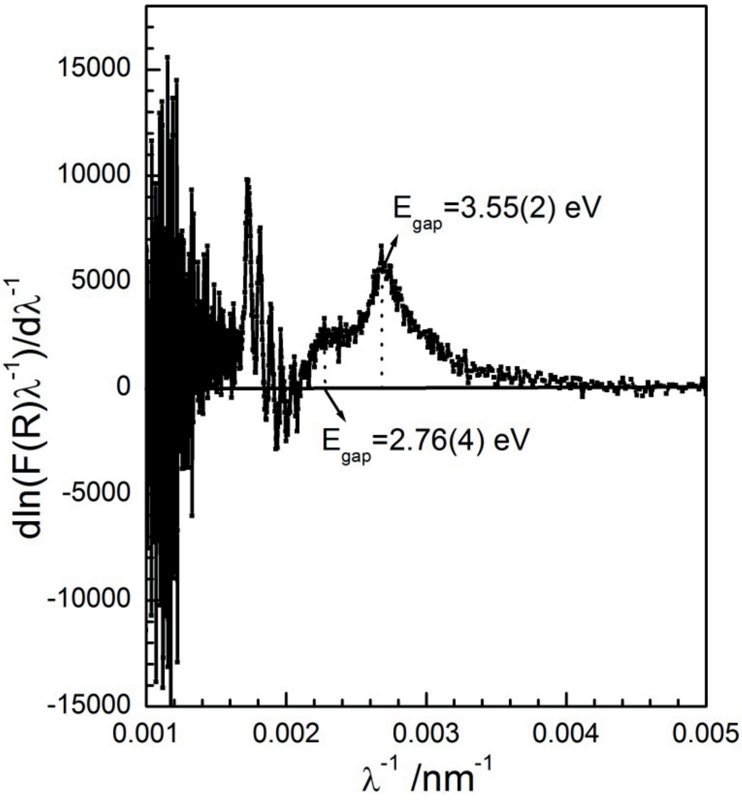

Figure 3.15: The new method DASF (derivation of absorption spectrum fitting) plot with calculated band gaps.

For $Li_3AsW_7O_{25}$ the band-gap energy for an indirect transition (**Figure 3.14**b) has been extracted as 2.84 ±0.03 eV, whereas the direct transition results in 3.40 ±0.04 eV (**Figure 3.14**c). The determined band-gap energies are in both cases within the class of wide-gap semiconductor [144]. The Kubelka-Munk extrapolation suggests a direct band-gap based on the wide range of the linear regression. A new method for determination of band-gap named DASF (derivation of absorption spectrum fitting) [145] shows existing of both the indirect and direct transition type (**Figure 3.15**). To further validate the type of transition respective density functional theory (DFT) calculations are required.

3.3.4. Thermal analysis

Simultaneous thermal analyses (TG-DSC) were carried out using 23.6(1) mg sample which was measured relative to an empty corundum crucible as the reference. A drift correction to the data was applied using an empty corundum crucible measurement.

The DSC curve shows one sharp and one broad peak as shown in **Figure 3.16**. The sharp endothermic signal is almost a straight line in the low-temperature range, which indicates the fusion process of $Li_3AsW_7O_{25}$. The melting point corresponds to the onset temperature of 1135(3) K. The X-ray powder data analysis of the residual shows the existence of WO_3 and unknown phases. The broad endothermic peak can be attributed to decomposition and the release of oxygen. The TG curve shows the decomposition starting at around 1182(5) K.

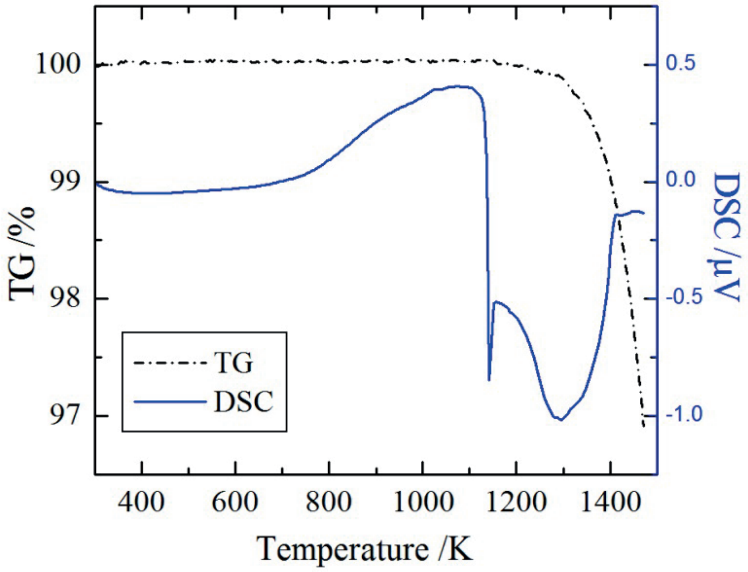

Figure 3.16: Thermogravimetry (TG) analysis and the differential scanning calorimetry (DSC) curve of $Li_3AsW_7O_{25}$.

3.4. Summary and Conclusion

A new alkali metal oxo-tungstate-arsenate $Na[AsW_2O_9]$ was prepared guided by a phenomenological model for the preparation of non-centrosymmetric crystalline materials. The observed mean W−O and As−O bond distances lie within the range of the M−O maps designed for the formation of non-centrosymmetric tungstates and arsenates. A comparative study between $Na[AsW_2O_9]$ and $K[AsW_2O_9]$ shows that the Na−O bond length is significantly smaller than that of K−O. Although WO_6 and AsO_4 polyhedra in $Na[AsW_2O_9]$ possess slightly higher distortions the associated asymmetric chemical bonding do not enhance the non-linear optical susceptibility, that is, the intensity of the second harmonic generation of $Na[AsW_2O_9]$ was observed lower than that of $K[AsW_2O_9]$. A trial with Li produced a centrosymmetric compound $Li_3AsW_7O_{25}$. It is thus reasonable to test the other alkaline element such as Rb or Cs substitution at the K-sites as a way to tune the optical nonlinearity level. Detailed analysis of the sources of NLO properties of the crystals from the $A[AsW_2O_9]$ isotypes (A = alkali metals) may be produced by theoretical calculations on the basis of known crystal structures. Moreover, theoretical calculation (e.g., DFT calculation) is further sought for a fuller assignment of the observed IR or Raman frequencies for a deeper understanding of the vibrational properties of the compounds.

Chapter 4 Temperature-dependent behavior of alkali metal arsenotungstates

4.1. Introduction

One great challenge for chemists is to study the mechanism of a specific property with wide application. The property like negative thermal expansion (NTE) is such a case [146]. Thermal expansion, materials expand upon heating, is normal whereas NTE which show in contrast behavior is rare. Materials with NTE are of considerable interest to tune thermal expansion coefficients to be adjustable and useful for electrical, optical and precision devices [147]. However, limitations also became apparent due to the stability or incompatibility under use conditions. NTE can be isotropic or anisotropic which means these materials can shrink in all directions or only show one or two direction contracting. Only cubic or amorphous materials would show real isotropic NTE.

This property is limited to only a few families and among them; the tungstate compounds achieved remarkable development over the last two decades. Two most well-known and intensively studied families are AW_2O_8 ($A = Zr^{4+}$, Hf^{4+}) [148-149] and $A_2W_3O_{12}$ ($A = Sc^{3+}$, Al^{3+}, Y^{3+} etc.) [70-72,150]. The mechanism of this intrinsic property is explained based on structures and till now the most common theories are phonon transverse vibrations, rigid unit modes and phase-transition etc. [151]. In the structure of ZrW_2O_8, all the oxygen atoms of ZrO_6 are shared with WO_4 tetrahedra while WO_4 have one terminal oxygen atom which is important in the phase-transition at approximately 450 K. The structure of $Sc_2W_3O_{12}$ was also composed of ScO_6 octahedra and WO_4 tetrahedra but with all polyhedral corners shared. NTE in both families is related to transverse thermal motion in A–O–W linkages [152].

In the tungstates, $K[AsW_2O_9]$ [116], $Na[AsW_2O_9]$ [130] and $Li_3AsW_7O_{25}$ [131] extend the tungsten-bronze family and they are the first series of ternary compounds containing arsenic. They were synthesized by solid-state reaction. In this chapter, we study their thermal behavior using temperature-dependent X-ray and neutron diffractions, Raman spectroscopy as well as density functional theory (DFT) calculations. The combined approach of low-temperature neutron and high-temperature X-ray diffraction can be used to determine cell parameters and get thermal expansion behavior over a wide temperature range. Analyzing the structure information at variable temperatures – bond lengths, bond angles, atom positions and polyhedra out-of-center distortions etc. – also help clarify the origin of NTE.

4.2. Experimental methods

4.2.1. Temperature-dependent X-ray powder diffraction

The powders were placed on flat corundum sample holders using acetone to submerge and produce small evaporation channels to allow for the thermal expansion during heating. Patterns for $K[AsW_2O_9]$ were taken in the range between 5° and 85° 2θ with a step width of 0.0167° and a collection time of 45 s/step; the temperature range from 303 K to 978 K with a ramping slice of 15 K. Patterns for $Na[AsW_2O_9]$ were taken in the range between 5° and 130° 2θ with a step width of 0.0167° and a collection time of 50 s/step; the temperature range from 300 K to 980 K with a ramping slice of 20 K Patterns for $Li_3AsW_7O_{25}$ were taken in the range between 5° and 130° 2θ with a step width of 0.0167° and a collection time of 50 s/step; the temperature range from 300 K to 1040 K with a ramping slice of 20 K The Rietveld batch refinements were applied using "Diffrac^{Plus} Topas 4.2" software (Bruker AXS GmbH, Karlsruhe, Germany) starting with room-temperature data.

4.2.2. Temperature-dependent powder neutron diffraction

Time-of-flight powder neutron diffraction was performed on approximate 6.5 g of sample which were loaded in a vanadium container. The data were collected in the temperature range from 10 K to 90 K with 5 K/step, 90 K to 300 K with 10 K/step and 380 K-900 K with 10 K/step for $K[AsW_2O_9]$ and with 10 K/step in the same temperature range for the other two compounds. The flight-times were between 9.8 ms and 121.6 ms corresponding to d-spacing from 0.43 nm to 5.38 nm using the center wavelength of 1.333 nm for about 20 minutes. Rietveld refinements against both powder data sets were performed using the GSAS [137] platform with EXPGUI interface [138]. During these Rietveld refinements the scale factor, absorption coefficient and two profile shape parameters were varied for each pattern. The lattice parameters, fractional coordinates of the atoms and their displacement parameters were optimized against both data sets simultaneously.

4.2.3. Temperature-dependent powder Raman spectroscopy

The Raman spectra were recorded using a grating of 1800 grooves/mm in the Raman shift range between 50 cm^{-1} and 1100 cm^{-1}. The samples are pressed into powder pellets. The spectra were obtained in the temperature range from 83 K to 293 K and from 298 K to 978 K with a ramping slice of 10 K using a laser worked at wavelength of 532 nm for $K[AsW_2O_9]$; the temperature range from 78 K to 293 K with 5 K/step using a laser worked at wavelength of 785 nm and from 300 K to 980 K with a ramping slice of 10 K using a laser worked at wavelength of 633 nm for Na[AsW_2O_9]; the temperature range from 78 K to 98 K with 5 K/step, from 98 K to 298 K with 10 K/step and from 300 K to 990 K with a ramping slice of 15 K using a laser worked at wavelength of 633 nm for $Li_3AsW_7O_{25}$.

4.2.4. Electrochemical Impedance spectroscopy

Ionic conductivity for the bulk of sample was measured by an AC impedance technique. Specimens with two electrodes for conductivity measurement were prepared as follows: the powder samples were pressed (3 kN) into a pellet and then sintered at 973 K for 12 h. Then platinum was sputtered onto both sides of the pellet in order to be used as electrodes. Electrochemical impedance spectroscopy (EIS) measurements were carried out over the temperature interval 293.15 K to 353.15 K on heating with 10 K/step under argon atmosphere in the frequency range from 10^{-2} Hz to 10 MHz and amplitude of 10 mV. Then the pellet was moved to another sample holder for higher temperature from 373.15 K to 773.15 K with ramping slice of 100 K under air atmosphere.

4.2.5. Bulk modulus

The constant pressure constrained geometry optimizations were performed at 0, 5, 10, 15, 20 and 25 GPa for K[AsW_2O_9], 0, 2.5, 5, 10, 15, 20 and 25 GPa for Na[AsW_2O_9]. Similar experimental method (density functional theory calculation) can be found elsewhere [153-155].

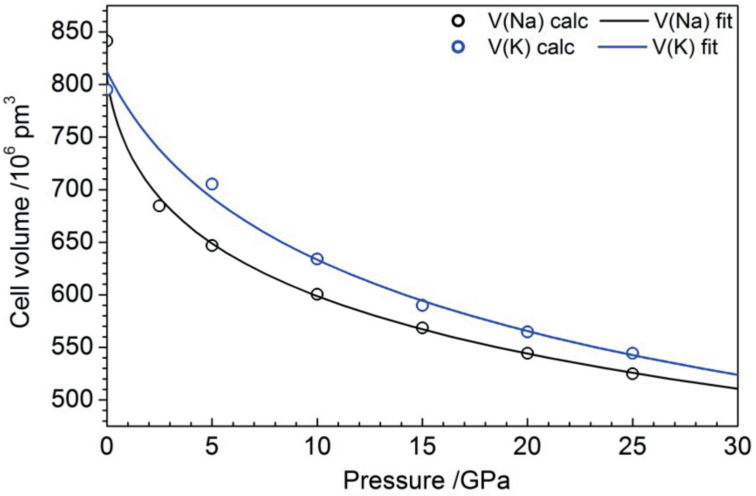

Figure 4.1: Density functional theory (DFT) calculated pressure dependent volume change of Na[AsW_2O_9] and K[AsW_2O_9] along with the 3rd order Birch-Murnaghan EoS fit.

Pressure-volume data were fitted using the 3rd order Birch-Murnaghan equation of state (EoS):

$$P(V) = \frac{3}{2}K_0\left[\left(\frac{V_0}{V}\right)^{7/3} - \left(\frac{V_0}{V}\right)^{5/3}\right]\left\{1 + \frac{3}{4}(K_0' - 4)\left[\left(\frac{V_0}{V}\right)^{2/3} - 1\right]\right\} \tag{4-1}$$

where V_0 and V are the unit cell volume at ambient pressure and unit cell volume at a given temperature. K_0 is the bulk modulus at ambient pressure and K_0' its pressure derivative. **Figure 4.1** shows the pressure dependent DFT calculated unit-cell volume and the respective fits. The fitting simulation converged resulting in K_0 = 19.94 GPa and 6.13 GPa, K_0' = 5.65 and 16.36, V_0 = 812.28 × 10^6 pm^3 and 805.79 × 10^6 pm^3 for $K[AsW_2O_9]$ and $Na[AsW_2O_9]$.

4.3. Results and discussion

4.3.1. Modeling of lattice thermal expansion

The thermal expansion behavior was investigated using composite data collected from low-temperature neutron and high-temperature X-ray diffraction. Low-temperature neutron data required a slight linear adjustment fitting to the high-temperature X-ray diffraction data. The metric parameters were extracted from the Rietveld refinements. The expansion behavior of the cell parameters of $K[AsW_2O_9]$ is highly anisotropic, with negative thermal expansion along the **b-**direction, and positive thermal expansion along **a**- and **c**-direction. In contrast, in $Na[AsW_2O_9]$ and $Li_3AsW_7O_{25}$, all the cell parameters show positive thermal expansion.

There are two well-known approximate theories to calculate the crystal energy: Einstein and Debye model. Einstein [156] assumed that each atom of the solid vibrates about its equilibrium position with an angular frequency ω. Each atom has the same frequency and vibrates independently of other atoms. The total energy of the solid becomes:

$$U_E = \frac{3N\hbar\omega}{e^{\hbar\omega/k_BT} - 1} \tag{4-2}$$

And the Einstein heat capacity is

$$C = 3R\left(\frac{\theta_E}{T}\right)^2 \frac{e^{\theta_E/T}}{(e^{\theta_E/T} - 1)^2} \tag{4-3}$$

N refers to the number of atoms in a mole of solid, $\hbar$ is reduced Planck constant, k_B is Boltzmann constant, and θ_E has been written for $\hbar\omega/k_B$ which is called the Einstein temperature. The Einstein model provides a reasonable qualitative description of the heat capacity of a crystal, but it fails at very low temperature. This is because at low temperature, the energy of the Einstein phonon $\hbar\omega$ significantly above the thermal energy k_BT is barely excited; and the contribution of the acoustic modes whose phonon energies are lower than the thermal energy dominates the thermodynamic functions.

Debye [157] improved on Einstein's theory by assuming that the frequency spectrum was that of an elastic continuum with a high-frequency cut off ω_D determined by the fixed number of vibratory modes. At low temperature, the phonon energy is given as

$$U_D = \frac{3V\hbar}{2\pi^2 c^3}\left(\frac{k_B T}{\hbar}\right)^4 \int_0^\infty x^3\,(e^x - 1)^{-1} dx \tag{4-4}$$

Where V is the volume, c is an average velocity of sound and $x = \hbar\omega/k_BT$. Debye temperature θ_D is defined as $\hbar\omega_D/k_B$. The Debye heat capacity can be written as

$$C = \frac{12\pi^4 N k_B}{5}\left(\frac{T}{\theta_D}\right)^3 \tag{4-5}$$

It shows the characteristic T^3 form from the acoustic modes, in agreement with experimental observation.

We applied a model taking both the Debye and Einstein approximations along with an intrinsic anharmonicity term which becomes increasingly significant at high temperature [158]. In our approach, the thermal expansion of the metric parameters was modeled using Grüneisen first-order approximation for the zero-pressure equation of state while the internal energy were calculated by Debye-Einstein-Anharmonicity (DEA) [153-155],

$$M(T) = M_0 + \frac{\gamma M(T)}{K_0} \tag{4-6}$$

where K_0 and γ are isothermal bulk modulus and thermodynamic Grüneisen parameter, respectively. We take quasi-harmonic Debye (U_D) and Einstein (U_E), and intrinsic anharmonic (U_A) vibrational contributions:

$$M(T) = M_0 + \sum_{i=1}^{d} k_{Di} U_{Di}(T) + \sum_{i=1}^{e} k_{Ei} U_{Ei}\,(T) + k_A U_A(T) \tag{4-7}$$

Where $M(T)$ is the metric parameter at temperature T, k_{Di}, k_{Ei} and k_A are fitting parameters contributing to Debye (U_{Di}), Einstein (U_{Ei}) and anharmonic (U_A) internal energies respectively. In equation 4-7,

$$U_{Di}(T) = 9Nk_BT\left(\frac{T}{\theta_{Di}}\right)^3 \int_0^{\theta_{Di}/T} \frac{x^3}{e^x - 1} dx \tag{4-8}$$

$$U_{Ei}(T) = \frac{3Nk_B\theta_{Ei}}{e^{(\theta_{Ei}/T)} - 1} \tag{4-9}$$

$$U_A(T) = a_A \frac{3Nk_B\theta_A^2}{24T}\left[Te^{(3\theta_A/T)} + 9Te^{(2\theta_A/T)} - 12\theta_A e^{(2\theta_A/T)} - 9Te^{(\theta_A/T)} - 12\theta_A e^{(\theta_A/T)} - T\right]\left(e^{(\theta_A/T)} - 1\right)^{-3} \tag{4-10}$$

N is the atom number in one unit cell, k_B is Boltzmann constant, θ_{Di} and θ_{Ei} are the Debye and Einstein temperatures, and

$$\theta_A = \frac{\sum_{i=1}^{d} k_{Di}\theta_{Di}}{\sum_{i=1}^{d} k_{Di}} \qquad 4\text{-}11$$

The thermal expansion coefficients (TECs) were calculated using equation

$$\alpha(T) = \frac{1}{M_0}\left(\frac{\partial M}{\partial T}\right) \qquad 4\text{-}12$$

The anisotropy parameter (A_{an}) is calculated using the values above,

$$A_{an} = |\alpha(a) - \alpha(b)| + |\alpha(b) - \alpha(c)| + |\alpha(c) - \alpha(a)| \qquad 4\text{-}13$$

In **Figure 4.2**, **Figure 4.3** and **Figure 4.4** the temperature-dependent cell parameters behaviors are depicted with respective model fits as well as thermal expansion coefficients (TECs).

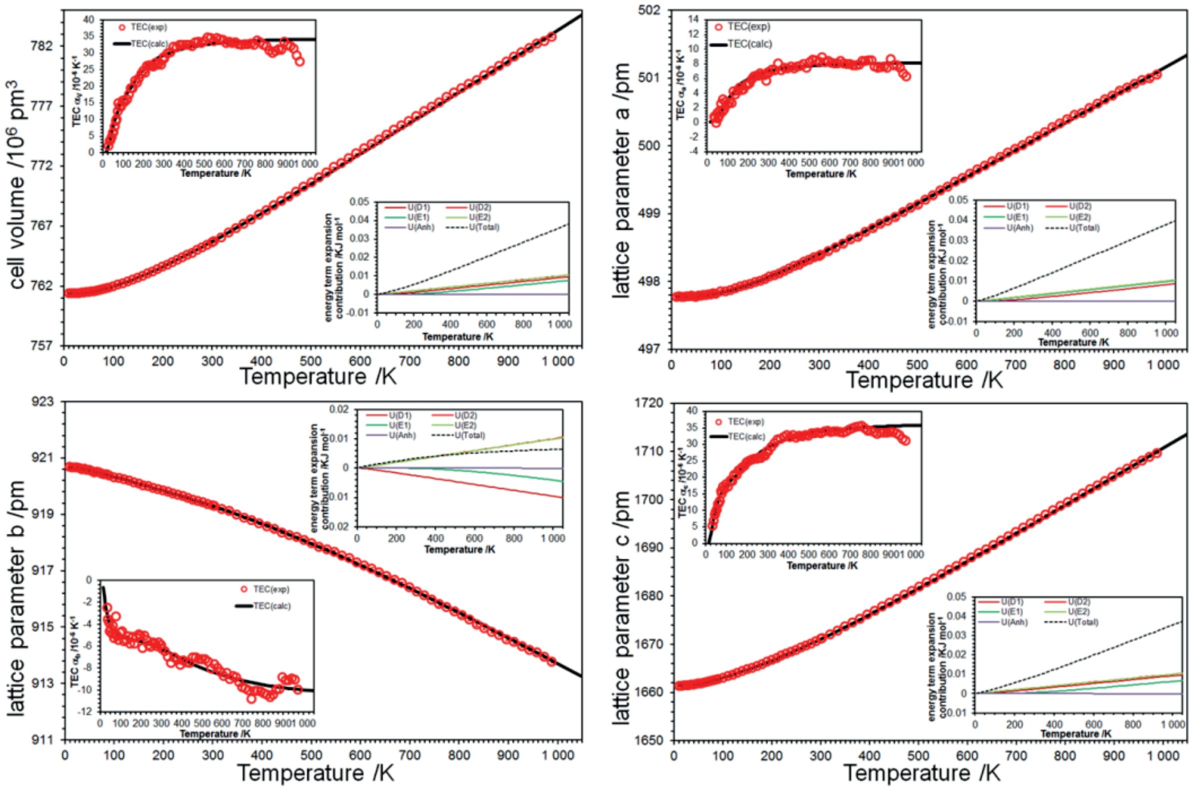

Figure 4.2: Thermal expansion of K[AsW_2O_9] metric parameters together with the DEA model simulations, energy contributions and thermal expansion coefficients.

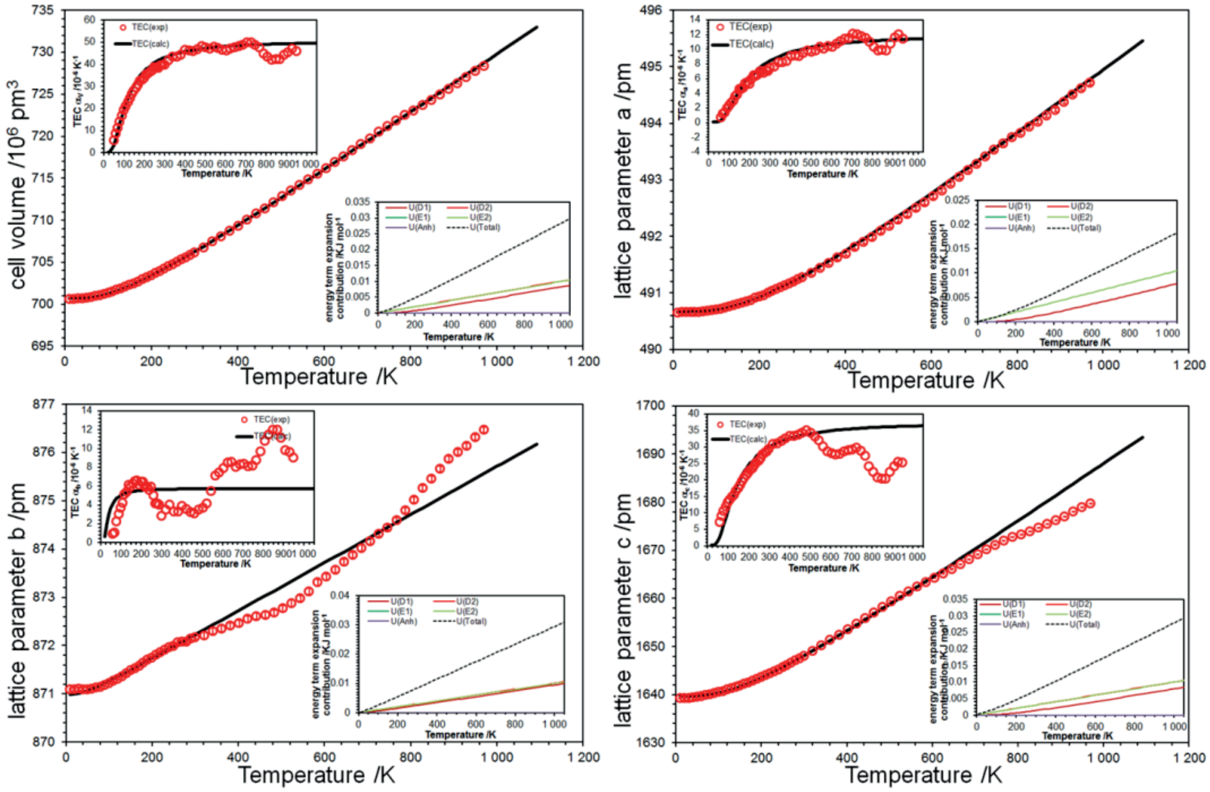

Figure 4.3: Thermal expansion of Na[AsW_2O_9] metric parameters together with the DEA model simulations, energy contributions and thermal expansion coefficients.

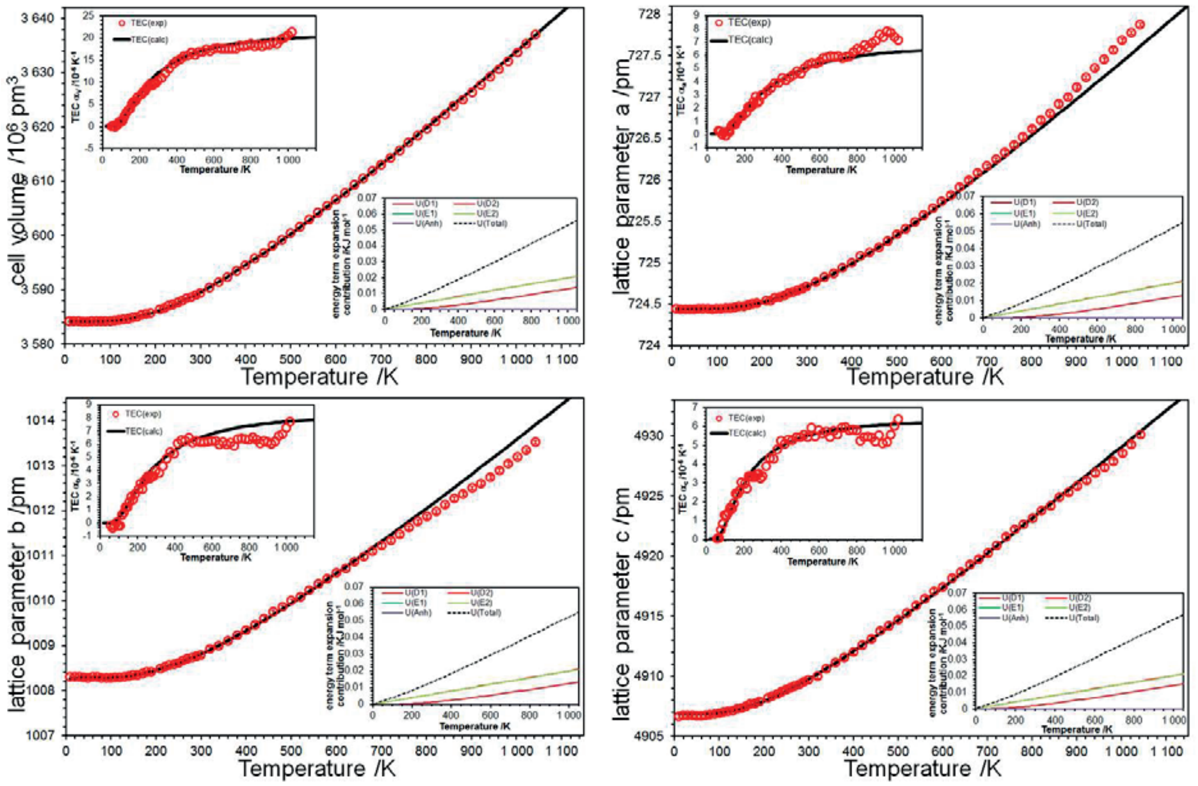

Figure 4.4: Thermal expansion of $Li_3AsW_7O_{25}$ metric parameters together with the DEA model simulations, energy contributions and thermal expansion coefficients.

Table 4.1: Metric parameters from the DEA fitting of the composite data collected from low-temperature neutron and high-temperature X-ray diffraction.

Compounds	Parameter	Volume /10^6 pm^3	a /pm	b /pm	c /pm
K[AsW$_2$O$_9$]	M_0	761.4(1)	497.77(7)	920.6(1)	1661.4(4)
	k_{D1} /× 10^{-12}	7.5(1)	1.88(3)	-2.38(3)	16.9(5)
	θ_{D1}	245(4))	493(7)	113(1)	195(5)
	k_{E1} /× 10^{-12}	4.80(8)	0.02	-2.31(3)	11.3(3)
	θ_{E1}	640(11)	50.0(7)	1600(20)	850(23)
	k_A /× 10^{-12}	0.89(2)	0.30	2.00(3)	0.90(2)
Na[AsW$_2$O$_9$]	M_0	700.7(9)	490.7(2)	870.9(5)	1640(2)
	k_{D1} /× 10^{-12}	16(2)	2.69(9)	2.3(1)	28(4)
	θ_{D1}	468(59)	745(25)	138(8)	568(76)
Li$_3$AsW$_7$O$_{25}$	M_0	3584(1)	724.44(7)	1008.3(2)	4907(1)
	k_{D1} /× 10^{-12}	6.4(2)	0.42	0.71(1)	2.65(6)
	θ_{D1}	1041(30)	1250(12)	1130(19)	848(20)

4.3.2. Spectra and autocorrelations

In the previous chapter, the Raman and IR active modes of the sodium and the lithium compounds were analyzed according to factor group theory but much less bands were observed in the spectra under room-temperature condition. For K[AsW$_2$O$_9$], using density function theory (DFT) calculation, modes with the higher intensity were chosen and attributed to different group vibrations (**Table 4.2**).

Table 4.2: The IR frequencies (ω_i) of K[AsW$_2$O$_9$], and their irreducible representations, intensities calculated by density functional theory (DFT).

Irr. Rep.	Int.	ω_i /cm^{-1}	Assignment
B_3	6250.98	731.3415	W−O + W−O−W
B_2	4805.27	820.4565	As−O−W + As−O
B_1	4563.84	659.6724	W−O−W
B_2	2240.96	704.5982	W−O−W
B_1	2145.49	865.7806	As−O
B_3	1950.01	878.6011	O(As, K, W)
B_2	1500.05	328.4244	As−O
B_2	1249.44	786.1153	As−O−W + As−O
B_2	1023.94	195.9421	O(As, K, W)
B_3	945.28	162.4108	K−O
B_1	881.38	501.6153	O−As−O
B_1	869.16	813.5489	W−O + W−O−W
B_3	829.24	708.4355	W−O−W
B_2	763.60	280.1431	As−O + W−O−W
B_3	658.75	307.7251	As−O

The DFT calculations confirm the published results and give more clarity for this new compound. The spectra can be generally divided into three parts in the higher wavenumber range: bands between 550 cm^{-1} – 850 cm^{-1} mainly are assigned to the W–O bond; 850 cm^{-1} – 910 cm^{-1} can be mainly contributed to the As–O bond and 940 cm^{-1} – 990 cm^{-1} are attributed to W=O terminal bond (**Figure 4.5**). The spectra of Na[AsW_2O_9] are similar to K[AsW_2O_9]. But the DFT calculation for $Li_3AsW_7O_{25}$ is not available because it is much more complicated than the former two compounds.

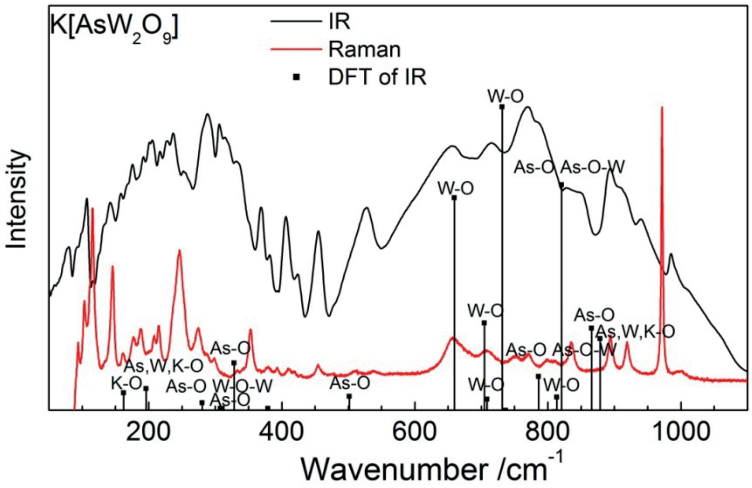

Figure 4.5: IR, Raman spectra and density functional theory (DFT) calculation result of K[AsW_2O_9].

Temperature-dependent Raman spectra with normalized intensity are given in **Figure 4.6**, **Figure 4.7** and **Figure 4.8**. Most of Raman modes show the behavior of peak positions shift towards lower frequency and the width of modes increase with the temperature increment.

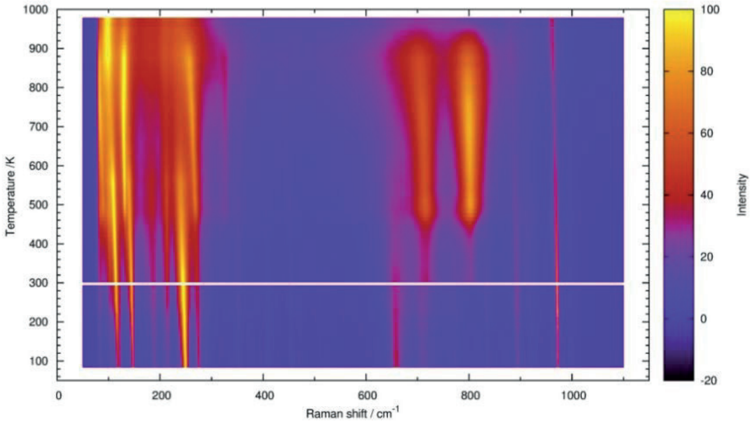

Figure 4.6: The temperature-dependent Raman measurement of K[AsW_2O_9].

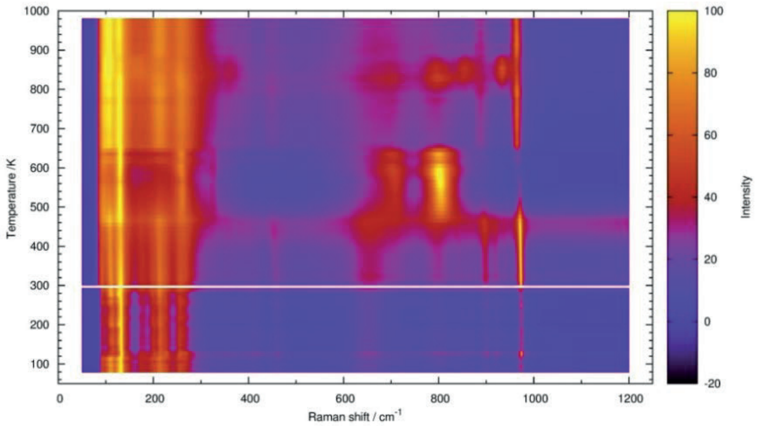

Figure 4.7: The temperature-dependent Raman measurement of Na[AsW_2O_9].

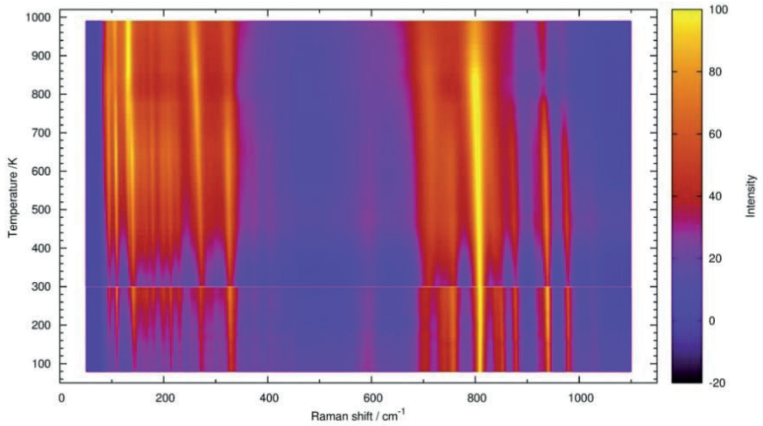

Figure 4.8: The temperature-dependent Raman measurement of $Li_3AsW_7O_{25}$.

However, for the merged peaks with low intensity, it is not easy to split them and analyze the changes. The autocorrelation method can give an easy but sensible way to analyze the mean width. The autocorrelation function, was first used to parameterize the effective line widths of absorption bands in the IR spectra by Salje et al. [159]. It can be written as:

$$Corr(\alpha, \omega') = \int_{-\infty}^{\infty} \alpha(\omega + \omega')\alpha(\omega)d\omega \qquad 4\text{-}14$$

where $\alpha(\omega)$ is the spectrum itself and $\alpha(\omega + \omega')$ is the same spectrum offset in frequency by ω'. Then the Gaussian function was used to fit it.

$$G = k_0 exp\left[-\left(\frac{x - k_1}{k_2}\right)^2\right] \qquad 4\text{-}15$$

The coefficient k_2 is related to the width Γ,

$$\Gamma = \frac{2.354k_2}{\sqrt{2}} \qquad 4\text{-}16$$

Actually, this method is not only limited to IR data. We apply it also in Raman and X-ray diffraction data [160]. Assuming the sum of primary data is one Gaussian function which can be defined with amplitude A and width λ' at the position ω_0 as:

$$G = \frac{A}{\sqrt{2\pi}\lambda'} e^{-\frac{(\omega-\omega_0)^2}{2\lambda'^2}} \tag{4-17}$$

The autocorrelation is given as:

$$Corr(G', G', \omega') = \frac{A^2}{\sqrt{2\pi}\lambda'} e^{-\frac{\omega'^2}{4\lambda'^2}} \tag{4-18}$$

And the normalized function can be written as:

$$Corr(G', G', 0) = \frac{A^2}{\sqrt{2\pi}\lambda'} \tag{4-19}$$

$$Corr_{Norm}(G', G', \omega') = \frac{Corr(G', G', \omega')}{Corr(G', G', 0)} = e^{-\frac{\omega'^2}{4\lambda'^2}} \tag{4-20}$$

Then the width λ' is:

$$\lambda'(\omega') = \sqrt{\frac{\omega'}{-4\ln(Corr_{Norm}(G', G', \omega'))}} \tag{4-21}$$

To choose an appropriate value of ω', the plot $\lambda'(\omega')$ against ω' is needed. Choose its value as small as possible to avoid peak overlay effects and meanwhile need avoid the interference of noise contributions. The ω' value for the three compounds in difference temperature range and Raman shift ranges are listed in **Table 4.3**.

Table 4.3: The chosen ω' value for all three compounds.

Compound	Raman shift ranges /cm^{-1}	Assignment	ω' value	
			Low-temperature	High-temperature
K[AsW$_2$O$_9$]	550-850	W−O	1	7
	850-910	As−O	1	5
	940-990	W=O	1	3
Na[AsW$_2$O$_9$]	550-870	W−O	14	15
	875-910	As−O	12	5
	945-990	W=O	5	2
Li$_3$AsW$_7$O$_{25}$	550-865	W−O	1	5
	865-900	As−O	1	10
	955-1000	W=O	1	5

The autocorrelation results of various ranges after baseline correction for these three compounds are shown with diffraction data. The analyzed results of the anisotropy factors and the spectra autocorrelations are in agreement with each other (**Figure 4.9**).

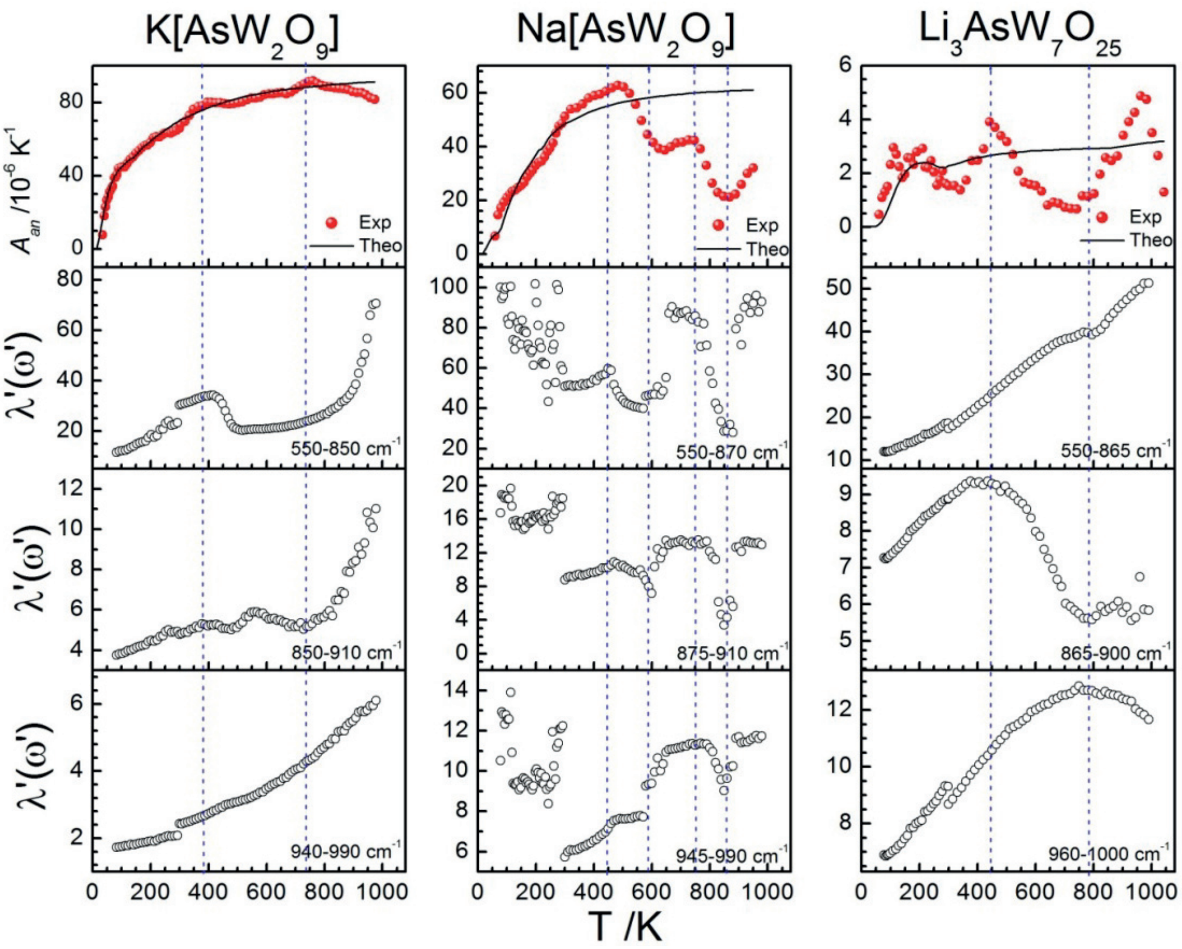

Figure 4.9: The anisotropy A_{an} factor with spectra autocorrelation results of the three compounds.

4.3.3. Electrochemical impedance spectra

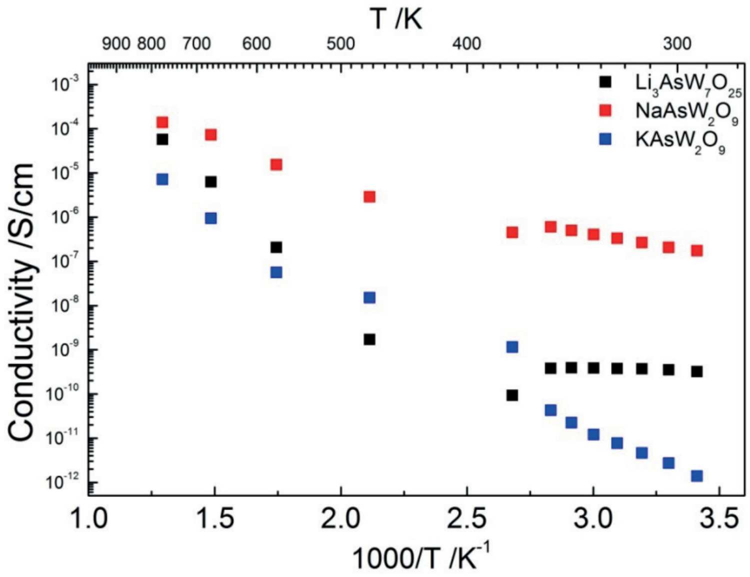

Figure 4.10: The temperature-dependent conductivities of three samples.

Using the Nyquist plot of imaginary impedance against real part at different temperatures, the intercept Z_0 can be obtained on the real axis of the zero phase angle extrapolation. The conductivity (σ) is calculated by the equation:

$$\sigma = \frac{l}{Z_0 A} \qquad \text{4-22}$$

where l is the thickness and A is the area of the pellet. The temperature-dependent conductivities of the three samples are plotted in **Figure 4.10**.

4.3.4. Discussion

The compounds $K[AsW_2O_9]$ and $Na[AsW_2O_9]$ have isostructural framework. However, *b* lattice parameter in the former compounds shows negative thermal expansion while the sodium one shows opposite behavior. There were several explanations for negative thermal expansion. From the view of structure part, individual polyhedra distortions and the interaction of polyhedra including rotation and tilt both affect the metric parameters.

The individual polyhedra can be analyzed using out-of-center distortion factor. Octahedra and tetrahedra out-of-center distortions Δ_d [161] were calculated according to the bond lengths and angles in the polyhedra (**Figure 4.11**) using neutron diffraction data. For octahedra, the magnitude of the distortion ($\Delta_{d\text{-}o}$) was quantified by six W−O bond lengths as well as deviations from 180° of three trans O−W−O bond angles. It can be written as,

$$\Delta_{d\text{-}o} = (|(W{-}O1) - (W{-}O4)| \,/\, |\cos\theta_1|) + (|(W{-}O2) - (W{-}O5)| \,/\, |\cos\theta_2|) + (|(W{-}O3) - (W{-}O3)| \,/\, |\cos\theta_3|) \qquad \text{4-23}$$

where

$\theta_1 = \angle O1{-}W{-}O4$, $\theta_2 = \angle O2{-}W{-}O5$ and $\theta_3 = \angle O3{-}W{-}O6$. In the tetrahedra, the distortion ($\Delta_{d\text{-}t}$) was calculated in a similar way but with only two As−O bond lengths and two trans O−As−O bond angles:

$$\Delta_{d\text{-}t} = (|(As{-}O1) - (As{-}O3)| \,/\, |\cos\theta_1|) + (|(As{-}O2) - (As{-}O4)| \,/\, |\cos\theta_2|) \qquad \text{4-24}$$

and $\theta_1 = 129°28' - \angle O1{-}W{-}O3$, $\theta_2 = 129°28' - \angle O2{-}W{-}O4$.

For W2 and As, the two compounds have similar value of distortion. While the distortion value of the W1 octahedra in $K[AsW_2O_9]$ are much higher than in $Na[AsW_2O_9]$. However, Δ_d keep more or less constant which suggests polyhedra remain stable in the whole temperature range.

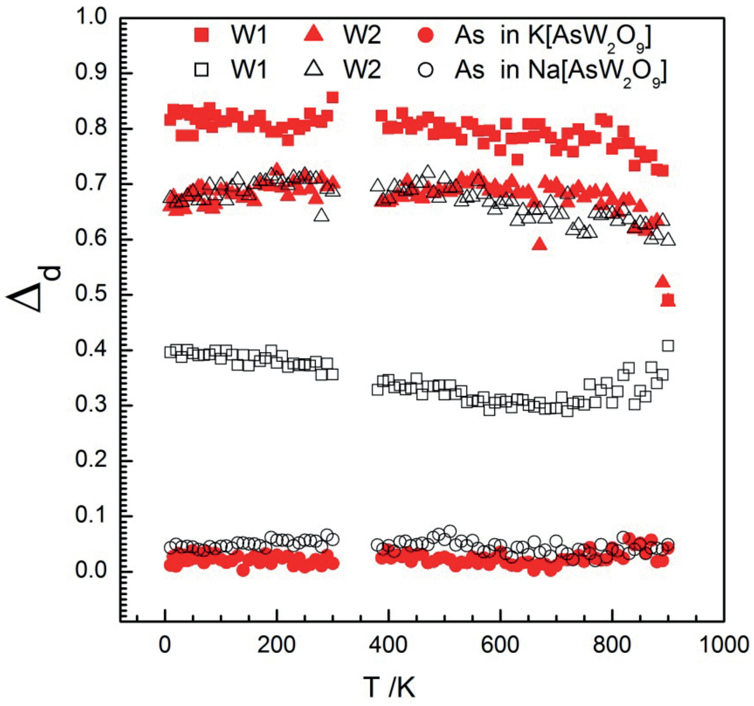

Figure 4.11: Out-of-center distortion results of K/Na[AsW$_2$O$_9$] obtained from neutron diffraction data.

The rotating interaction between polyhedra can be calculated by M–O–M angles (M = W or As). In both cases, most of the bond angles are constant or changed very small degrees except one of W1–O–W2 (**Figure 4.12**). The bond angles of W1–O–W1 and W2–O–As1 in K[AsW$_2$O$_9$] are larger than those in Na[AsW$_2$O$_9$].

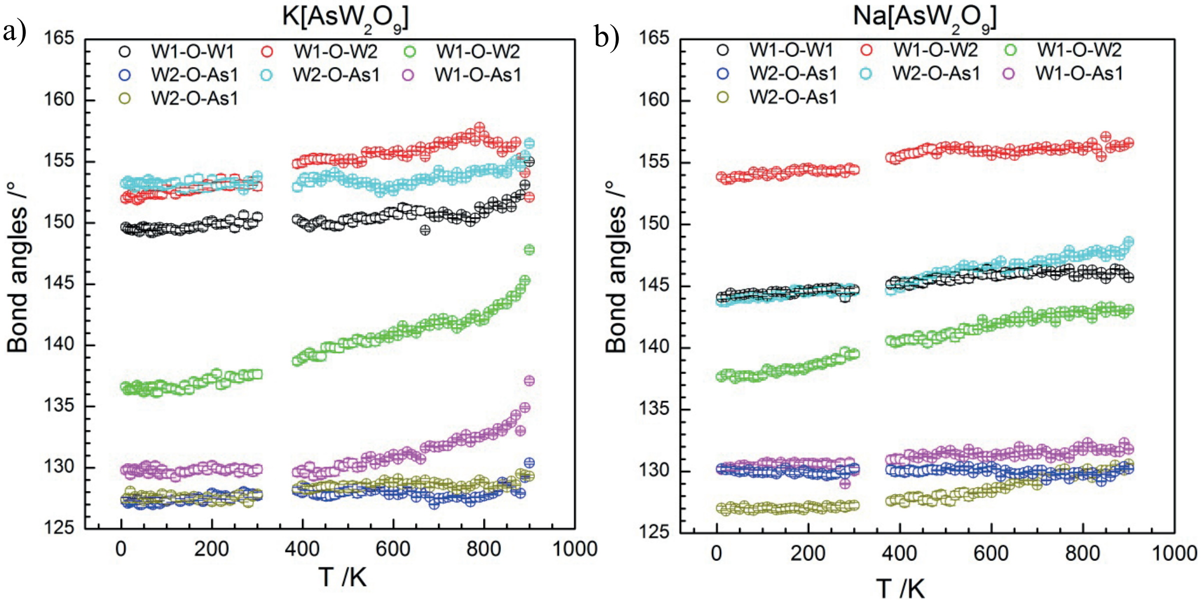

Figure 4.12: The bond angles of M–O–M (M = W or As) in a) K[AsW$_2$O$_9$] and b) Na[AsW$_2$O$_9$].

In the framework of two compounds, the tungsten layers consisting of corner-sharing octahedra can form two types of planes. One plane is approximately parallel to crystal planes (011) and the other plane to crystal planes ($01\bar{1}$) (**Figure 4.13**). The acute angles between two planes obtained from high-temperature neutron diffraction shows that they increase as temperature increase. The angles in potassium compound changed 3.49(1)° from 85.14(1)° at 388 K to 88.63(1)° at 900 K while sodium one changed 1.61(1)° from 75.29(1) to 76.90(1)° in the temperature range between 380 K and 900 K. It is clear the angles in $K[AsW_2O_9]$ and the change are much larger than ones in $Na[AsW_2O_9]$. And this enlargement maybe one reason of smaller *b* lattice parameters at higher temperature in potassium compound.

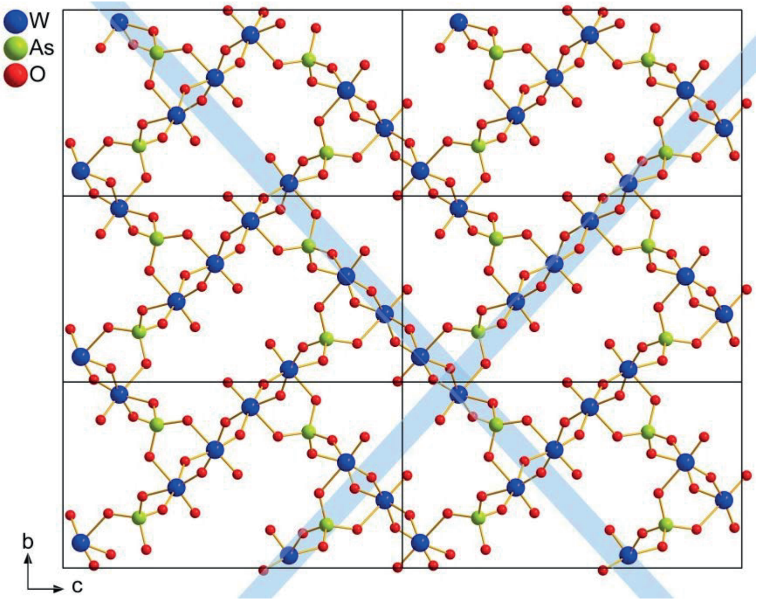

Figure 4.13: Two types of planes in the framework of $K/Na[AsW_2O_9]$.

Chapter 5 The phase diagram of K_2O-As_2O_5-WO_3

5.1. Introduction

$K[AsW_2O_9]$ [116] is the first ternary oxide compound in the system of K_2O-As_2O_5-WO_3. We start to fill the phase diagram under the same synthesis condition but using different molar ratios of raw materials to search for more new materials. The known phases in this system are obtained from former research and used as reference products.

There is only one compound $W_2As_2O_{11}$ [162] existing on the line between As_2O_5 and WO_3. The compound was obtained by heating the mixture of WO_3 and As_2O_5 in the ratio 2 : 1 in sealed, evacuated platinum capsules for about a month at 873 K.

The phase diagram of the system K_2WO_4-WO_3 was given by Gelsing et al. [35]. They prepared the samples by sintering K_2CO_3 and WO_3 in the appropriate ratio at a temperature below the solidus till X-ray patterns did not change on further sintering. Four compounds were presented which are K_2WO_4, $K_2W_2O_7$, $K_2W_3O_{10}$ and $K_2W_4O_{13}$. Sakka [36] confirmed this result and gave the X-ray diffraction data of $K_2W_6O_{19}$. According to his study, the first three samples can be obtained by sintering K_2CO_3 and WO_3 at 873 K for 24 hours. However, $K_2W_4O_{13}$ and $K_2W_6O_{19}$ need to be sintered at a higher temperature of 983K for 10 hour and 100 hours, respectively. Another compound is K_4WO_5 published by Betz and Hoppe [37], the light grey samples were made by $KO_{0.58}$ and WO_3 (2.4 : 1) annealing at 673 K for 5 days, then increasing the temperature to 1123 K in 6 hours, keeping it for 21 days and finally cooling down slowly in 8 days.

The phase diagram of the system K_2O-As_2O_5 [163] shows four compounds: K_3AsO_4, $K_4As_2O_7$, $K_5As_3O_{10}$ and $KAsO_3$. K_3AsO_4 were obtained by mixing KO_2 and As in the ratio of 3 : 1, heating to 973 K at a rate of 350 K/h and cooling to room-temperature via turning off the furnace. $K_5As_3O_{10}$ [164] single crystals were grown from a melt of K_2O and As_2O_5 by cooling from 1073 K at a rate of 0.14 K/min and are very hygroscopic. $KAsO_3$ [165] which is formed on dehydration of KH_2AsO_4, has three forms stable at different ranges of temperatures: the α-form is stable above 803 K, while the β-form is metastable and the γ-form is stable at room-temperature. There are two more compounds K_5AsO_5 and $K_2As_4O_{11}$ shown in the phase diagram of K_2O-As_2O_5-H_2O [166].

According to the information above, the phase diagram of the system K_2O-As_2O_5-WO_3 in molar percentage with all the references can be drawn (**Figure 5.1**).

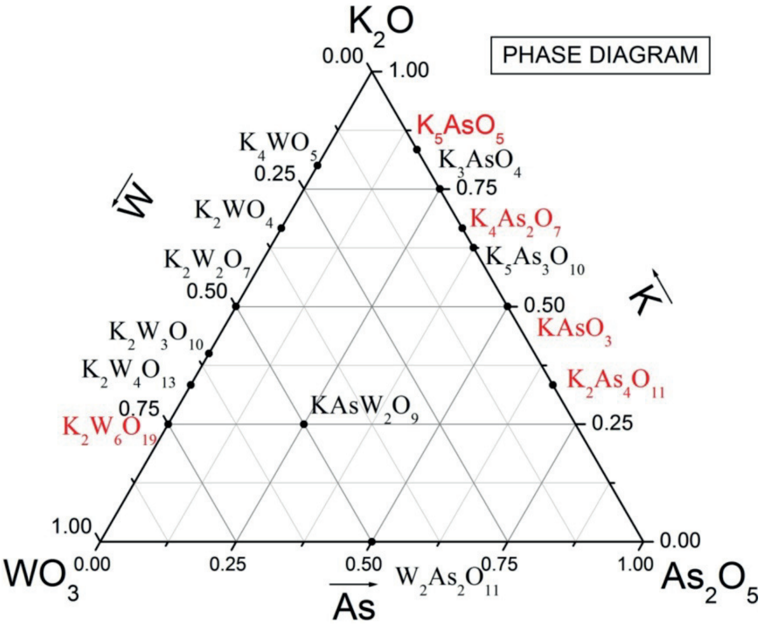

Figure 5.1: Phase diagram of K_2O-As_2O_5-WO_3. For the formula in red color no structural data are available (in the ICSD).

5.2. System of K_2O-As_2O_5-WO_3

5.2.1. Syntheses

Mixtures of KNO_3, $NH_4H_2AsO_4$ and WO_3 in the appropriate molar ratio were grounded intensively, and then heated in a platinum crucible up to 1023 K for 24 hours. Afterwards turned off the furnace and let the samples cool to room-temperature inside the furnace naturally.

5.2.2. Characterization

The powder X-ray diffractions were collected using different programs which are summarized in **Table 5.1** and refined by Rietveld method. The crystallographic information files (cif) of the reference compounds are collected from Inorganic Crystal Structure Database (ICSD). Special points such as located on the connected lines between two compounds were selected in the phase diagram and 17 of them (**Figure 5.2**) helped to complete it. The molar ratios of three raw materials are listed in **Table 5.1**.

Table 5.1: The molar ratio of phase diagram samples and measurement information.

Sample label	Molar ratio of K : As : W	Measurement instrument and program
1	0.25 : 0.125 : 0.625	PW 1800_005_085_003_010s_7h24m
2	0.1794 : 0.0688 : 0.7518	X-pert_003_110_30s_26min
3	0.125 : 0.25 : 0.625	PW 1800_005_085_002_001s_1h06m
4	0.125 : 0.326 : 0.549	X-pert_005_90_30s_21min
5	0.125 : 0.375 : 0.5	X-pert_005_90_30s_21min
6	0.25 : 0.5 : 0.25	PW 1800_005_085_003_010s_7h24m
7	0.29 : 0.46 : 0.25	X-pert_003_120_25s_21min
8	0.37 : 0.47 : 0.16	X-pert_003_110_30s_26min
9	0.29167 : 0.125 : 0.58333	PW 1800_005_085_002_001s_1h06m
10	0.827 : 0.125 : 0.048	X-pert_003_120_25s_21min
11	0.7083 : 0.125 : 0.1667	PW1800_005_085_002_001s_1h06m
12	0.625 : 0.125 : 0.25	X-pert_003_120_25s_21min
13	0.5625 : 0.1875 : 0.25	PW 1800_005_085_003_010s_7h24m
14	0.5 : 0.1 : 0.4	X-pert_003_110_30s_26min
15	0.498 : 0.167 : 0.335	PW 1800_005_085_002_014s_15h35m
16	0.5 : 0.375 : 0.125	X-pert_003_120_25s_21min
17	0.4589 : 0.0965 : 0.4446	X-pert_003_110_30s_26min

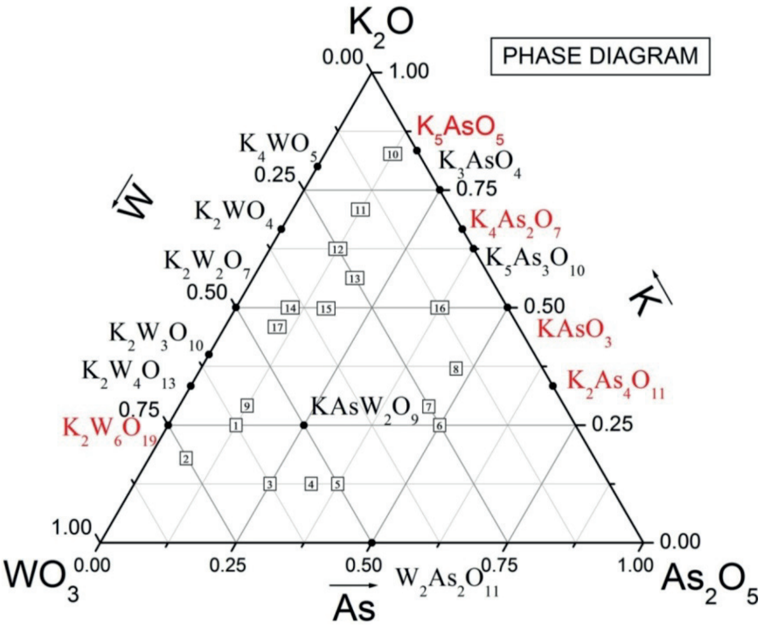

Figure 5.2: Selected 17 points in the phase diagram.

5.2.3. Results and discussion

All the points were separated into six groups corresponding to six regions in the phase diagram. They will be discussed in details in the following small sections.

1) Sample-1 and sample-2

The point 1 is located on the straight line between $K[AsW_2O_9]$ and $K_2W_6O_{19}$ while the point 2 is placed in the triangular region of $K[AsW_2O_9]$, $K_2W_6O_{19}$ and WO_3. Comparing two diffraction patterns (**Figure 5.3**), a third common phase besides $K[AsW_2O_9]$ and WO_3 is identified as $K_2W_6O_{19}$ [36]. Acorrding to this result, the straight line between $K_2W_6O_{19}$ and $K[AsW_2O_9]$ as well as the line between $K[AsW_2O_9]$ and WO_3 can be connected (**Figure 5.4**).

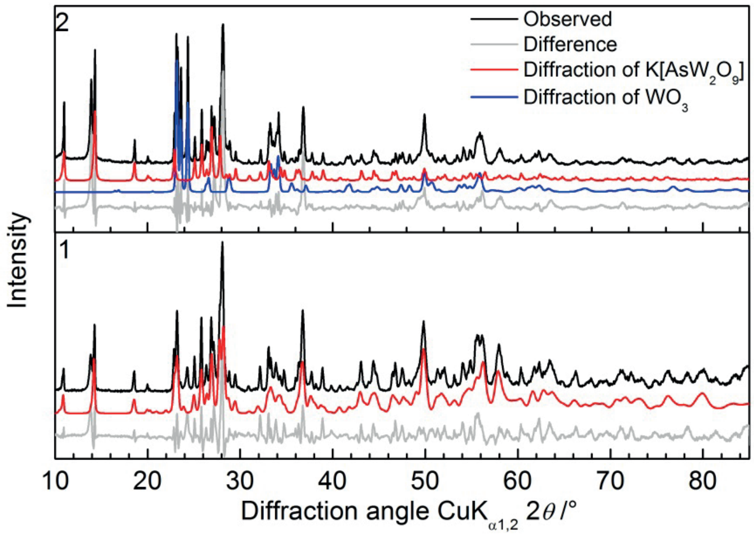

Figure 5.3: The X-ray powder diffraction patterns and Rietveld plots of the sample-1 and sample-2.

Table 5.2: X-ray diffraction data of the compound $K_2W_6O_{19}$.

d	I	d	I
6.37	64	2.03	5
5.55	1	1.969	1
5.06	1	1.943	1
4.22	1	1.912	6
3.81	39	1.848	4
3.80	16	1.826	18
3.50	1	1.760	1
3.35	4	1.690	3
3.27	20	1.649	11
3.16	100	1.646	11
2.98	4	1.635	11
2.64	10	1.591	4
2.44	30	1.582	8
2.40	2	1.463	7
2.12	5		

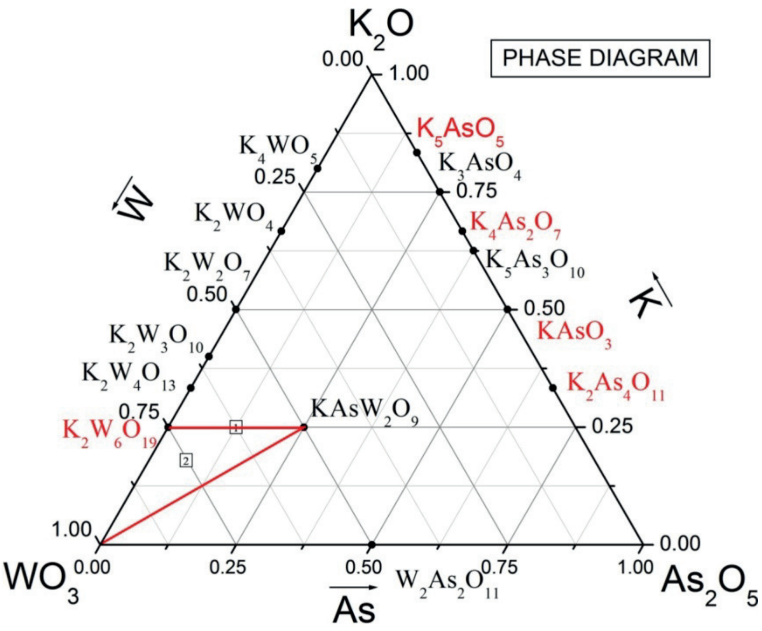

Figure 5.4: Phase diagram of K_2O-As_2O_5-WO_3, showing the locations of part of points (sample-1 and sample-2).

2) Sample-3, 4 and 5

The points 3, 4 and 5 are all located in the same region below the straight line between WO_3 and $K[AsW_2O_9]$.

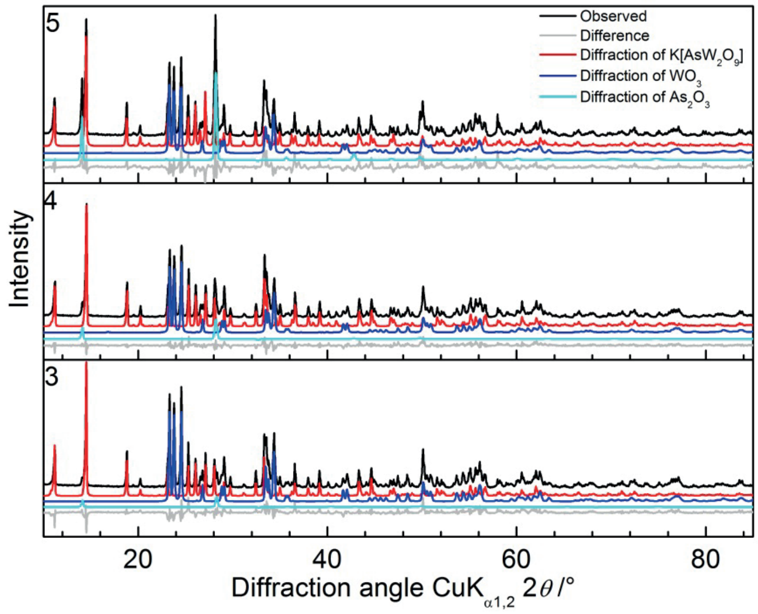

Figure 5.5: The X-ray powder diffraction patterns and Rietveld plots of the sample-3, 4 and 5.

There are several possible connections in this region, either $K[AsW_2O_9]$ connecting with $W_2As_2O_{11}$ or As_2O_5, or forming the triangle with points WO_3, $KAsO_3$ and $W_2As_2O_{11}$. Since all three diffraction patterns (**Figure 5.5**) show the existing of $K[AsW_2O_9]$, the last possibility can be omitted. The main distinguish of the former two guesses is the content of the third phase ($W_2As_2O_{11}$ or As_2O_5). By heating the samples (three times) to 1023 K for 24 hours, the X-ray diffraction patterns become stable. The patterns show a new phase with increasing intensity which can be identified as As_2O_3. It confirmed the guess of connecting $K[AsW_2O_9]$ and As_2O_5 (**Figure 5.6**). During the heating procedure, As_2O_5 lost oxygen and turned into As_2O_3.

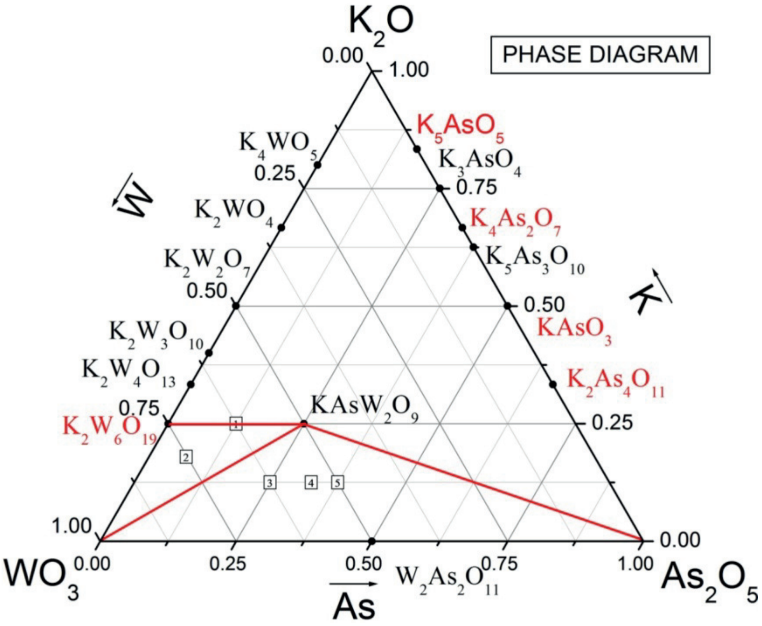

Figure 5.6: Phase diagram of K_2O-As_2O_5-WO_3, showing the locations of part of points (sample-1 – sample-5).

3) Sample-6 and sample-7

The points 6 and 7 are both located above the line between $K[AsW_2O_9]$ and As_2O_5. The difference of these two points is the relationship of their positions with the line between $K[AsW_2O_9]$ and $K_2As_4O_{11}$. From the diffraction patterns (**Figure 5.7**) we can see the sample-6 and sample-7 contain compound $K[AsW_2O_9]$ and an amorphous phase. The sample-6 contains so little amount of As_2O_5 or As_2O_3 that it could not be observed in the diffraction pattern. And the amorphous product can be contributed to $K_2As_4O_{11}$. The sample-7 contains more of the amorphous phase than the sample-6. So the most reasonable result is existing of a straight line between $K[AsW_2O_9]$ and $K_2As_4O_{11}$ (**Figure 5.8**).

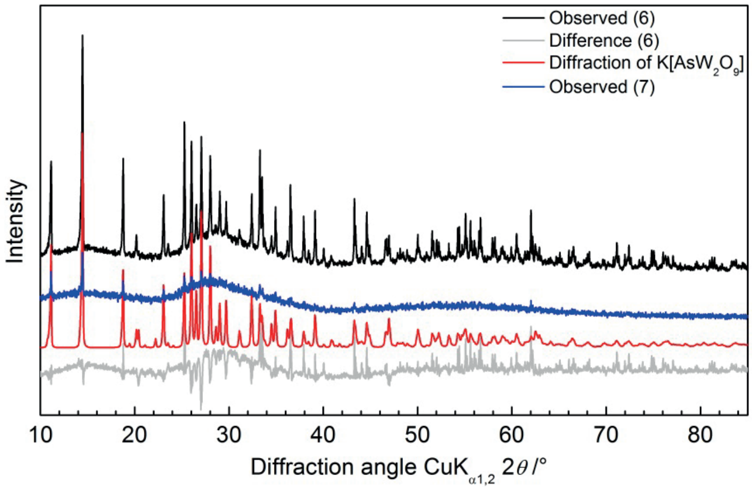

Figure 5.7: The X-ray powder diffraction patterns and Rietveld plots of the sample-6 and sample-7.

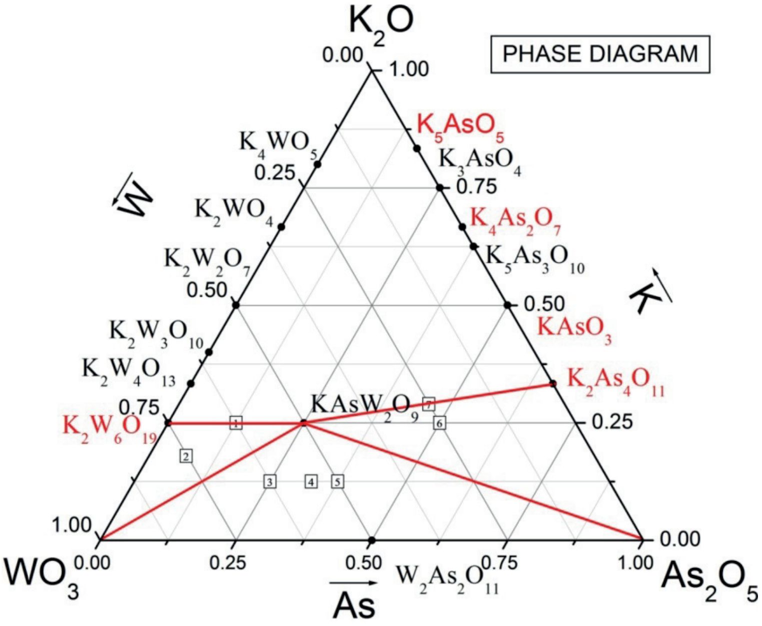

Figure 5.8: Phase diagram of K_2O-As_2O_5-WO_3, showing the locations of part of points (sample-1 – sample-7).

4) Sample-8 and sample-9

The point 8 is located above the line between $K_2W_3O_{10}$ and $K_2As_4O_{11}$ but below the line joining points $K[AsW_2O_9]$ and $KAsO_3$. The point 9 is placed on the straight line between $K[AsW_2O_9]$ and $K_2W_4O_{13}$.

The sample-8 contains KH_2AsO_4 which is the product of $KAsO_3$ absorbing one water molecular and an amorphous phase but $K[AsW_2O_9]$ (**Figure 5.9**). So the possibility of $K[AsW_2O_9]$ connecting with any known points above $K_2As_4O_{11}$ on the line of K_2O-As_2O_5 can be omitted and the point 8 should be out of the region of $K[AsW_2O_9]$. There are three possibilities, connecting $K_2As_4O_{11}$ with $K_2W_6O_{19}$, $K_2W_4O_{13}$ or $K_2W_3O_{10}$. And this can be determined by the diffraction pattern of sample-9 (**Figure 5.10**) whose point is on the line between $K[AsW_2O_9]$ and $K_2W_4O_{13}$.

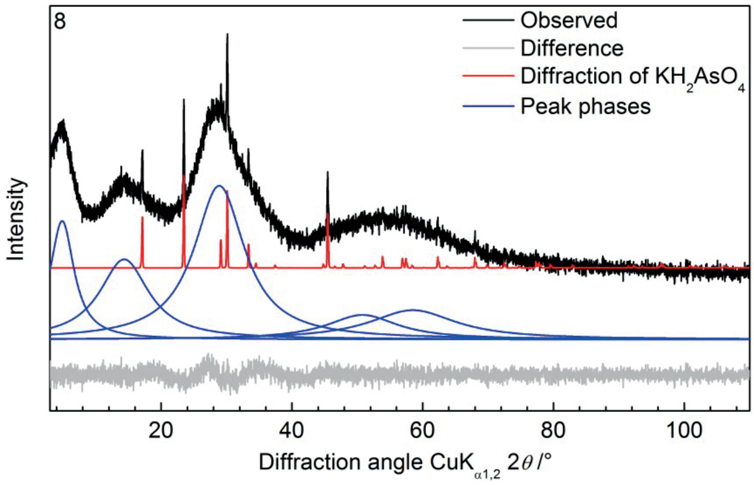

Figure 5.9: The X-ray powder diffraction pattern and Rietveld plot of the sample-8.

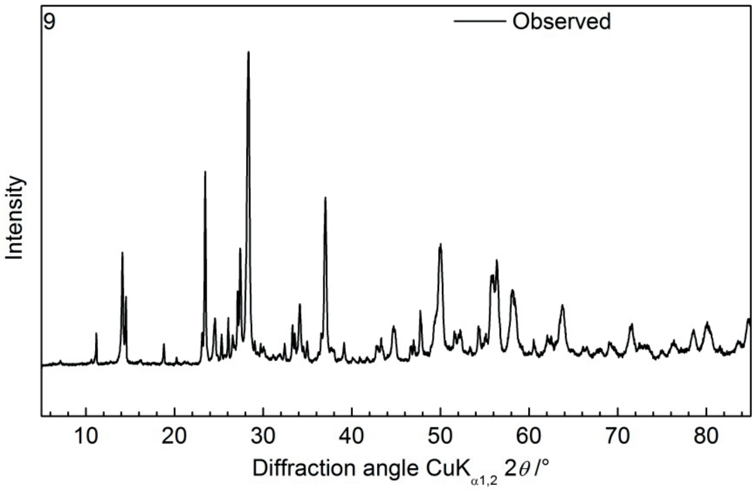

Figure 5.10: The X-ray diffraction pattern of the sample-9.

It is obvious that the sample-9 contains a large amount of $K_2W_6O_{19}$. This fact eliminates the possibility of the line between $K_2W_4O_{13}$ and $K[AsW_2O_9]$. It means also that this line between $K_2As_4O_{11}$ and $K_2W_4O_{13}$. The line between $K_2As_4O_{11}$ and $K_2W_3O_{10}$, and simultaneously between $K_2W_3O_{10}$ and $K[AsW_2O_9]$ locate the sample-9 containing three corner phases. The line between $K_2As_4O_{11}$ and $K_2W_6O_{19}$ means the sample-9 contains mostly $K_2W_6O_{19}$, $K_2As_4O_{11}$ and a third phase. The diffraction pattern of the sample-9 shows a large amount of $K_2W_6O_{19}$, a small amount of an amorphous phase, which is same as in the sample-

6 and a little amount of a third phase. This supports the possibility of the straight line between $K_2As_4O_{11}$ and $K_2W_6O_{19}$ (**Figure 5.11**).

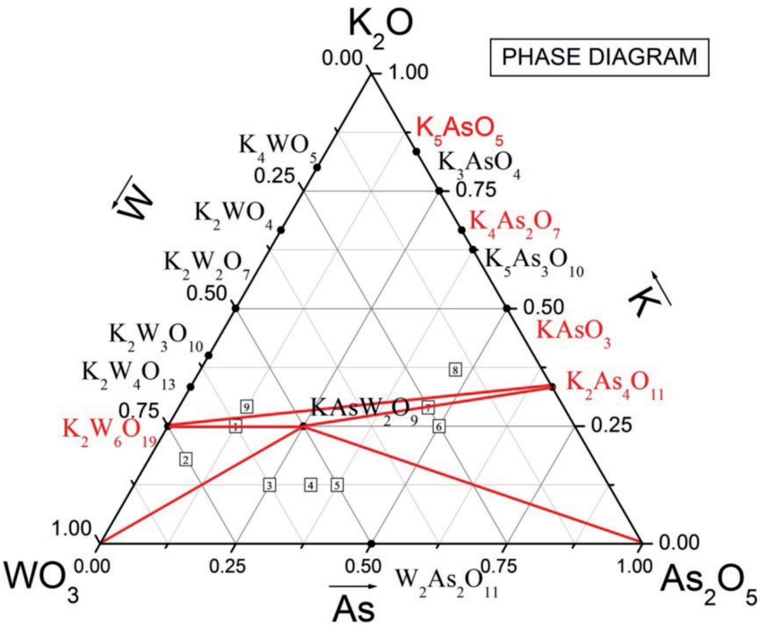

Figure 5.11: Phase diagram of K_2O-As_2O_5-WO_3, showing the locations of part of points (sample-1 – sample-9).

5) Samples from 10 to 13

The points 10 to 13 are located along the line between K_2O and $K[AsW_2O_9]$.

In all the diffraction patterns of these four samples (**Figure 5.12**), K_2WO_4 can be observed. So the main division is which compounds on the line K_2O-As_2O_5 connecting with K_2WO_4. The sample-10 contains an unknown phase. Sample-11 is located on the line K_2WO_4-K_3AsO_4 and is highly hygroscopic. It is known that $K_5As_3O_{10}$ is very hygroscopic. The combination of these two results is the reasonable straight line between K_2WO_4 and K_5AsO_5 and the line between K_2WO_4 and $K_5As_3O_{10}$. The sample-12 which is on the line between K_2WO_4 and $KAsO_3$ contains an amorphous phase besides K_2WO_4. In the sample-13, even higher content of the same amorphous phase can be observed. And they both are not hygroscopic. So the line between K_2WO_4 and $KAsO_3$ can be connected (**Figure 5.13**).

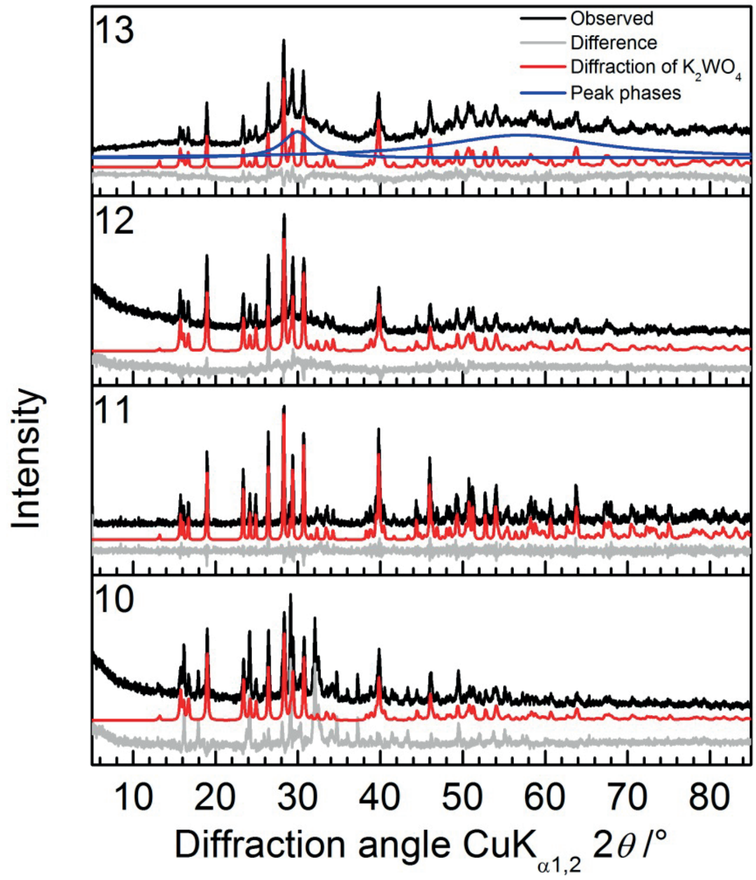

Figure 5.12: The X-ray powder diffraction patterns and Rietveld plots of the samples 10-13.

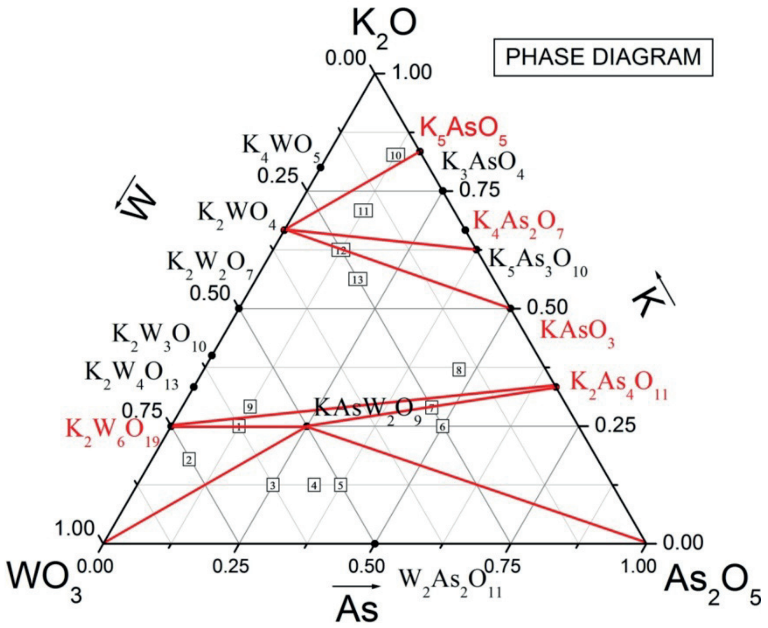

Figure 5.13: Phase diagram of K_2O-As_2O_5-WO_3, showing the locations of part of points (sample-1 – sample-13).

6) Samples from 14 to 17

The points 14, 15 and 16 are located on the straight line between $K_2W_2O_7$ and $KAsO_3$.

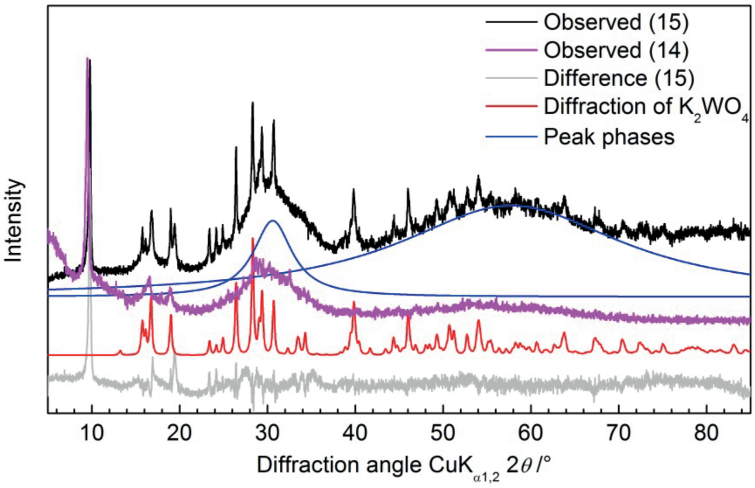

Figure 5.14: The X-ray powder diffraction patterns and Rietveld plots of the samples-14 and sample-15.

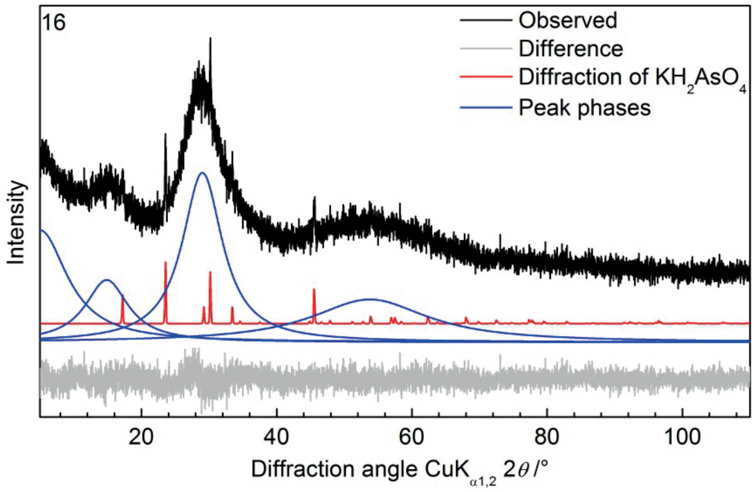

Figure 5.15: The X-ray powder diffraction pattern and Rietveld plot of the sample-16.

The sample-14 (**Figure 5.14**) contains an unknown phase along with an amorphous one. The unknown phase exhibits sharp diffraction features at 10° 2θ. Sample-15 contains K_2WO_4 besides sample-14. Sample-16 (**Figure 5.15**) is similar to 8 (KH_2AsO_4 and an amorphous phase). The sample-17 (**Figure 5.16**) contains all the phases of the sample-14 and other unknown phases. So in this region some new crystalline compounds may exist (**Figure 5.17**).

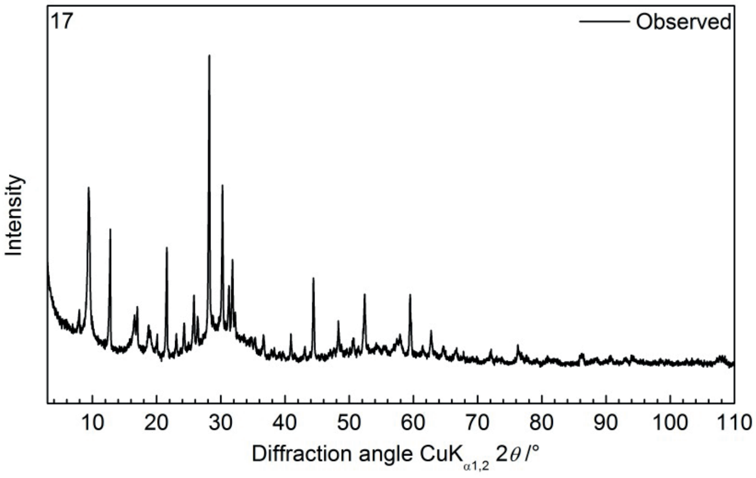

Figure 5.16: The X-ray diffraction pattern of the sample-17.

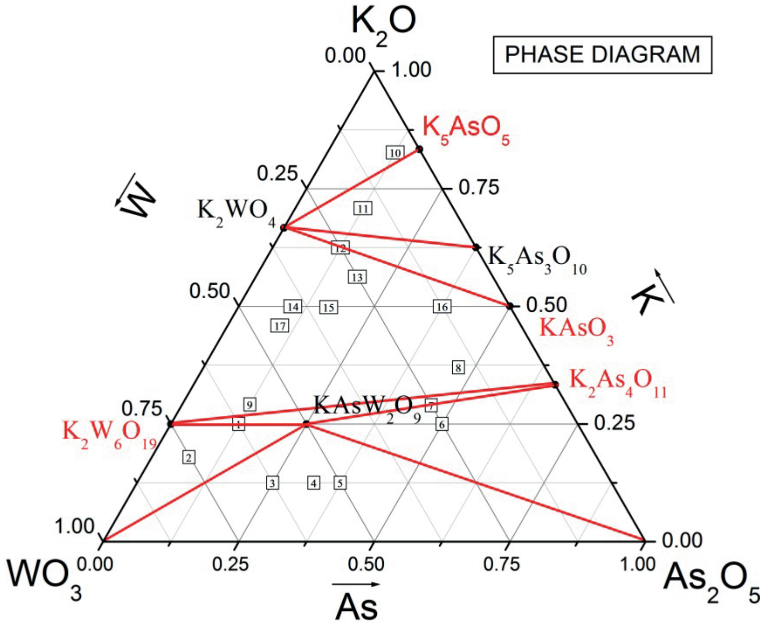

Figure 5.17: Phase diagram of K_2O-As_2O_5-WO_3, showing the locations of all points (sample-1 – sample-17).

Chapter 6 Summary and outlook

6.1. Summary in English

Within the scope of this thesis three novel compounds K[AsW_2O_9], Na[AsW_2O_9] and $Li_3AsW_7O_{25}$ were studied. The samples were synthesized using conventional solid-state reactions. As K[AsW_2O_9] exhibits promising second harmonic generation intensity (quite high compared with other known tungstates), the first and foremost focus of this study was to further tune the nonlinear optical susceptibility by replacing alkali metals with different sizes. Following the similar synthesis conditions as applied to K[AsW_2O_9], while it worked for the formation of Na[AsW_2O_9] but not for Li[AsW_2O_9]. Instead, under the similar synthesis condition using lithium precursor, another novel compound $Li_3AsW_7O_{25}$ was formed, which is centrosymmetric (*Pbca*) compared with either K[AsW_2O_9] or Na[AsW_2O_9], both of which are non-centrosymmetric ($P2_12_12_1$). The size of Li^+ cation may not be optimum fitting to the channels of the K/Na[AsW_2O_9] structure. The crystal structures of these three compounds were studied both from single crystal and powder in-house X-ray and neutron diffractions. The primary building units for both these structures are corner-sharing WO_6 and AsO_4 polyhedra. In the structure of K/Na[AsW_2O_9], WO_6 octahedra corner share to form layers which are further connected by AsO_4 tetrahedra, forming a framework of 12-membered ring channels. However, the structure of $Li_3AsW_7O_{25}$ is more complex compared with them with large unit cell, where each of seven independent WO_6 octahedra are corner-shared to build nanoscale blocks and further connected by AsO_4 tetrahedra. From structural point of view, smaller Na incorporation causes slightly higher distorted structure compared with potassium compound. Due to darker color and the associated optical absorption, the sodium sample showed a lower nonlinear optical susceptibility than that of K[AsW_2O_9]. The EDX analysis results for three compounds are in good agreement with the atomic composition of refined structures. The TG/DSC curves show one or two mass loss/peaks indicating the fusion or decomposition processes which start at least above 1050 K. The infrared and Raman spectra of K[AsW_2O_9] and Na[AsW_2O_9] are similar while that of $Li_3AsW_7O_{25}$ are much more complicated. All bands shown in the spectra are typical for oxides with WO_6 and AsO_4 polyhedra, which further are confirmed by density function theory (DFT) calculations. The absorption spectrum of $Li_3AsW_7O_{25}$ and detailed analyses using Kubelka-Munk and derivation of absorption spectrum fitting (DASF) method show the existing of both direct and indirect transition type. The electrochemical impedance spectra analysis result shows that

Na[AsW_2O_9] has the highest conductivity and K[AsW_2O_9] has the lowest value except the middle temperature range (a little bit higher than $Li_3AsW_7O_{25}$). These three compounds including K[AsW_2O_9] are characterized by temperature-dependent X-ray, neutron diffraction and Raman spectra. From the diffraction refined data, we get metric parameters and thermal expansion behavior. In K[AsW_2O_9], *b* cell parameter shows negative thermal expansion and *a* and *c* show positive thermal expansion. However, in other two compounds all the parameters exhibit positive thermal expansion. Analyzing from structural part, the distortion of polyhedra shows constant value and the most of M−O−M bond angles in the compounds A[AsW_2O_9] (A = K/Na) changed only small degrees. But the angles between two types of layers which are composed by corner-sharing WO_6 octahedra become larger. This may be caused by the enlargement of angle W1−O−W2 and be a reason of anisotropic thermal expansion behavior in K[AsW_2O_9]. Introducing the Debye-Einstein-Anharmonicity model to fit metric parameters, we get the Debye and Einstein temperatures for each compound. And using the autocorrelation function for spectra, we get consistent results with the diffraction data. However, the reason behind these anomalies is still not clear. The most part of phase diagram for K_2O-As_2O_5-WO_3 is completed by using particular molar ratios of raw materials and analyzing the X-ray diffraction pattern of the products. Some new crystalline compounds may exist in the middle region around the line between $K_2W_2O_7$ and $KAsO_3$.

6.2. Summray in German

Im Rahmen dieser Arbeit wurden die drei neuartigen Verbindungen K[AsW_2O_9], Na[AsW_2O_9] und $Li_3AsW_7O_{25}$ untersucht. Die Proben wurden durch konventionelle Festkörperreaktionen hergestellt. Da K[AsW_2O_9] eine vielversprechende Intensität für die Frequenzverdopplung aufweist (recht hoch verglichen mit anderen bekannten Wolframaten), wurde der Fokus dieser Studie auf die Anpassung der nonlinearen optischen Suszeptibilität durch Austausch mit Alkalimetallen verschiedener Größen gelegt. Die gleichen Synthesebedingungen, die für K[AsW_2O_9] angewendet wurden, funktionierten für Na[AsW_2O_9], jedoch nicht für Li[AsW_2O_9]. Stattdessen wurde unter diesen Bedingungen mit dem Lithiumpräkursor eine weitere neue Verbindung $Li_3AsW_7O_{25}$ hergestellt, welche, im Gegesatz zu den nicht zentrosymmterische Verbindungen K[AsW_2O_9] oder Na[AsW_2O_9] ($P2_12_12_1$), eine zentrosymmetrische Symmetrie aufweist (*Pbca*). Die Größe des Lithiumkations könnte nicht optimal passend für Kanäle in der K/Na[AsW_2O_9]-Struktur sein. Die Kristalle dieser drei Verbindungen wurden sowohl mit in-house Einkristall- und

Pulverröntgendiffraktometrie als auch Neutronenbeugung untersucht. Die primären Baueinheiten dieser Strukturen bestehen aus eckenverknüpften WO_6- und AsO_4-Polyedern. In der Struktur von K/Na[AsW_2O_9] bilden die eckenverknüpften WO_6-Oktaeder Schichten, welche durch AsO_4-Tetraeder verbunden sind, wodurch sich ein Gerüst aus 12-zähligen Ringkanälen bildet. Die Struktur von $Li_3AsW_7O_{25}$ ist jedoch komplexer, mit einer großen Einheitszelle, in der jeder von sieben unabhängigen WO_6-Oktaedern durch Eckenverknüpfung nanoskalige Baueinheiten bilden, welche weiter über AsO_4-Tetraeder verbunden sind. Vom strukturellen Standpunkt aus, führt der Einbau im Vergleich kleinerer Natriumatome zu stärker verzerrten Strukturen als bei den Kaliumverbindungen. Aufgrund der dunkleren Farbe und der damit verbundenen optischen Absorption zeigt die Natriumprobe eine niedrigere nonlineare optische Suszeptibilität als K[AsW_2O_9]. Die Ergebnisse der EDX-Analyse stimmen gut mit den atomaren Zusammensetzungen der verfeinerten Strukturen überein. Die TG/DSC-Kurven zeigen ein bis zwei Masseverluste/Signale, welche auf Fusions- oder Dekompositionsprozesse bei über mindestens 1050 K hindeuten. Die Infrarot- und Raman Spektren von K[AsW_2O_9] und Na[AsW_2O_9] sind ähnlich, wohingegen die von $Li_3AsW_7O_{25}$ wesentlich komplizierter sind. Alle in den Spektren gezeigten Banden sind typisch für Oxide mit WO_6- und AsO_4-Polyedern, was durch dichtefunktionaltheoretische (DFT) Berechnungen weiter bestätigt wird. Die Absorptionsspektren von $Li_3AsW_7O_{25}$ und die detaillierte Analyse mit den Methoden von Kubelka-Munk sowie derivation of absorption spectrum fitting (DASF) zeigen sowohl direkte als auch indirekte Übergänge. Das Ergebnis der elektrochemischen Impedanzspektroskopie zeigt die höchste Leitfähigkeit für Na[AsW_2O_9] und die niedrigste für K[AsW_2O_9] (mit Ausnahme des mittleren Temperaturbereichs, in der die Leitfähigkeit letzterer Verbindung leicht über der von $Li_3AsW_7O_{25}$ liegt). Die drei Verbindungen, inklusive K[AsW_2O_9], wurden mit temperaturabhängiger Röntgen-, Neutronenbeugung und Raman Spektroskopie. Aus den verfeinerten Beugungsdaten erhalten wir die metrischen Parameter und das thermische Ausdehnungsverhalten. In K[AsW_2O_9] zeigt der *b*-Zellparameter negative sowie *a*- und *c*-Parameter positive thermische Expansion. In den anderen zwei Verbindungen jedoch zeigen alle Parameter eine positive thermische Ausdehnung. Aus den strukturellen Analysen zeigt sich ein konstanter Wert für die Polyederverzerrung und die meisten M−O−M Bindungswinkel in den A[AsW_2O_9] (A = K/Na) Verbindungen ändern sich nur wenige Grad. Die Winkel zwischen zwei Typen von aus eckenverknüpften WO_6-Oktaedern bestehenden Schichten hingegen werden größer. Dies könnte durch die Aufweitung des W1−O−W2 Winkels hervorgerufen werden und damit ein Grund sein, für das anisotrope thermische

Ausdehnungsverhalten in K[AsW_2O_9]. Durch Einführung des Debye-Einstein-Anharmonizitätsmodells erhalten wir die Debye- und Einsteintemperaturen für jede der Verbindungen. Und unter Verwendung der Autokorrelation für Spektren erhalten wir mit den Beugungsdaten konsistente Ergebnisse. Die Ursache hinter diesen Anomalien ist jedoch weiterhin unklar. Der Hauptteil des Phasendiagramms im K_2O-As_2O_5 -WO_3 System ist vervollständigt durch die Verwendung der bestimmten molaren Verhältnisse der Ausgangsmaterialien und der Analyse der Röntgendiffraktogramme der erhaltenene Produkte. Einige neue kristalline Verbindungen könnten in der mittleren Region um die Linie zwischen $K_2W_2O_7$ und $KAsO_3$ existieren.

6.3. Outlook

Based on the investigations carried out on these three samples, several open questions are left, triggering further systematic studies as listed below:

a) Tuning the synthesis conditions for the formation of still hypothetical Li[AsW_2O_9]. In this regard, a prior density functional theory (DFT) calculation may guide the thermodynamic stability of the proposed compound. This also true for the isostructural Rb- and Cs-compounds. A positive appearance would be promising for the enhanced NLO susceptibility. Because either of Li, Rb or Cs can contract/broaden the channels, leading to more local distortion, thus to higher signal of SHG.

b) Try to figure out the underlying mechanism of the anomalous feature happened as observed from lattice thermal expansion, vibrational spectroscopic features analyzed by autocorrelation function. It is of critically importance to modify the thermal expansion model, as it significantly departs from the experimental observation at higher temperatures, based on either the spectroscopic or structural hints.

c) Expansion of the family members is proposed by replacing arsenic with other +5 valence ions and tungsten with molybdenum due to their comparable (similar) ionic radii.

d) To further increase the number of points in K_2O-As_2O_5-WO_3 phase diagram in search of more novel compounds.

Chapter 7 References

1. E. Lassner, W.-D. Schubert, E. Lüderitz, H.U. Wolf, Ullmann's Encyclopedia of Industrial Chemistry. 37 (2000) 498.
2. L.S. Palatnik, O.A. Obol'yaninova, M.N. Naboka, N.T. Gladkikh, Izv. Akad. Nauk SSSR, Neorg. Mater. 9 (1973) 801.
3. C.J. Howard, V. Luca, K.S. Knight, J. Phys.: Condens. Matter. 14 (2002) 377.
4. S. Tanisaki, J. Phys. Soc. Jpn. 15 (1960) 566.
5. S.K. Deb, Sol. Energy Mater. Sol. Cells. 92 (2008) 245.
6. A.M. El-Sayed, S.M.A. Mousa, Indian J. Chem. Technol. 12 (2005) 304.
7. Z.H. Zhang, X.T. Tao, J.J. Zhang, Y.X. Sun, C.Q. Zhang, B. Li, CrystEngComm. 15 (2013) 10197.
8. Y. Djaoued, P.V. Ashrit, S. Badilescu, R. Bruning, J. Sol-Gel Sci. Technol. 28 (2003) 235.
9. D.D. Xu, T.F. Jiang, D.J. Wang, L.P. Chen, L.J. Zhang, Z.W. Fu, L.L. Wang, T.F. Xie, ACS Appl. Mater. Interfaces. 6 (2014) 9321.
10. O. Berger, T. Hoffmann, W.J. Fischer, V. Melev, J. Mater. Sci.: Mater. Electron. 15 (2004) 483.
11. S.K. Gullapalli, R.S. Vemuri, F.S. Manciu, J.L. Enriquez, C.V. Ramana, J. Vac. Sci. Technol., A. 28 (2010) 824.
12. D.B. Migas, V.L. Shaposhnikov, V.N. Rodin, V.E. Borisenko, J. Appl. Phys. 108 (2010) 093713.
13. Y.A. Barabanenkov, N.D. Zakharov, I.P. Zibrov, V.P. Filonenko, P. Werner, A.I. Popov, M.D. Valkovskii, Acta Crystallogr., Sect. B: Struct. Sci. 49 (1993) 169.
14. M. Sundberg, N.D. Zakharov, I.P. Zibrov, Y.A. Barabanenkov, V.P. Filonenko, P. Werner, Acta Crystallogr., Sect. B: Struct. Sci. 49 (1993) 951.
15. K. Viswanathan, K. Brandt, E. Salje, J. Solid State Chem. 36 (1981) 45.
16. M.M. Dobson, R.J.D. Tilley, Acta Crystallogr., Sect. B: Struct. Sci. 44 (1988) 474.
17. I.J. Mccolm, R. Steadman, S.J. Wilson, J. Solid State Chem. 23 (1978) 33.
18. A. Magneli, Acta Crystallogr. 6 (1953) 495.
19. M. Sundberg, Acta Crystallogr., Sect. B: Struct. Crystallogr. Cryst. Chem. 32 (1976) 2144.
20. D.B. Migas, V.L. Shaposhnikov, V.E. Borisenko, J. Appl. Phys. 108 (2010) 093714.

21. A.A. Bolzan, B.J. Kennedy, C.J. Howard, Aust. J. Chem. 48 (1995) 1473.
22. P. Labbe, Key Eng. Mater. 68 (1992) 293.
23. R. Brusetti, P. Bordet, J. Marcus, J. Solid State Chem. 172 (2003) 148.
24. J.M. Reau, Fouassie.C, G. Leflem, J.Y. Barruad, J.P. Doumerc, Hagenmul.P, Revue De Chimie Minerale. 7 (1970) 975.
25. C.H. Ruscher, K.R. Dey, T. Debnath, I. Horn, R. Glaum, A. Hussain, J. Solid State Chem. 181 (2008) 90.
26. Q. Zhong, J.R. Dahn, K. Colbow, Phys. Rev. B: Condens. Matter Mater. Phys. 46 (1992) 2554.
27. A. Magneli, Acta Chem. Scand. 7 (1953) 315.
28. A. Hussain, L. Kihlborg, Acta Crystallogr., Sect. A: Cryst. Phys., Diffr., Theor. Gen. Crystallogr. 32 (1976) 551.
29. R.K. Stanley, R.C. Morris, W.G. Moulton, Phys. Rev. B: Condens. Matter Mater. Phys. 20 (1979) 1903.
30. J. Ranninger, K.P. Sinha, Proc. - Indian Acad. Sci., Chem. Sci. 95 (1985) 93.
31. B. Darriet, M. Rat, J. Galy, C. R. Seances Acad. Sci., Ser. C. 271 (1970) 1324.
32. H.Y. Chang, T. Sivakumar, K.M. Ok, P.S. Halasyamani, Inorg. Chem. 47 (2008) 8511.
33. F. Galasso, W. Darby, J. Phys. Chem. 68 (1964) 1253.
34. M. Maczka, A.G. Souza Filho, W. Paraguassu, P.T.C. Freire, J. Mendes Filho, J. Hanuza, Prog. Mater. Sci. 57 (2012) 1335.
35. R.J.H. Gelsing, H.N. Stein, J.M. Stevels, Recl. Trav. Chim. Pays-Bas. 84 (1965) 1452.
36. S. Sakka, Bull. Inst. Chem. Res., Kyoto Univ. 46 (1969) 300.
37. T. Betz, R. Hoppe, J. Less-Common Met. 105 (1985) 87.
38. W.H. Zachariasen, H.A. Plettinger, Acta Crystallogr. 14 (1961) 229.
39. R.W. Goranson, F.C. Kracek, J. Chem. Phys. 3 (1935) 87.
40. F.X.N.M. Kools, A.S. Koster, G.D. Rieck, Acta Crystallogr., Sect. B: Struct. Crystallogr. Cryst. Chem. B26 (1970) 1974.
41. H.-C. Mumm, H. Müller-Buschbaum, J. Less-Common Met. 142 (1998) 85.
42. A.J.V.D. Berg, C.a.H. Juffermans, J. Appl. Crystallogr. 15 (1982) 114.
43. T.J. Mormann, W. Jeitschko, Inorg. Chem. 39 (2000) 4219.
44. A.W. Sleight, J.D. Bierlein, P.E. Bierstedt, J. Chem. Phys. 62 (1975) 2826.
45. K. Okada, J. Ossaka, S. Iwai, Acta Crystallogr., Sect. B: Struct. Crystallogr. Cryst. Chem. 35 (1979) 2189.

46. V.N. Kolobanov, I.A. Kamenskikh, V.V. Mikhailin, I.N. Shpinkov, D.A. Spassky, B.I. Zadneprovsky, L.I. Potkin, G. Zimmerer, Nucl. Instrum. Methods Phys. Res., Sect. A. 486 (2002) 496.
47. A.W. Sleight, Acta Crystallogr., Sect. B: Struct. Crystallogr. Cryst. Chem. B28 (1972) 2899.
48. F.J. Manjón, D. Errandonea, N. Garro, J. Pellicer-Porres, P. Rodríguez-Hernández, S. Radescu, J. López-Solano, A. Mujica, A. Muñoz, Phys. Rev. B: Condens. Matter Mater. Phys. 74 (2006) 144111.
49. S.H. Yoon, D.-W. Kim, S.-Y. Cho, K.S. Hong, J. Eur. Ceram. Soc. 26 (2006) 2051.
50. Q. Zhang, W.-T. Yao, X. Chen, L. Zhu, Y. Fu, G. Zhang, L. Sheng, S.-H. Yu, Cryst. Growth Des. 7 (2007) 1423.
51. S. Dey, R.A. Ricciardo, H.L. Cuthbert, P.M. Woodward, Inorg. Chem. 53 (2014) 4394.
52. N.J. Dunning, H.D. Megaw, Trans. Faraday Soc. 42 (1946) 705.
53. O. Heyer, N. Hollmann, I. Klassen, S. Jodlauk, L. Bohatý, P. Becker, J.A. Mydosh, T. Lorenz, D. Khomskii, J. Phys.: Condens. Matter. 18 (2006) L471.
54. V.B. Mikhailik, H. Kraus, G. Miller, M.S. Mykhaylyk, D. Wahl, J. Appl. Phys. 97 (2005) 083523.
55. D.L. Stern, R.K. Grasselli, J. Catal. 167 (1997) 570.
56. A. Kuzmin, J. Purans, R. Kalendarev, D. Pailharey, Y. Mathey, Electrochim. Acta. 46 (2001) 2233.
57. D.W. Kim, I.-S. Cho, S.S. Shin, S. Lee, T.H. Noh, D.H. Kim, H.S. Jung, K.S. Hong, J. Solid State Chem. 184 (2011) 2103.
58. L. Kihlborg, E. Gebert, Acta Crystallogr., Sect. B: Struct. Crystallogr. Cryst. Chem. B26 (1970) 1020.
59. M.B.A. Dahlborg, G. Svensson, T. Ouvarova, Acta Crystallogr., Sect. C: Cryst. Struct. Commun. 56 (2000) 397.
60. W. Jeitschko, A.W. Sleight, Acta Crystallogr., Sect. B: Struct. Crystallogr. Cryst. Chem. B30 (1974) 2088.
61. Jeitschk.W, A.W. Sleight, Acta Crystallogr., Sect. B: Struct. Crystallogr. Cryst. Chem. B 28 (1972) 3174.
62. E.G. Steward, H.P. Rooksby, Acta Crystallogr. 4 (1951) 503.
63. J.A. Baguo, S. Natansohn, J. Appl. Crystallogr. 2 (1969) 252.
64. G. King, A.M. Abakumov, J. Hadermann, A.M. Alekseeva, M.G. Rozova, T. Perkisas, P.M. Woodward, G. Van Tendeloo, E.V. Antipov, Inorg. Chem. 49 (2010) 6058.

65. E. Gebert, L. Kihlborg, Acta Chem. Scand. 23 (1969) 221.
66. V.A. Efremov, Russ. Chem. Rev. 59 (1990) 627.
67. K. Nassau, H.J. Levinstein, G.M. Loiacono, J. Phys. Chem. Solids. 26 (1965) 1805.
68. K. Nassau, P.B. Jamieson, J.W. Shiever, J. Phys. Chem. Solids. 30 (1969) 1225.
69. K. Nassau, J.W. Shiever, E.T. Keve, J. Solid State Chem. 3 (1971) 411.
70. S. Sumithra, A.M. Umarji, Solid State Sci. 6 (2004) 1313.
71. J.S.O. Evans, T.A. Mary, A.W. Sleight, J. Solid State Chem. 137 (1998) 148.
72. P.M. Forster, A.W. Sleight, Int. J. Inorg. Mater. 1 (1999) 123.
73. N. Imanaka, M. Hiraiwa, G. Adachi, H. Dabkowska, A. Dabkowski, J. Cryst. Growth. 220 (2000) 176.
74. A.K. Sriraman, A.K. Tyagi, Thermochim. Acta. 406 (2003) 29.
75. G. Blasse, J. Inorg. Nucl. Chem. 28 (1966) 1488.
76. P.J.L. Hodeau, M. Gondrand, M. Labeau, J.C. Joubert, Acta Crystallogr., Sect. B: Struct. Crystallogr. Cryst. Chem. B34 (1978) 3543.
77. G. Bayer, J. Am. Ceram. Soc. 43 (1960) 495.
78. W. Kunnmann, S.L. Placa, L.M. Corliss, J.M. Hastings, J. Phys. Chem. Solids. 29 (1968) 1359.
79. A. Castro, P. Millan, R. Enjalbert, E. Snoeck, J. Galy, Mater. Res. Bull. 29 (1994) 871.
80. K.S. Knight, Mineral. Mag. 56 (1992) 399.
81. G.J. Mccarthy, R.D. Fischer, G. G. Johnson, J.a.C.E. Gooden, NBS Special Publication (United States). 364 (1972) 397.
82. J.S.O. Evans, T.A. Mary, T. Vogt, M.A. Subramanian, A.W. Sleight, Chem. Mater. 8 (1996) 2809.
83. M. Lundberg, Acta Chem. Scand. 26 (1972) 2932.
84. A. Santoro, R.S. Roth, D. Minor, Acta Crystallogr., Sect. B: Struct. Crystallogr. Cryst. Chem. 35 (1979) 1202.
85. S.R.S. Prabaharan, T.T. Yong, A. Fauzi, M.S. Michael, J. Power Sources. 97-98 (2001) 535.
86. M. Gateshki, J.M. Igartua, J. Phys.: Condens. Matter. 16 (2004) 6639.
87. S.A. Ivanov, S.G. Eriksson, J. Erikssen, R. Tellgren, H. Rundlof, Mater. Res. Bull. 39 (2004) 615.
88. S.S.M. Bhat, D. Swain, C. Narayana, M. Feygenson, J.C. Neuefeind, N.G. Sundaram, Cryst. Growth Des. 14 (2014) 835.
89. J. Goodey, J. Broussard, P.S. Halasyamani, Chem. Mater. 14 (2002) 3174.

90. Y.Y. Li, W.D. Cheng, H. Zhang, C.S. Lin, W.L. Zhang, L. Geng, G.L. Chai, Z.Z. Luo, Z.Z. He, Dalton Trans. 40 (2011) 7357.
91. J. Goodey, K. Min Ok, J. Broussard, C. Hofmann, F.V. Escobedo, P.S. Halasyamani, J. Solid State Chem. 175 (2003) 3.
92. G. Schileo, A. Dias, R.L. Moreira, T.J. Jackson, P.A. Smith, K.T.S. Chung, A. Feteira, J. Am. Ceram. Soc. 97 (2014) 1096.
93. H. Ohtsuka, A. Yamaji, T. Okada, Solid State Ionics. 14 (1984) 283.
94. T. Kar, R.N.P. Choudhary, J. Mater. Sci. Lett. 19 (2000) 809.
95. M. MąCzka, A.V. Knyazev, N.Y. Kuznetsova, M. Ptak, L. Macalik, J. Raman Spectrosc. 42 (2011) 529.
96. J.R. Reddy, G. Ravi, N.K. Veldurthi, R. Velchuri, S. Pola, M. Vithal, B. Sreedhar, Z. Anorg. Allg. Chem. 639 (2013) 794.
97. D.E. Cox, G. Shirane, B.C. Frazer, J. Appl. Phys. 38 (1967) 1459.
98. J.H.G. Bode, A.B. Vanoosterhout, J. Lumin. 10 (1975) 237.
99. C.P. Khattak, D.E. Cox, F.F.Y. Wang, J. Solid State Chem. 17 (1976) 323.
100. D. Reinen, H. Weitzel, Z. Anorg. Allg. Chem. 424 (1976) 31.
101. Z.M. Fu, Sci. China, Ser. A: Math., Phys., Astron. Technol. Sci. 34 (1991) 455.
102. Z.M. Fu, W.X. Li, Sci. China, Ser. A: Math., Phys., Astron. Technol. Sci. 38 (1995) 309.
103. Z.M. Fu, W.X. Li, Sci. China, Ser. A: Math., Phys., Astron. 39 (1996) 981.
104. M. Gateshki, J.M. Igartua, J. Phys.: Condens. Matter. 15 (2003) 6749.
105. M. Gateshki, J.M. Igartua, E. Hernandez-Bocanegra, J. Phys.: Condens. Matter. 15 (2003) 6199.
106. J.B. Philipp, P. Majewski, L. Alff, A. Erb, R. Gross, T. Graf, M.S. Brandt, J. Simon, T. Walther, W. Mader, D. Topwal, D.D. Sarma, Phys. Rev. B: Condens. Matter Mater. Phys. 68 (2003) 144431.
107. M.C. Viola, M.J. Martinez-Lope, J.A. Alonso, J.L. Martinez, J.M. De Paoli, S. Pagola, J.C. Pedregosa, M.T. Fernandez-Diaz, R.E. Carbonio, Chem. Mater. 15 (2003) 1655.
108. F. Zhao, Z. Yue, Z. Gui, L. Li, Jpn. J. Appl. Phys. 44 (2005) 8066.
109. C.A. Lopez, J. Curiale, M.D.C. Viola, J.C. Pedregosa, R.D. Sanchez, Physica B (Amsterdam, Neth.). 398 (2007) 256.
110. K.R. Chakraborty, A. Das, P.S.R. Krishna, S.M. Yusuf, S.J. Patwe, S.N. Achary, A.K. Tyagi, J. Alloys Compd. 457 (2008) 15.
111. D.E. Bugaris, J.P. Hodges, A. Huq, H.C. Zur Loye, J. Solid State Chem. 184 (2011) 2293.

112. O. Sahnoun, H. Bouhani-Benziane, M. Sahnoun, M. Driz, C. Daul, Comput. Mater. Sci. 77 (2013) 316.

113. R.L. Andrews, A.M. Heyns, P.M. Woodward, Dalton Trans. 44 (2015) 10700.

114. V.V. Atuchin, B.I. Kidyarov, N.V. Pervukhina, Comput. Mater. Sci. 30 (2004) 411.

115. B.I. Kidyarov, V.V. Atuchin, Ferroelectrics. 444 (2013) 144.

116. E.V. Alekseev, O. Felbinger, S. Wu, T. Malcherek, W. Depmeier, G. Modolo, T.M. Gesing, S.V. Krivovichev, E.V. Suleimanov, T.A. Gavrilova, L.D. Pokrovsky, A.M. Pugachev, N.V. Surovtsev, V.V. Atuchin, J. Solid State Chem. 204 (2013) 59.

117. L. Smart, E. Moore, Solid State Chemistry : An Introduction, 3rd ed.; Taylor and Francis. Boca Raton, 2005.

118. C. Chen, B. Wu, A. Jiang, G. You, Sci. Sin., Ser. B (Engl. Ed.). 28 (1985) 235.

119. J. Liebertz, S. Stahr, Z. Kristallogr. 165 (1983) 91.

120. C. Chen, Y. Wu, A. Jiang, B. Wu, G. You, R. Li, S. Lin, J. Opt. Soc. Am. B. 6 (1989) 616.

121. F.C. Zumsteg, J.D. Bierlin, T.E. Gier, J. Appl. Phys. 47 (1976) 4980.

122. L.I. Isaenko, A.A. Merkulov, V.I. Tjurikov, V.V. Atuchin, L.V. Sokolov, E.M. Trukhanov, J. Cryst. Growth. 171 (1997) 146.

123. G. Hansson, H. Karlsson, S.H. Wang, F. Laurell, Appl. Opt. 39 (2000) 5058.

124. H.-S. Ra, K.M. Ok, P.S. Halasyamani, J. Am. Chem. Soc. 125 (2003) 7764.

125. J.-H. Kim, J. Baek, P.S. Halasyamani, Chem. Mater. 19 (2007) 5637.

126. A.A. Kaminskii, J.B. Gruber, S.N. Bagaev, K. Ueda, U. Hommerich, J.T. Seo, D. Temple, B. Zandi, A.A. Kornienko, E.B. Dunina, A.A. Pavlyuk, R.F. Klevtsova, F.A. Kuznetsov, Phys. Rev. B: Condens. Matter Mater. Phys. 65 (2002) 125108.

127. C. Cascales, M.D. Serrano, F. Esteban-Betegon, C. Zaldo, R. Peters, K. Petermann, G. Huber, L. Ackermann, D. Rytz, C. Dupre, M. Rico, J. Liu, U. Griebner, V. Petrov, Phys. Rev. B: Condens. Matter Mater. Phys. 74 (2006) 174114.

128. A.A. Kovalyov, V.V. Preobrazhenskii, M.A. Putyato, O.P. Pchelyakov, N.N. Rubtsova, B.R. Semyagin, V.E. Kisel, S.V. Kuril'chik, N.V. Kuleshov, Laser Phys. Lett. 8 (2011) 431.

129. X.Y. Liu, S.L. Qu, Y. Tan, F. Chen, Appl. Opt. 50 (2011) 930.

130. P. Zhao, M.M. Murshed, E.V. Alekseev, V.V. Atuchin, A.M. Pugachev, T.M. Gesing, Mater. Res. Bull. 60 (2014) 258.

131. P. Zhao, M. Mangir Murshed, A. Huq, H.K. Grossmann, L. Mädler, E.V. Alekseev, T.M. Gesing, J. Solid State Chem. 226 (2015) 81.

132. G.M. Sheldrick, SHELXS97 Program for Solution of Crystal Structures, University of Göttingen, Germany, 1997.
133. N.E. Brese, M. O'keeffe, Acta Crystallogr., Sect. B: Struct. Sci. 47 (1991) 192.
134. K. Robinson, G.V. Gibbs, P.H. Ribbe, Science (Washington, DC, U. S.). 172 (1970) 567.
135. H. Siebert, Z. Anorg. Allg. Chem. 275 (1954) 225.
136. S.K. Kurtz, T.T. Perry, J. Appl. Phys. 39 (1968) 3798.
137. A.C. Larson, R.B.V. Dreele, General Structure Analysis System (GSAS), Los Alamos National Laboratory Report LAUR. (2004) 86.
138. B.H. Toby, J. Appl. Crystallogr. 34 (2001) 210.
139. A. Hussain, Chem. Scr. 11 (1977) 224.
140. D. Mezaoui, M.M. Borel, A. Leclaire, A. Rebbah, J. Provost, B. Raveau, J. Solid State Chem. 136 (1998) 305.
141. R. Lopez, R. Gomez, J. Sol-Gel Sci. Technol. 61 (2012) 1.
142. P. Kubelka, J. Opt. Soc. Am. 38 (1948) 448.
143. P. Kubelka, F. Munk, Zeitschrift für Technische Physik 12 (1931) 593.
144. M.N. Yoder, IEEE Trans. Electron Devices. 43 (1996) 1633.
145. D. Souri, Z.E. Tahan, Appl. Phys. B: Lasers Opt. 119 (2015) 273.
146. K. Takenaka, Sci. Technol. Adv. Mater. 13 (2012) 013001.
147. E.-J. Liang, Recent Pat. Mater. Sci. 3 (2010) 106.
148. T.A. Mary, J.S.O. Evans, T. Vogt, A.W. Sleight, Science (Washington, DC, U. S.). 272 (1996) 90.
149. E.J. Liang, Y. Liang, Y. Zhao, J. Liu, Y.J. Jiang, J. Phys. Chem. A. 112 (2008) 12582.
150. S.N. Achary, G.D. Mukherjee, A.K. Tyagi, S.N. Vaidya, J. Mater. Sci. 37 (2002) 2501.
151. W. Miller, C.W. Smith, D.S. Mackenzie, K.E. Evans, J. Mater. Sci. 44 (2009) 5441.
152. J.S.O. Evans, T.A. Mary, A.W. Sleight, J. Solid State Chem. 133 (1997) 580.
153. T.M. Gesing, C.B. Mendive, M. Curti, D. Hansmann, G. Nenert, P.E. Kalita, K.E. Lipinska, A. Huq, A.L. Cornelius, M.M. Murshed, Z. Kristallogr. 228 (2013) 532.
154. M.M. Murshed, C.B. Mendive, M. Curti, G. Nénert, P.E. Kalita, K. Lipinska, A.L. Cornelius, A. Huq, T.M. Gesing, Mater. Res. Bull. 59 (2014) 170.
155. M. Mangir Murshed, C.B. Mendive, M. Curti, M. Šehović, A. Friedrich, M. Fischer, T.M. Gesing, J. Solid State Chem. 229 (2015) 87.
156. A. Einstein, Ann. Phys. 22 (1907) 180.
157. P. Debye, Annalen der Physik. 334 (1912) 789.
158. A.R. Oganov, P.I. Dorogokupets, J. Phys.: Condens. Matter. 16 (2004) 1351.

159. E.K.H. Salje, M.A. Carpenter, T. Malcherek, T.B. Ballaran, Eur. J. Mineral. 12 (2000) 503.

160. L. Robben, T.M. Gesing, 22nd DGK. (2014).

161. P.S. Halasyamani, Chem. Mater. 16 (2004) 3586.

162. M. Westerlund-Sundbäck, Acta Chem. Scand. 25 (1971) 1429.

163. E.M. Levin, H.F. Mcmurdie, F.P. Hall, Phase diagrams for ceramists, 1st ed.; American Ceramic Society. Columbus, Ohio, 1956.

164. J. Hornstra, H. Verweij, Acta Crystallogr., Sect. B: Struct. Crystallogr. Cryst. Chem. (1980) 1634.

165. F. Emmerling, M. Idilbi, C. Röhr, Z. Naturforsch., B: J. Chem. Sci. 57b (2002) 599.

166. C. Duc-Mauge, H. Guerin, Bull. Soc. Chim. Fr. (1957) 995.

Curriculum vitae

Name	Pei Zhao
E-mail	zhaopeide@yeah.net
Date and place of birth	Oct 24th, 1986, China

Education

09/2005 – 07/2009	Bachelor of Science on Material Chemistry Faculty of chemistry and chemical engineering, Henan University, China
09/2009 – 06/2012	Master of Science Master thesis: Synthesis and Characterization of Open-Framework Metal Borates and Bimetal Phosphates Fujian Institute of Research on the Structure of Matter, Chinese Academy of Sciences, China
09/2012 till now	Study in the group of Solid State Chemical Crystallography, Institute of Inorganic Chemistry and Crystallography, the University of Bremen, Germany

Publications during PhD study

Articles

1. P. Zhao, M. M. Murshed, E. V. Alekseev, V. V. Atuchin, A. M. Pugachev, Th. M. Gesing, Synthesis, structure and properties of Na[AsW_2O_9]. Mat. Res. Bull. 60 (2014) 258-263.
2. P. Zhao, M. M. Murshed, A. Huq, H. K. Grossmann, L. Mädler, E. V. Alekseev, Th. M. Gesing, Nanoscale building blocks in a novel lithium arsenotungsten bronze: synthesis and characterization. J. Solid State Chem. 226 (2015) 81-87.
3. P. Zhao, M. M. Murshed, A. Huq, E. V. Alekseev, Th. M. Gesing, Three alkali metal arsenotungstates: structures, properties and temperature-dependent behavior study, manuscript in preparation.

Conference abstract

1. P. Zhao, M. M. Murshed, E. V. Alekseev, Th M. Gesing, Synthesis, crystal structure and anisotropic thermal expansion of $KAsW_2O_9$, 16th Norddeutsche Doktorandenkolloqium (NDDK), September 19-20, 2013, Bremen, Germany.

2. P. Zhao, M. M. Murshed, E. V. Alekseev, Th M. Gesing, Synthesis, structure and characterization of $Li_3AsW_7O_{25}$, 22nd Annual Conference of the German Crystallographic Society (DGK), March 17-20, 2014, Berlin, Germany.
3. M. M. Murshed, P. Zhao, E. V. Alekseev, A. Huq, Th. M. Gesing, Modelling of lattice thermal expansion of complex oxides with intrinsic anharmonicity, 23rd Congress and Gerneral Assembly of the International Union of Crystallography (IUCr), August 5-12, 2014, Montreal, Canada.
4. P. Zhao, M. M. Murshed, A. Huq, E. V. Alekseev, Th. M. Gesing, Thermal expansion properties in the arsenotungstate compounds, 1st Meeting of the Young Crystallorgraphers, September 28-30, 2014, Bremen, Germany.
5. P. Zhao, M. M. Murshed, A. Huq, E. V. Alekseev, Th. M. Gesing, Thermal expansion behaviors of three alkali metal arsenotungstates, 23rd Annual Conference of the German Crystallographic Society (DGK), March 16-19, 2015, Göttingen, Germany.

Acknowledgement

I would like to thank all the people along the way over the past three years of my PhD work. They gave me the courage to overcome variety of difficulties, lead a happy and fulfilled life here in Germany. They have shown lots of patient, encouragements and their knowledge to taciturn maybe sometime clumsy of me. The top person on the list is my supervisor Prof. Thorsten M. Gesing. He gave me the opportunity to do this PhD thesis in his working group. His advices, ideas, support and discussions are very helpful to lead my work to the point. I am grateful for the great chances to attend domestic conferences and do the measurements in Oak Ridge National Laboratory which can get the latest development in this major field, broad my view sight and much more.

My sincere thank also goes to Dr. M. Mangir Murshed for his constant support in all questions as best as he can. I have greatly benefited from the manifold discussions with him and corrections of my manuscripts.

Great thank all my colleagues in the CKfS group: Andrea Kirsch, Ariane Friedemann, Elena Merzlykova, Gabriele Ebert, Hilke Petersen, Irma Poltz, Julia Butzlaff, Kristin Hoffmann, Dr. Lars Robben, Malik Šehović, Mathias Gogolin, Michael Teck, Dr. M. Shahidur Rahman and Niels Lefeld for their scientific and moral supports and their ears for all my concerns and doubts. I have enjoyed their company.

Prof. Evgeny V. Alekseev recommended me to my supervisor Prof. Gesing for this PhD study. My work is also based on his research. Thanks for the discussions and guidance in the beginning stage, his scholastic suggestions afterwards and being a reviewer of this thesis.

I would like to thank the following people for technical support at various instruments and calculations: J. Birkenstock, M. Wendschuh (XRD), A. Huq, M. J. Kirkham (neutron diffraction), F. Andre, K. Robert, F. Langer (EIS), H. K. Grossmann, L. Mädler (UV-vis), V. V. Atuchin, A. M. Pugachev (NLO), C. B. Mendive, D. Hansmann, M. Fischer (DFT). Especially thank all the members of Crystallography for the long time kindly help.

Thanks a lot to all the members of my PhD defense panel.

I gratefully acknowledge the financial support provided by China Scholarship Council for the whole study.

I finish all the thanks with my family where the most basic source of my life energy resides. Their support and love has been unconditional all these years.